12-2011

Radio Frequency Micro/Nano-Fluidic Devices for Microwave Dielectric Property Characterizations

Chunrong Song
Clemson University, chunrongs@yahoo.com

Recommended Citation

Song, Chunrong, "Radio Frequency Micro/Nano-Fluidic Devices for Microwave Dielectric Property Characterizations" (2011). *All Dissertations*. 836.
https://tigerprints.clemson.edu/all_dissertations/836

RADIO FREQUENCY MICRO/NANO-FLUIDIC DEVICES FOR MICROWAVE DIELECTRIC PROPERTY CHARACTERIZATIONS

A Dissertation
Presented to
the Graduate School of
Clemson University

In Partial Fulfillment
of the Requirements for the Degree
Doctor of Philosophy
Electrical Engineering

---

by
Chunrong Song
May 2011

Accepted by:
Dr. Pingshan Wang, Committee Chair
Dr. L. Wilson Pearson
Dr. Xiao-Bang Xu
Dr. Apparao M. Rao

ABSTRACT

In this dissertation, a number of different topics in microwave dielectric property measurements have been covered by a systematic approach to the goals of development of dielectric spectroscopy and study of its high electric field effects with integrated on-chip microwave microfluidic / nanofluidic devices.

A method of parasitic effects cancellation for dielectric property measurement is proposed, analyzed, and experimentally evaluated for microwave characterization of small devices and materials that yield low intensity signals. The method dramatically reduces parasitic effects to uncover the otherwise buried signals. A high-sensitive radio frequency (RF) device is then developed and fabricated to detect small dielectric property changes in microfluidic channel. Sensitivity improvement via on-chip transmission line loss compensation is then analyzed and experimentally demonstrated. Different samples are measured and high sensitivity is achieved compared to conventional transmission-line-based methods.

High DC electric field effects on dielectric properties of water are investigated with microwave microfluidic devices. Gold microstrip-line-based devices and highly-doped silicon microstrip-line-based devices are exploited. Initiation process of water breakdown in a small gap is discussed. Electrode surface roughness is examined and its effect on observed water breakdown is investigated. It is believed that electrode surface roughness is one of critical factors for the initiation process of water breakdown in small gap system. Finally, water dielectric property subjected to uniform DC electric field in 260 nm planar microfluidic channels is experimentally studied via silicon microstrip-line-based devices. When applied DC field is as high as up to ~ 1 MV/cm, the water is sustained and no breakdown is occurred. Strong water dielectric saturation effects are observed from measured water dielectric spectroscopy.

An on-chip, broadband microwave dielectric spectrometer with integrated transmission line and nanofluidic channels is designed, fabricated and characterized through microwave S-parameter measurements. Heavily-doped Si material is used to build the microstrip line to provide broadband characterization capability. 10 nm deep planar Si nanofluidic channels are fabricated through native oxide etch and wafer bonding process. It is the first effort to build the microstrip line with periodically loaded individual sub-10 nm nanofluidic channels to conduct the broadband high frequency characterization of materials within confined space. The functionality of the device is demonstrated by the measurement of DI water. It behaves well and has great potentials on the study of confinement effects of fluids and molecules. Further work includes development of parasitic signal de-embedding procedures for accurate measurements.

TABLE OF CONTENTS

Table of Contents (Continued)

Page

LIST OF TABLES

Table Page

LIST OF FIGURES

List of Figures (Continued)

List of Figures (Continued)

Figure Page

CHAPTER ONE

INTRODUCTION

A dielectric is an electrical insulator that may be polarized by an applied electric field. When a dielectric is placed in an electric field, electric charges do not flow through material, as in a conductor, but only slightly shift from their average equilibrium positions causing dielectric polarization. Because of dielectric polarization, positive charges are displaced toward the field and negative charges shift in opposite direction. This creates an internal electric field that partly compensates the external field inside the dielectric. If a dielectric is composed of weakly bonded molecules, those molecules not only become polarized, but also reorient so that their symmetry axis aligns to the field. Dielectric property of a material is represented by a complex quantity known as permittivity, which is usually normalized to permittivity of a vacuum and defined by equation $\varepsilon = \varepsilon^{'} - j\varepsilon^{''}$. Real part of the permittivity, $\varepsilon^{'}$, is a measure of energy stored and is called dielectric constant. Imaginary part of the permittivity, $\varepsilon^{''}$, is a measure of energy loss and called loss factor. The dielectric properties of a material are determined by its molecular structure. If the molecular structure changes, its dielectric property changes. Other properties, such as moisture content, biomass, bulk density, bacterial content, cancer detection, chemical reaction, structure, concentration and most other physical properties, can be correlated to dielectric properties. For example, amount of water in solid or liquid can be determined by measuring the permittivity of material in real time; cancer cell and healthy cell have different permittivity; mixtures with different concentrations have different permittivity, and so on. Because of these correlations, the measurement of permittivity has found applications in many fields, such as biology, medicine, food science, chemistry, drug discovery, agriculture, electrical/electronic devices, non-destructive testing, and so on.

The dielectric property, or permittivity, is one of the factors that determine how a material interacts with an applied electromagnetic field. Consider molecular structure of water as an example: it consists of two hydrogen atoms and one oxygen atom. Because of its bonding mechanism, hydrogen side of the molecule is more positive then oxygen side. Due to this unbalanced sharing of electrons by atoms of a molecule, a permanent dipole moment is caused. In an absence of an external electric field, these moments are oriented in a random order such that no net polarization is present. Under an external electric field, the dipoles rotate to align with the electric field causing orientation polarization to occur, therefore it causes the water have a particular permittivity. If the applied electric field is a changing field, there are a number of different mechanisms to illustrate how the dielectric property varies with the frequency of the applied electric field. Figure 1.1 shows a dielectric permittivity spectrum over a wide range of frequencies. Each dielectric mechanism effect has a characteristic relaxation frequency.

At low frequencies, the water molecules can follow the applied electric field, which gives maximum values of ε'. This polarization is a form of energy storage. Ionic current caused by positive and negative ions' movement in accordance to the electric field introduces losses into a system. When the frequency increases, the water molecules can no longer keep up the changing electric field. This results decrease of ε', consequently less energy storage and higher rotational losses. At these frequencies, the mass of the ions prevents them from responding the changing electric field. At even higher frequencies, the water molecules no longer respond to the electric field. The water molecules are stretched or even pulled apart. Therefore permittivity usually is measured at frequencies below 10^{11} Hz.

Dielectric spectroscopy which is also known as electrochemical impedance spectroscopy (EIS), measures the dielectric properties/permittivity of a medium as a function of frequency. It is based on the interaction of an external field with the electric dipole moment of the sample. Almost any physic-chemical system, such as electrochemical cells, mass-beam oscillators and even biological tissue, possesses energy storage and dissipation properties. Dielectric spectroscopy examines them. It has grown tremendously over past decade and is now being widely employed in a wide variety of scientific fields, such as biology, chemistry, nanofluidic electronics, health science and tribology.

Devices integrated with transmission lines can provide broadband microwave dielectric spectroscopy measurement for materials within microfluidic or nanofluidic channels. Compared with other experimental instruments, microwave dielectric spectroscopy is an ideal tool to study relaxation processes of materials. For example, the measurement method may be based on equivalent transmission line model as illustrated in Figure 1.2. As illustrated, C' and G' represent effects of the dielectric property of material under test (MUT), which is defined by equation $\varepsilon_x(\omega) = \varepsilon_x^{'} - j\varepsilon_x^{''}$. The obtained permittivity is related to MUT relaxation constant, τ. For instance, if Debye relaxation is assumed, the relationship becomes $\varepsilon_x(\omega) = \varepsilon_x^{'} - j\varepsilon_x^{''} = \varepsilon_\infty + \frac{\varepsilon_s - \varepsilon_\infty}{1 - j\omega\tau}$, where ε_s and ε_∞ refers to MUT permittivity at DC and infinite frequency, respectively. Therefore, broadband measurements utilizing the devices formed as described above are possible to define the relaxation time constant, τ. In addition, the MUT dielectric properties under different DC electric fields may be obtained by simultaneously applying different DC voltage across the transmission lines.

Compared to the devices with integrated microfluidic channels, the devices with integrated nanofluidic channels are more promising and attractive. They can be used to detect and analyze biological molecules, cells, their dynamic processes and surface interactions, such as protein and DNA folding-unfolding process analysis, cell detection and analysis, molecular structure analysis, bimolecular surface interaction analysis and molecular dynamics analysis in confined spaces. Examples of confined liquids include biological water between two membranes and liquid lubricants between two friction surfaces. Since both are only a few molecule thick, dielectric spectroscopy with nanofluidic channels enables the study of the dynamic interactions between surfaces and confined liquids.

Some materials, e.g., carbon nanotubes, zeolites and polymers such as poly vinyl methyl ether (PVME) and polyvinylpyrrolidone (PVP), naturally include nanochannels or a random network of nanopores. However, many limitations with utilizing nanochannels in these materials exists, such as their randomness, difficulty of controlling and modifying their pore surfaces uniformly and consistently, difficulty of studying effects of external electric fields, and occurrence of parasitic signals that obscure test readings.

Planar nanofluidic channels through nanofabrication processes are powerful tools for investigating materials under confinement, such as confined water, DNA and proteins. Its formation has easy control and it is readily integrated into the measurement devices. Various techniques developed from traditional semiconductor processing such as patterning, thin film deposition, wet/dry-etch of silicon and silicon dioxide thin films, and wafer bonding have produced nanochannels from ~20 nm to ~100 nm, mainly for nanofluidic research and bio-molecule separation and detection investigations. Although various methods for fabricating planar nanofluidic channels have been developed, room for improvement in the art exists. Unfortunately, producing nanofluidic channels having a height of about 1~10 nm remains very difficult. Channels having a height from about 1 nm to about 10 nm would be useful for many scientific and engineering investigations, including confinement effect research, biology studies and tribology studies. For example, measured dielectric properties of the confined water under DC electric field stresses have also not been reported to date. The ability to form nanofluidic channels of a smaller height could greatly improve functionality and performance of such devices.

In this dissertation, a number of different topics in radio frequency/microwave dielectric property measurements have been covered by a systematic approach to the goals of development of microwave dielectric spectroscopy and study of its high DC electric field effects with integrated on-chip microfluidic and nanofluidic devices. Below is an outline of different topics, each chapter covers a topic which includes several experimental approaches:

Chapter II presents a methodology development for parasitic effect cancellation/subtraction for radio frequency characterization of small devices or materials which yield low intensity signals. Two structure prototypes are exploited for different sample requirements: the structure with gaps which is needed to host Device Under Test (DUT); structure without gaps (with a through line) where it is no needs to host the DUT or Material Under Test (MUT).

Firstly, the proposed method is validated by the Advanced Design System (ADS) simulation and experiments, such as small capacitance measurements, transmission line dielectric permittivity measurements.

Secondly, a high-sensitive on-chip radio frequency (RF) sensor is developed and fabricated to detect small dielectric property changes in microfluidic channels. Sensitivity improvement via on-chip transmission line losses compensation is then analyzed and experimentally demonstrated. Different samples are measured and high sensitivity for small dielectric property changes is achieved compared to conventional transmission line based methods.

Chapter III presents a study of high DC electric field effects on microwave dielectric properties of water measured with radio frequency microfluidic devices.

Firstly, a radio frequency characterization method for on-chip liquid film dielectric property measurement is developed. Microstrip-line-based on-chip test devices are designed and fabricated to characterize the microwave dielectric properties of various on-chip liquid films. This on-chip microwave dielectric spectroscopy demonstrates a promising and inexpensive on-chip sensing mechanism for biomedical and chemical applications.

Secondly, water dielectric property subjected to uniform DC electric field in 300 nm planar microfluidic channels is experimentally studied. Test devices with gold (Au) microstrip line configurations are designed and fabricated through nanofabrication technology to investigate water dielectric saturation effects. Unfortunately, our results show that water breakdown occurs at ~ 100 kV/cm electric field under current system setup before any water dielectric saturation effects can be observed. Initiation process of water breakdown in a small gap is then discussed. Electrode surface roughness is examined and its effect on observed water breakdown is investigated. It is believed that electrode surface roughness is one of critical factors for the initiation process of water breakdown in small gap system.

Thirdly, water dielectric property subjected to uniform DC electric field in 260 nm planar microfluidic channels is experimentally studied. Test devices with highly-doped silicon (Si) microstrip line configurations are designed and fabricated through nanofabrication technology to investigate water dielectric saturation effects. When applied DC field is as high as up to ~ 1 MV/cm, the water is sustained and no breakdown is occurred. Strong water dielectric saturation effects are observed from measured water dielectric spectroscopy.

Chapter IV presents broadband microwave dielectric property characterizations with radio frequency/microwave nanofluidic devices.

An on-chip, broadband microwave dielectric spectrometer with integrated transmission line and nanofluidic channels is designed, fabricated and characterized through microwave S-parameter measurements. Heavily-doped Si material is used to build the microstrip line to provide broadband characterization capability. 10 nm deep planar Si nanofluidic channels are fabricated through native oxide etch and wafer bonding process. It is the first effort to build the microstrip line with periodically loaded individual sub-10 nm nanofluidic channels to conduct the broadband high frequency characterization of materials within confined space. The functionality of the device is demonstrated by the measurement of DI water. It behaves well and has great potentials on the study of confinement effects of fluids and molecules.

More detailed descriptions of each of the above-mentioned topics, such as previous work, device design and fabrication, experimental results, discussions and conclusions are contained in following chapters.

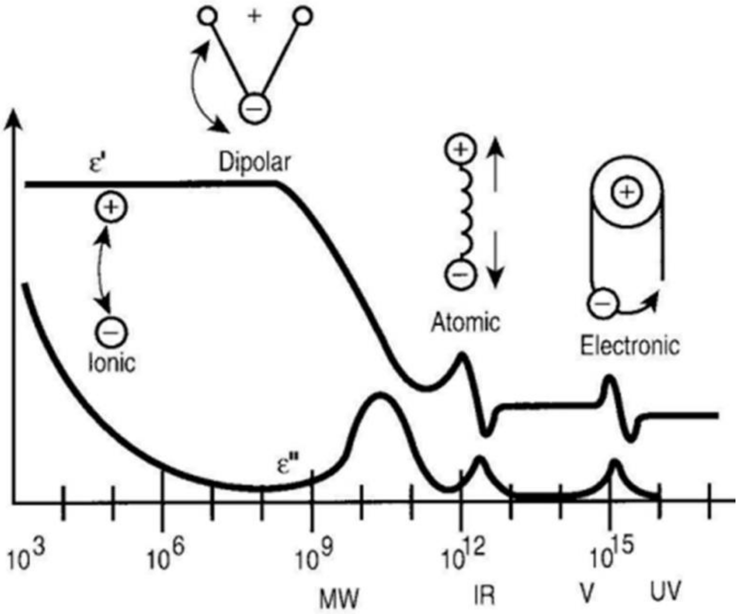

Figure 1.1: Dielectric permittivity spectrum over a wide range of frequencies [K. A. Mauritz, http://www.psrc.usm.edu/mauritz/dilect.html].

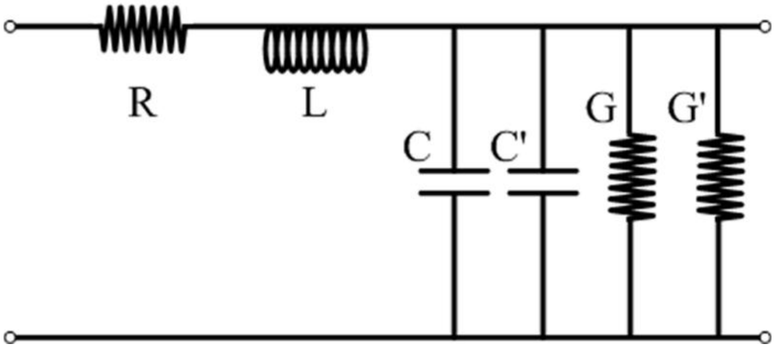

Figure 1.2: Equivalent high frequency transmission line model for broadband microwave dielectric spectroscopy measurement for materials within microfluidic or nanofluidic channels.

CHAPTER TWO

RADIO FREQUENCY MICROFLUIDIC DEVICES WITH PARASITIC EFFECT CANCELLATION FOR DETECTIONS OF SMALL DIELECTRIC PROPERTY CHANGES

2.1 Parasitic Effect Cancellation for Radio Frequency Characterizations of Small Devices

2.1.1 Introduction

Parasitic effects from measurement fixtures are difficult to handle in radio-frequency/microwave characterization of small devices. It is even more challenging when the expected signal level is low. Such devices include magnetroelectronic/spintronic devices and high-impedance devices, e.g., a metallic single-walled-carbon-nanotube (mSWNT), a SWNT transistor, a minimum-size deep-submicron metal-oxide-semiconductor (MOS) field-effect-transistor (FET), a sub-micron MOS FET that is operating in sub-threshold region, and a molecular device. The microwave characteristics of these devices are of great interest in their development and applications. Considering a metallic SWNT as an example; its high-frequency characteristics are important for fundamental physics studies [1] and for potential interconnect and sensor applications [2, 3]. However, its experimental characterization is very challenging because of very low signal levels due to its high impedance and overwhelming capacitive parasitic effects from measurement fixtures, shown in Figure 2.1. Uncertainties and errors in network analyzer characterization and device measurement make it difficult to interpret the obtained data when parasitic signals overwhelm the intended low intensity signals [4-6].

In this section, a new methodology has been developed for the characterization of small devices that uses microwave structures to significantly reduce parasitic effects of the test fixture with a focus on reducing the coupling gap capacitor effect. Both computer simulations and experimental measurements of small capacitance measurements are used for methodology evaluations.

2.1.2 Parasitic Effect Cancellation with Gaps

2.1.2.1 Design Methodology

Figure 2.2 shows a schematic of proposed microwave characterization structure for small devices with the parasitic effect cancellation. An incoming signal from port 1 is split evenly into two branches via a 3-dB power divider. The resistor of the power divider will absorb reflected signals from any structure discontinuities and provide isolation between the two branches. Signals transmitted across the gaps then propagate to the rat-race hybrid. Assume low-loss transmission lines with propagation constant $\gamma = \alpha + j\beta$, measured scattering parameter, S_{21}, is:

$$S_{21} = [\exp(-\alpha \sum_i l_i - j(\sum_i \beta l_i)) \cdot (S_{21(PowerDivider)}) \cdot (S_{21(Hybrid)})] \cdot (S_{21(DUT+C_p)} - \exp(-\alpha\lambda/2) \cdot S_{21(C_p)}), \qquad (2.1)$$

where $S_{21(DUT+Cp)}$ is the scattering parameter of the gap with a DUT, and $S_{21(Cp)}$ of the other gap without a DUT. The components in the bracket in (2.1) and C_p need to be determined by use of similar dummy structures.

2.1.2.2 Methodology Evaluation

2.1.2.2.1 Simulation Evaluation

Metallic single-walled nanotube (mSWNT) is used as an example to illustrate the proposed microwave characterization method, where the gap coupling capacitance dominates. High-frequency characteristics of mSWNT can be represented by a microwave transmission line model [7]. When the used mSWNT is a few μm long and the operating frequency is on the order of 10 GHz, a lumped RL model can be used to approximate the distributed transmission line CNT model, as is shown in Figure 2.1 (b).

From obtained scattering parameters, resistance R and inductance L of an mSWNT may be obtained through the following equations.

$$R = 2Z_0(1-|S'_{21}|)/|S'_{21}| \ (\Omega), \tag{2.2a}$$

$$L = \frac{(2Z_0 + R)\tan(-Angle(S'_{21})) - 4Z_0\omega RC_p}{\omega} \ (\mathrm{H}), \tag{2.2b}$$

where Z_0 is reference impedance, ω is signal angular frequency and $S'_{21} = S_{21(CNT+C_p)} - S_{21(C_p)}$ obtained from (2.1). The term *exp (-αλ/2)* in (2.1) has been omitted because of small α if low loss substrate is used.

Advance Design System (ADS) simulations are conducted for given values of R = 7 kΩ, L = 4 nH, C_p = 5 fF, which are reasonable estimations for the mSWNT and fixture gap coupling capacitance. Resistance and inductance are then calculated by the use of (2.2) and shown in Table 2.1. The corresponding results of conventional methods, which do not have parasitic effect cancellation capability, are also shown. Table 2.1 shows the dependence of R and L measurement accuracy on C_p measurement accuracy. C_p= 5 pF is the true value of the coupling capacitance of a gap with a width of 20 mil. It shows that the proposed method yields reasonable approximations of R and L, even when the knowledge of C_p is inaccurate. The conventional method yields accurate results when C_p is known accurately, but much larger errors otherwise. The accuracy of the proposed method is not ideal, but quite acceptable, considering the challenges of the targeted small device high-frequency characterization, e.g., no method has been found for L measurement of mSWNT yet.

2.1.2.2.2 Experiment Evaluation

In order to experimentally evaluate the proposed method for parasitic effects cancellation and small device measurement, small capacitors are used as DUTs. They are realized by changing the microstrip line gap widths, shown in Figure 2.3. If a small capacitance C is to be measured using the proposed method, then

$$C = \sqrt{\left|S_{21}^{'}\right|^2 / (1-|S_{21}^{'}|^2)} \,/\, (2Z_0\omega) \text{ (F).} \tag{2.3}$$

Three test structures are fabricated with their gap widths increased by 10 %, 30 %, and 50 %, compared to the original 50 Ω microstrip-line width (92 mil). The gap space was 20 mils. The structures consist of a conventional 3 dB Wilkinson power divider and a Rat-Race hybrid designed at 5 GHz. All ports are matched to 50 Ω. Roger RT/Duroid 5870 substrate with thickness $h = 31$ mils, $\varepsilon_r = 2.33$ and loss tangent = 0.001 is used.

Figure 2.4 (a) shows measured parasitic effect cancellation results. A ~23 dB reduction is obtained when compared with that of a single gap at 5 GHz. Figure 2.4 (b) shows measured capacitance results, which are close to anticipated data. Furthermore, measured capacitance ratios are approximate to the gap-width ratios as expected. These observations show validity of the proposed method.

2.1.3 Discussions and Conclusions

There are a few issues that determine the accuracy, sensitivity and applications of the proposed measurement method. The (electrical) symmetry of the proposed structures is a critical one. Any non-symmetric geometry between the upper branch and the lower branch will cause non-symmetric electrical behaviors, which will eventually appear at the port 2 in Figure 2.2. For instance, a non-symmetric 3-dB power division, non-symmetric transmission line widths (hence different attenuation constant, phase constant and gap capacitance) and non-symmetric hybrid will introduce a different signal at port 2. A non-symmetric substrate will further complicate the cancellation process. In addition, any non-symmetric fabrication scratches on the substrate surface would probably contribute to a less than ideal cancellation process.

When a gap is needed for connecting the DUT during the radio frequency characterization, the symmetry of the gap is more important. Fortunately, it is not too difficult to control gap symmetry to a level that satisfies a reasonable accuracy under current fabrication technology.

From the topology of the designed test structure, it is obvious that the main attenuation limitation comes from the $\lambda/2$ -length line (attenuation) difference of the hybrid ring. This attenuation difference dictates the substrates and structure design need to be properly chosen in order to improve sensitivity of the proposed method.

In conclusion, the proposed method cancels parasitic effects by use of passive microwave devices for microwave characterization of small devices that yield low intensity signals. Weak signals from small and high-impedance devices then emerge from the dramatically reduced background, particularly the otherwise overwhelming coupling capacitance effects. The data extraction procedure is straightforward and its accuracy depends on the symmetry and loss of the microwave structures. The design guidelines are straightforward. Both computer simulations and experimental measurements of small capacitance demonstrated the efficacy of the approach.

ACKNOWLEDGMENT

This work is partially supported by the US Army Research Office with Grant # 2005567.

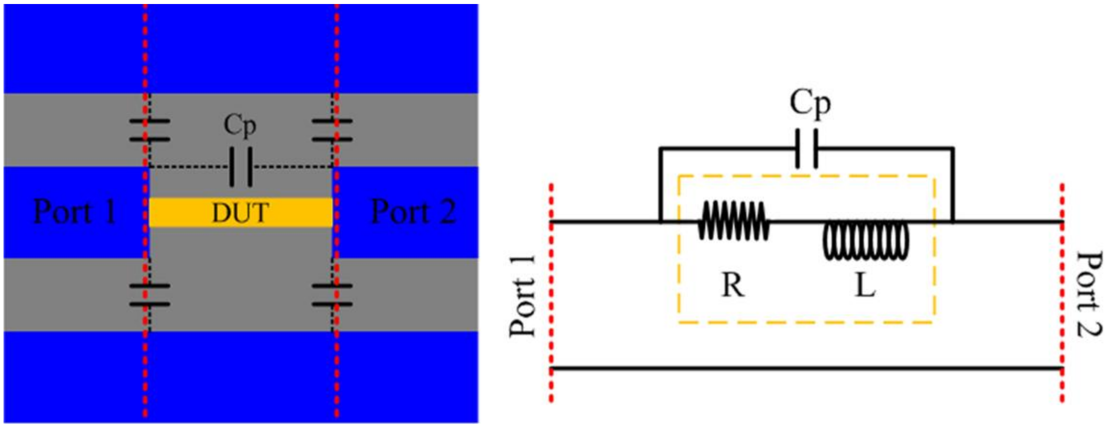

(a) (b)

Figure 2.1: (a) Top view of a high frequency measurement setup for a small device characterization. The (black) circuit components indicate the physical origins of the parasitic effects which are substrate dependent. A Device Under Test (DUT) is connected in between the two gaps. (b) A simplified equivalent circuit model of the measurement setup. Metallic SWNT is used as an example of DUT and its high frequency characteristics are represented by a microwave transmission line model shown in the (yellow) dashed-line rectangle. The gap capacitance C_p includes contributions from all relevant capacitive components shown in (a). Lossless substrates, such as fused silica, are assumed.

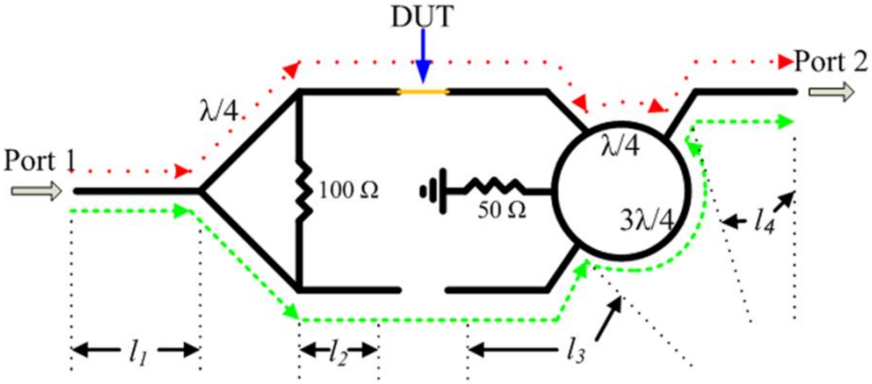

Figure 2.2: A schematic of the proposed microwave characterization structure. The (red and green) dashed lines indicate two main signal paths. Gaps are usually needed for microwave characterization of a device-under-test (DUT).

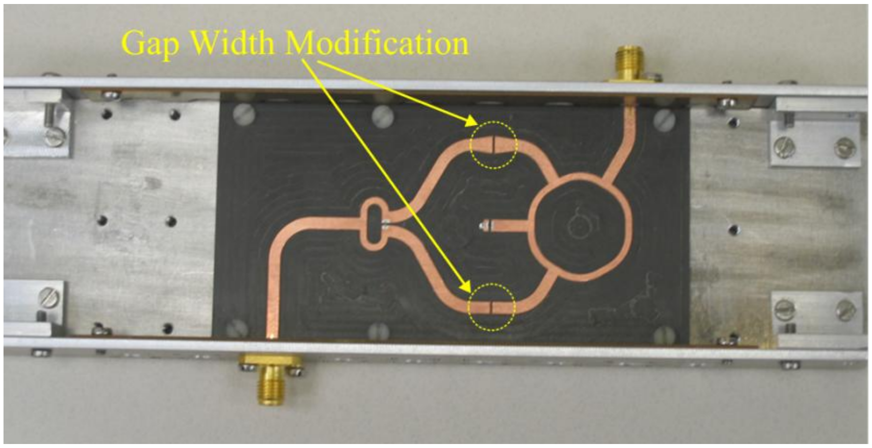

Figure 2.3: The photo of a structure with 50 % gap width increase in one signal path. Test structures have been fabricated with their gap widths increased by 10%, 30%, and 50%, respectively, compared to the original 50 Ω microstrip line width.

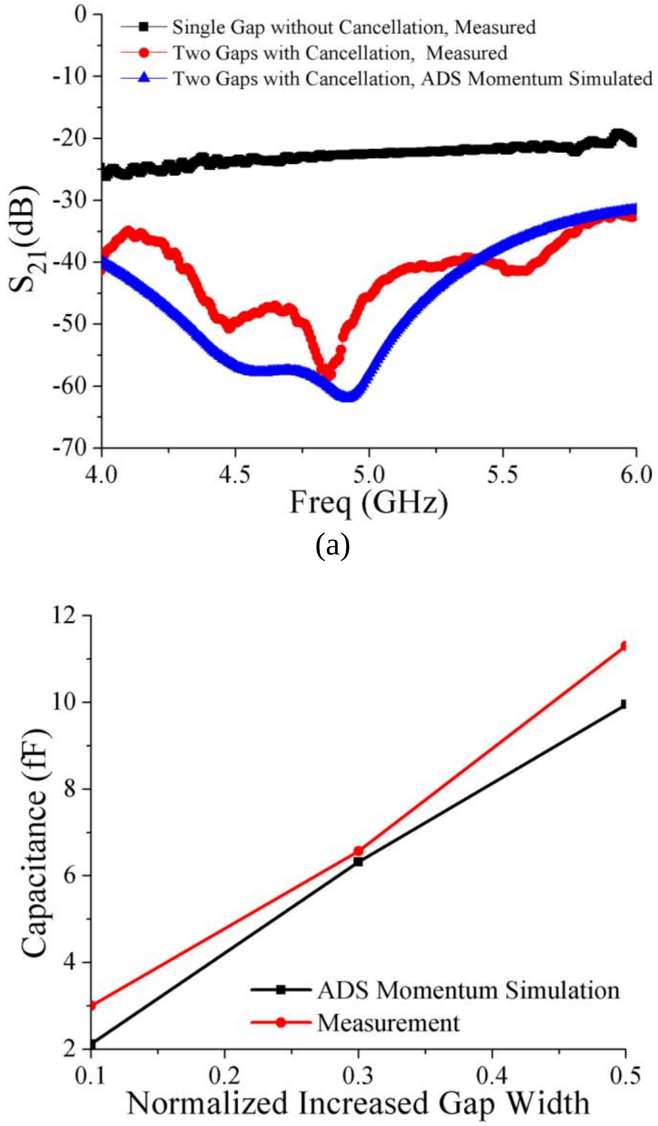

(a)

(b)

Figure 2.4: (a) Parasitic effect cancellation. Reflections cause additional resonance peaks that are not at ~ 5 GHz. (b) Capacitance values from measurement and ADS momentum simulation.

Table 2.1: Numerical evaluation of errors caused by inaccurate measured gap capacitance C_p (given data: R = 7 kΩ, L = 4 nH, C_p = 5 fF).

Cp *(fF)*	This Method				Conventional Method			
	R_cal *(kΩ)*	Error (%)	*L_cal* *(nH)*	Error (%)	*R_cal* *(kΩ)*	Error (%)	*L_cal* *(nH)*	Error (%)
1	7.14	2.04	11.3	182	4.77	-32	-	-
2	7.14	2.04	9.85	146	4.95	-29	-	-
3	7.14	2.04	8.42	110	5.27	-24	-	-
4	7.14	2.04	6.99	75	5.90	-16	-	-
5	7.14	2.04	5.56	39	7.15	2	4.23	5.7
6	7.14	2.04	4.13	3.3	11.0	57	107	2575
7	7.14	2.04	2.70	-32	-	-	-	-
8	7.14	2.04	1.28	-68	-	-	-	-

Notes: '-' indicates the calculated results are not meaningful.

2.2 Parasitic Effect Cancellation for Radio Frequency Dielectric Property Measurements

2.2.1 Introduction

Measuring complex dielectric property, or permittivity, is the foundation of a variety of microwave sensors, for which various high-frequency structures have been proposed and used [8-10]. The measurement is also an effective method for material characterization, biological specimen sensing, and signal transduction in current system miniaturization and integration efforts. Examples include characterization of low-k dielectric thin film for integrated circuit technologies [11] and the sensing of fluids [12-14] and biological specimens [15, 16] for lab-on-chip advancement [14, 17].

In these developments, planar transmission lines are usually the high frequency structure to use for the intended measurements. A few issues emerge therein: (i) parasitic effects, such as line loss, are not negligible; (ii) minute amount of specimens may only induce a small signal change; (iii) measurement uncertainties could be significant. The uncertainties are caused by network analyzer calibration process and probe tip contact repeatability [18, 19]. As a result, sensitivity and accuracy of the measurements are limited.

There have been many efforts and progress to improve measurement sensitivity and accuracy through different de-embedding and calibration procedures or simplified measurement procedures with new structures. In this section, we demonstrate that the method initially proposed in Section 2.1 which utilizes parasitic effect cancellation process can be further extended for sensitive and accurate dielectric property measurements.

2.2.2 Parasitic Effect Cancellation without Gaps

Figure 2.2 shows a schematic of proposed structure with parasitic effect cancellation for small device characterizations, where the gap is need to host the DUT and the gap coupling capacitance dominates. There are other application situations where no gap is needed to host the DUT or MUT while its expected signal level is relatively weak. Examples include characterizations of individual micro/nano magnetic structures or some bio/chem-related samples. The method proposed in Section 2.1 is still effective when gaps are directly connected. Therefore, it is anticipated that the method can be further extended for such applications.

Figure 2.5 shows a schematic of similar structure but with no gaps needed for sensitive and accurate dielectric property measurements. The design methodology is similar as we described in section 2.1.2.1. An incoming microwave signal from port 1 is split evenly via a 3-dB power divider into two branches. The resistor of the power divider will absorb reflected signals from any structure discontinuity and provide isolation between the two branches. Signals that are transmitted through the two branches will propagate to rat-race hybrid. The signal transmission coefficient from port 1 to port 2 can be expressed as

$$S_{21} = S_{21\_TOP} + S_{21\_BOT} = S_{21\_T} \times S_{21\_DUT} + S_{21\_BOT} = S_{21\_T} \times S_{21\_DUT} + S_{21\_B} \times S_{21\_REF}, \qquad (2.4)$$

where S_{21_TOP} and S_{21_BOT} are the signal transmission coefficients of the top and bottom paths, respectively. S_{21_DUT} and S_{21_T} are the signal transmission coefficients of section c_d (a DUT section) and the rest of top signal path components, respectively. S_{21_REF} and S_{21_B} are the signal transmission coefficients of section c'_d' (a reference section which is identical with section c_d except that it does not have DUT) and the rest of bottom signal path components, respectively. S_{21_T} and S_{21_BOT} can be determined with properly matched calibration structures that resemble the structure in Figure 2.5. The obtained S_{21_DUT} includes contributions from the material under test and the transmission line section that bears this material. The reference section is needed for some measurements, such as measuring a minute amount of bio-specimens in a buffer solution. S_{21_REF} of section c′_d′ can be represented by

$$S_{21\_REF} = \frac{2ZZ_0}{2ZZ_0\cosh(\gamma l) + (Z^2 + Z_0^2)sinh(\gamma l)}, \tag{2.5}$$

where Z_0 is system impedance, $Z = \sqrt{\frac{R + j\omega L}{G + j\omega C}}$, $\gamma = \sqrt{(R + j\omega L)(G + j\omega C)}$, and l is the line length. Parameters R, L, C, and G are the equivalent transmission line circuit parameters. Similar relationship applies to DUT, in which the addition of MUT would change C and G by an amount ΔC and ΔG. These changes correspond to the change of dielectric property due to MUT. Therefore, we have

$$S_{21\_DUT} = S_{21\_REF} + \frac{\partial S_{21\_DUT}}{\partial C}|_{REF} \times \Delta C + \frac{\partial S_{21\_DUT}}{\partial G}|_{REF} \times \Delta G = S_{21\_REF} + \Delta S_{21\_MUT}. \tag{2.6}$$

Assuming the same loss for the $\lambda/4$ and $3\lambda/4$ hybrid sections in Figure 2.5, (2.4) and (2.6) give

$$\Delta S_{21\_MUT} = \frac{S_{21}}{S_{21\_T}}, \tag{2.7}$$

at the desired frequency. Then ΔC and ΔG can be obtained, so are the small dielectric property changes.

Sensitivity improvement of the proposed approach is illustrated in Figure 2.6, which compares amplitude of S_{21} and $S_{21\_Compare}$ for different MUTs. S_{21} and $S_{21\_Compare}$ are the transmission coefficient of proposed sensing structure and a single transmission line sensing structure, respectively. Two reference materials for section c´_d´ are similar to that for thin film characterization in [11] and for fluids sensing in [12-14], respectively. Maximum $S_{21\_Compare}$ change is ~ 0.2 dB and 0.6 dB for the two cases. The proposed method, however, exhibits large S_{21} change even for a small dielectric property change, which indicates high measurement sensitivity. Change rate, determined by the change of S_{21} or $S_{21\_Compare}$ magnitude, versus the corresponding change of permittivity is shown in Figure 2.7. Sharp peaks around the reference permittivity indicate high sensitivity. It is also an indication that the proposed method is very sensitive for detecting small dielectric property changes.

The proposed method is experimentally evaluated with DUTs that are microstrip lines with different line width, shown in Figure 2.8. The structures are fabricated in Roger RT/Duroid 5870 substrate with thickness h = 31 mils, ε_r = 2.33 and loss tangent = 0.001.The reference section is a 50 Ohm microstrip line with the width of 92 mil and the length of 400 mil. Effective permittivity of the DUT section is changed due to line width change. From (2.4)-(2.7), characteristic impedance Z of the DUT is

$$Z = \frac{Z_0}{2}(a \pm \sqrt{a^2 - 4}), \tag{2.8}$$

where $a = \frac{2|\tan\alpha|}{\sqrt{(1+\tan^2\alpha)\cdot|S_{21\_DUT}|^2 - 1}}$, α is the phase of the S_{21_DUT}, Z_0 is reference impedance, normally 50 Ω.

Figure 2.9 and Table 2.2 show measured results, which agree with theoretical and simulation results reasonably well. The measured cancellation is better than 35 dB at ~6 GHz when the reference section and DUT section are identical. The cancellation is close to ADS momentum simulation results where the loss difference between the $\lambda/4$ and $3\lambda/4$ hybrid sections in Figure 2.5 is considered. If the loss difference is eliminated, simulation shows that better than 65 dB cancellation can be achieved.

2.2.3 Discussions and Conclusions

The proposed method exploits parasitic effect cancellation to dramatically reduce parasitic effects. The process can be understood as an interference approach that provides de-embedding operation. The effectiveness of the cancellation process depends on the symmetry of the structure, including loss difference of the hybrid line sections. Nevertheless, it is shown that the method is very sensitive to characterize small dielectric property changes even though no special considerations are implemented in our experimental demonstrations.

There are some issues that need to be addressed in future studies, such as bandwidth and miniaturization of the proposed structures. The proposed method works ideally at one frequency only. This bandwidth limitation mainly comes from the design of the rat-race hybrid, where a 180 °phase shift is needed for the two incoming common-mode signals to cancel each other. Thus broadband hybrid design needs to be exploited. Preliminary HFSS simulation results in Figure 2.10 show that a structure proposed in [20] can be explored for bandwidth expansion. It gives better than 40 dB cancellation over a broadband frequency range. Dimensions of the structures are mainly determined by the sizes of the power divider and the hybrid-ring. For GHz frequency or below, current structures may be too big to be integrated on-chip. As a result, miniaturization techniques, such as meander lines [21], need to be investigated as well. Some current efforts, such as dramatic size reduction on the hybrid and power divider can be exploited.

In conclusion, an approach of parasitic effect cancellation for dielectric property measurement is proposed, analyzed, and experimentally evaluated. As a result, weak signals from dielectric material permittivity changes emerge from the dramatically reduced background. This approach is a further extension of the method proposed in Section 2.1, and it is suitable for the applications where no gap is needed to host the DUTs or MUTs while expected signal level is relatively week. Sensitivity is greatly improved for dielectric property measurements. Experimental results agree well with theoretical and simulation results.

ACKNOWLEDGMENT

We would like to acknowledge the financial support from NSF, grant # ECCS-0622082.

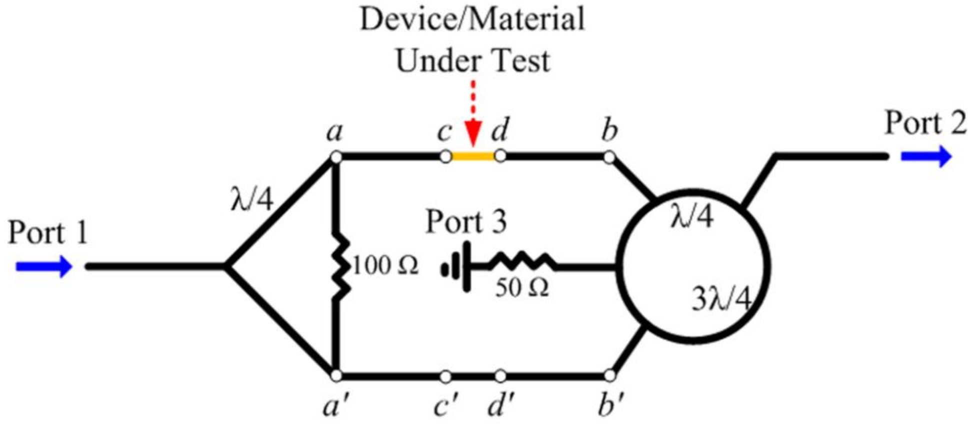

Figure 2.5: A schematic of proposed microwave characterization structure with no gap needed to host DUTs or MUTs.

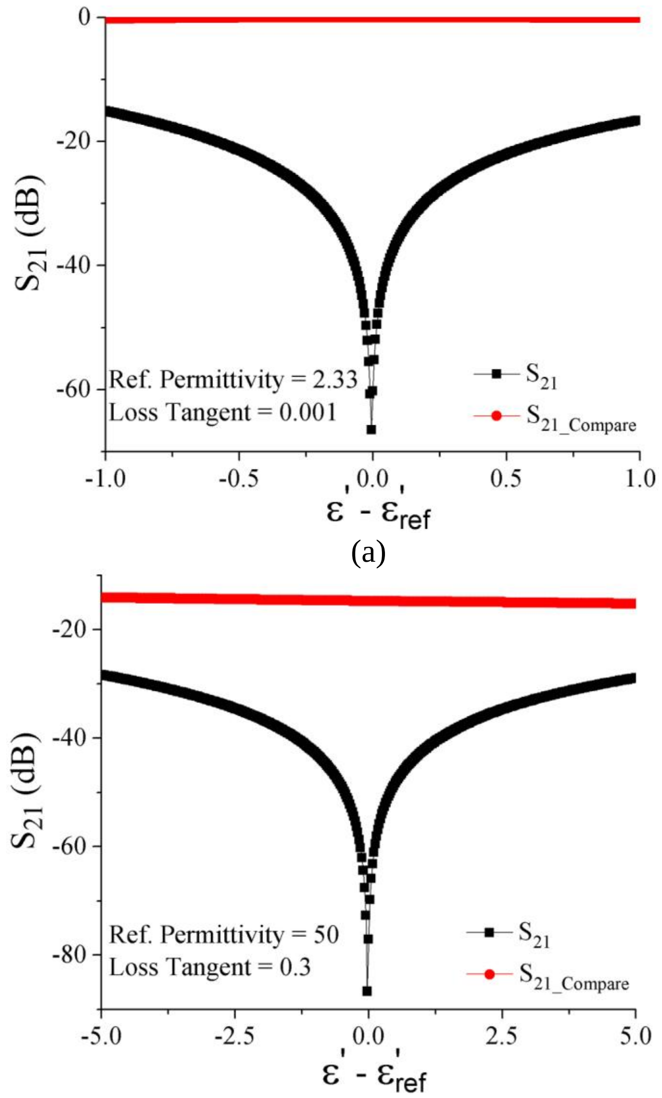

(a)

(b)

Figure 2.6: The scattering parameters S_{21} (black line) and $S_{21\_Compare}$ (red line). Two different materials are assumed as references as shown in (a) and (b). The substrate material for the rest of the structure in Figure 2.5 has permittivity 2.33 with loss tangent 0.001. The structure is designed for 6 GHz operation.

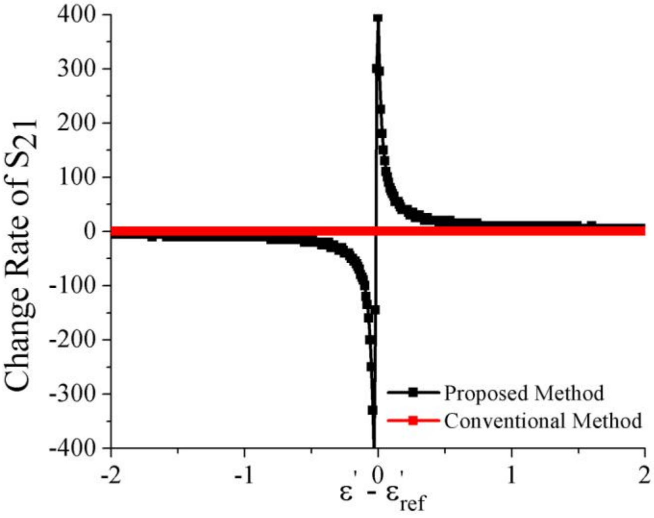

Figure 2.7: Change rate of S_{21} defined as ΔS_{21}(dB) / $\Delta\varepsilon$.

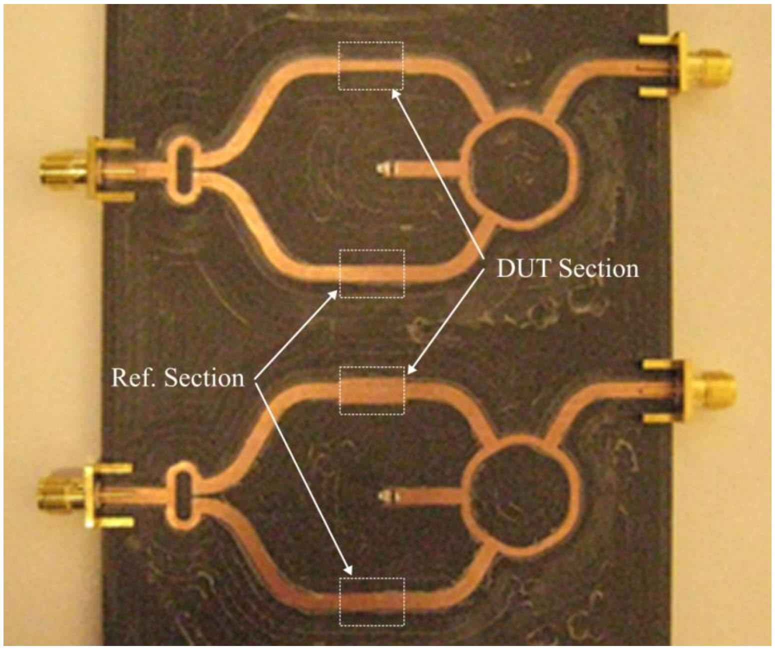

Figure 2.8: A photo of some test structures. Line widths of these two DUTs are 60 mil and 150 mil, respectively.

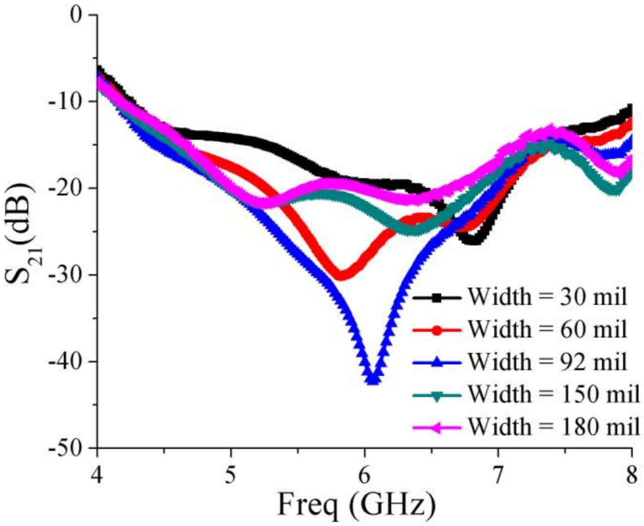

Figure 2.9: Measured S_{21}. Transmission lines with different line widths are the DUTs in the top path.

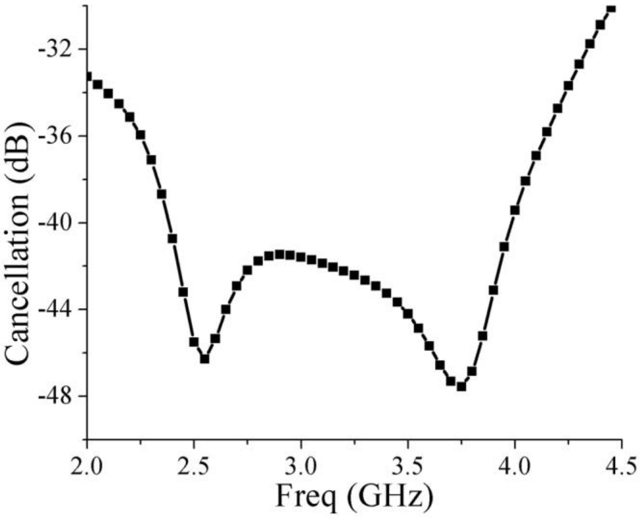

Figure 2.10: HFSS simulation for broadband cancellation design.

Table 2.2: Measurement results for transmission line with different line width

DUT Line Width (mil)	**Z_0 (Ω)**			**ε_{eff}**		**Line Width (mil)**
	Theoretical	**ADS Simulation**	**Measurement**	**Theoretical**	**Measurement**	**Measurement**
30	94.1	97.3	94.4	1.847	1.835	30.0
60	65.8	67.7	63.1	1.913	2.081	63.9
92	50.3	53.0	49.7	1.961	2.009	92.9
150	35.5	36.6	36.3	2.021	1.939	145.2
180	30.9	32.0	30.0	2.045	2.175	179.7

Note: Theoretical Z_0 and ε_{eff} are calculated according to [D.M. Pozar, "Microwave engineering", third edition, Wiley, 2005]; the choice of the different line width is limited by the fabrication precision available.

2.3 Radio Frequency Devices for Measurements of Small Dielectric Property Changes in Microfluidic Channels

2.3.1 Introduction

Measuring dielectric property changes has been developed and used as an effective approach to investigate biological matter and processes, such as protein thermal unfolding and refolding [22], lipid bilayer membranes [23], large aqueous-based molecules [24], and cells [25]. It has also been developed for bioanalysis [16, 24, 26]. Sensors that are based on measuring dielectric property changes, such as surface moisture sensors [27, 28], have been demonstrated as well. In comparison with other approaches, measuring dielectric properties and their changes (i.e., dielectric spectroscopy) electronically has several advantages. It provides a relatively simple electronic way to gain information about the subject without the need for labeling, chemical modification or physical intrusion. In addition, electronic methods are compatible with other sensor techniques and hold the potential for parallelization and integration.

Transmission lines and antennas are two main high-frequency structures developed and used for dielectric property measurements. A slot antenna/cuvette assembly had a sensitivity that is ~30 times higher than that of fluorescence spectroscopy, which is the most sensitive method popular for protein thermodynamics characterization [22]. Resonant frequency shift was used in Ref. [22] as an indicator of dielectric property changes. For planar transmission line structures, which can be readily integrated for lab-on-chip applications, elastomer polydimethylsiloxane (PDMS) microfluidic channels are usually developed since most bio-specimens and bio-processes naturally exist and occur in an aqueous environment. Some recent efforts are coplanar waveguide (CPW) transmission lines for sub-microliter fluid sample measurement [29], dielectric heating effect investigations [30], single cells studies [31], and on-chip CPW for biological cell characterization and analysis [32]. However, the sensitivity of these transmission line based approaches is relatively limited due to background signals that come from the lines [26]. These background signals are usually strong, yet necessary for sample probing and signal transduction. In this section, we demonstrate an on-chip RF device that uses interference with planar transmission lines to improve dielectric property measurement sensitivity. The method was initially proposed and briefly discussed in Ref. [33].

2.3.2 Design Methodology and Device Fabrication

Figure 2.11 is a schematic of the proposed high sensitivity RF device. An incoming signal from port 1 is split evenly into two branches via a 3-dB Wilkinson power divider. 100 Ω resistor of the Wilkinson power divider will absorb reflected signals from any structure discontinuities and provide isolation between the two branches. Signals transmit across the Material Under Test (MUT) channel and reference material (REF) channel, and then propagate to the 180 ° rat-race hybrid and arrive at port 2. Port 3 is terminated by a 50 Ω resistor. Assume low-loss transmission lines with propagation constant $\gamma = \alpha + j\beta$, the measured scattering parameter, S_{21}, at deign frequency is

$$S_{21} = [\exp(-\alpha \sum_i l_i - j(\sum_i \beta l_i)) \cdot S_{21(PowerDivider)} \cdot S_{21(Hybrid)}] \cdot (S_{21(MUT)} - \exp(-\alpha\lambda/2) \cdot S_{21(REF)}). \tag{2.9}$$

where $S_{21(MUT)}$ is the scattering parameter of the transmission line section on which MUT PDMS channel is attached; $S_{21(REF)}$ is for the transmission line section on which REF PDMS channel is attached.

When loss difference (exp($-\alpha\lambda/2$)) between λ/4 section and 3λ/4 section of ring hybrid is small, two signals coming from the top path and the bottom path will cancel each other provided that $S_{21(MUT)} = S_{21(REF)}$, i.e. the two PDMS channels are filled with the same materials. Then $S_{21} = 0$. If $S_{21(MUT)} \neq S_{21(REF)}$, their difference will appear at port 2, then $S_{21} \neq 0$. As a result, background signals are canceled and small differences between the MUT and REF materials are detected.

Fabricated RF device is shown in Figure 2.12 with PDMS microfluidic channels attached. Designed operating frequency is 6 GHz. A 4" 500 μm thick Corning Pyrex 7740 wafer is used as substrate. Its dielectric constant is 4.6 with a loss tangent of 0.004 @20 ℃ and 1 MHz, respectively. Due to design and process convenience, microstrip lines, instead of more sensitive CPW, are designed and fabricated for the device. Standard photolithography procedures and lift-off process are used for pattern transfer and device fabrication. The microstrip lines are formed with chromium(20 nm)/aluminum (2000 nm)/gold (80 nm) metal stack. Thin film chip resistors are attached to the device. Finally, SYLGARD 184 silicone elastomer kit is used to fabricate the PDMS microfluidic channels. Microfluidic channel mold is fabricated by use of 4" Si wafer through the standard photolithography and Deep Reactive-Ion Eching (DRIE) Si etch (Bosch process). Final dimension of microfluidic channel is 8 mm long, 10 mm wide and 350 μm high. Two holes are punched as sample inlet and outlet. In order to stick the

PDMS channel to the device which is fabricated on Pyrex glass substrate, both surfaces are treated with oxygen plasma to create reactive groups for strong bonding. The PDMS microfluidic channels are manually aligned to the device under microscope. Peek Tubing are then inserted into inlet and outlet and glued by the UV curable epoxy for sample solution injection.

2.3.3 Discussions and Conclusions

An HP8510C vector network analyzer and a Cascade probe station with ground-signal-ground (GSG) probes are used to measure scattering parameters. A full two-port calibration procedure is conducted before measurements. Two sets of primary alcohol-water mixtures are prepared with different concentrations in terms of molar fractions. The REF PDMS channel residing in the bottom path is filling with reference solution, deionized water in this case; the MUT PDMS channel residing in the top channel is filled with different sample solutions. Transmission scattering parameters S_{21} were measured for these samples.

The S-parameter S_{21} measurement results are shown in Figure 2.13. Good background cancellation performance, ~56 dB, is observed when the MUT and REF PDMS channels were filled with deionized water (namely x_m or $x_e = 0.00$). The frequency, where the S_{21} has minimum value, is defined as f_m. It shifted by 7.5 MHz from the design frequency (6 GHz) due to design and fabrication variations and the attachment of the PDMS channels. Dielectric property changes in MUT cause the f_m frequency shift and signal level change at the design frequency. Both can be used as sensing indicators of dielectric property changes as have been in Ref. [22] and Ref. [16]. The change of S_{21}

(dB) is defined as $S_{21\_Mixture}$ (dB) – S_{21_Water} (dB), where $S_{21\_Mixture}$ and S_{21_Water} are the S_{21} responses when the MUT is alcohol-water mixture and deionized water, respectively. Figure 2.14 (a) shows the change of S_{21} measured at operating frequency, 6 GHz, by use of our RF device and the comparison single microstrip line device, both are shown in Figure 2.12. Identical alcohol-water mixtures are measured by use of both devices. It is clear that our RF device is much more sensitive than the comparison line. Figure 2.14 (b) shows the variation of frequency f_m with approximate dielectric constant ε' for alcohol-water mixtures with different molar fractions. The dielectric constant values obtained in Ref. [34] are used. It shows that the proposed RF device is two times more sensitive than the set up in Ref. [22].

A few factors affect the sensitivity of the proposed RF device. Symmetry of the device is the most important one since it determines the level of cancellation. The loss difference between the $\lambda/4$ and $3\lambda/4$ sections is a main reason for device asymmetry that leaves residual background signals. Fortunately, this problem can be solved by adjusting the metal film thickness of the two sections. This sensitivity improvement technique will be analyzed and demonstrated in details in the next section. For the device in Figure 2.12, the two PDMS channels are another possible major source of asymmetries since the channels are manually aligned to the RF device under microscope. The asymmetry probably explains the deep peak in Figure 2.13 (a) and (b). A second factor is the length of the PDMS channel if we define sensitivity as the minimum detectable concentration level of the mixture. Therefore, there is a tradeoff between the volume of MUT and the device sensitivity. A third factor is the type of transmission lines that are used and the way they are used. The RF device in Figure 2.12 uses the top space of microstrip lines for MUTs. This kind of arrangement is least sensitive to dielectric property changes since the RF field of microstrip line is mainly concentrated between the signal lines and the ground. Nevertheless, the proposed RF device demonstrates great sensitivity improvement. Further sensitivity improvement is expected if MUT is placed between the signal line and the ground of the microstrip lines, such as the capacitor sensor [35], or if CPW is used.

In conclusion, we have demonstrated a sensitive on-chip RF device to detect small dielectric property changes in microfluidic channel. The device consists of an on-chip Wilkinson power divider and a rat-race hybrid which are built with planar microstrip lines and thin film chip resistors. Interference is used to cancel parasitic background signals. As a result, measurement sensitivity is improved by more than 20 dB compared with conventional transmission lines. Compared with an ultra-sensitive slot antenna/cuvette assembly [22], the proposed RF device is two times more sensitive.

ACKNOWLEDGMENT

Part of the device fabrication is conducted at the Cornell NanoScale Science & Technology Facility (CNF), Cornell University. The work is supported by NSF #ECCS-0703042. We also would like to thank Dr. Xiangchun Xuan for PDMS microfluidic channel fabrication.

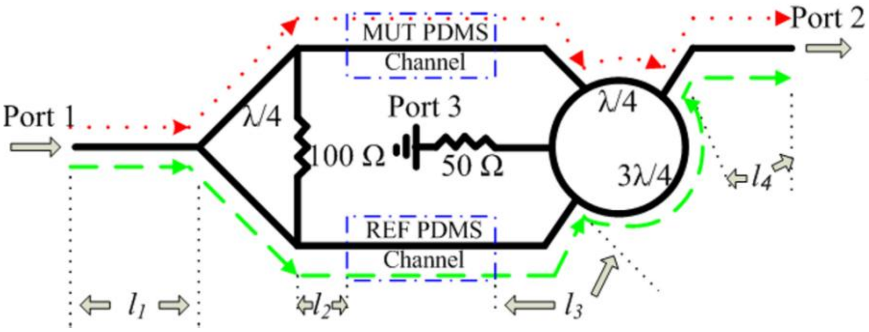

Figure 2.11: Schematic of the proposed high sensitivity RF sensing device. Dotted and dashed lines indicate two main signal paths. Dashed boxes indicate attached PDMS microfluidic channels for Material Under Test (MUT) and Reference Material (REF).

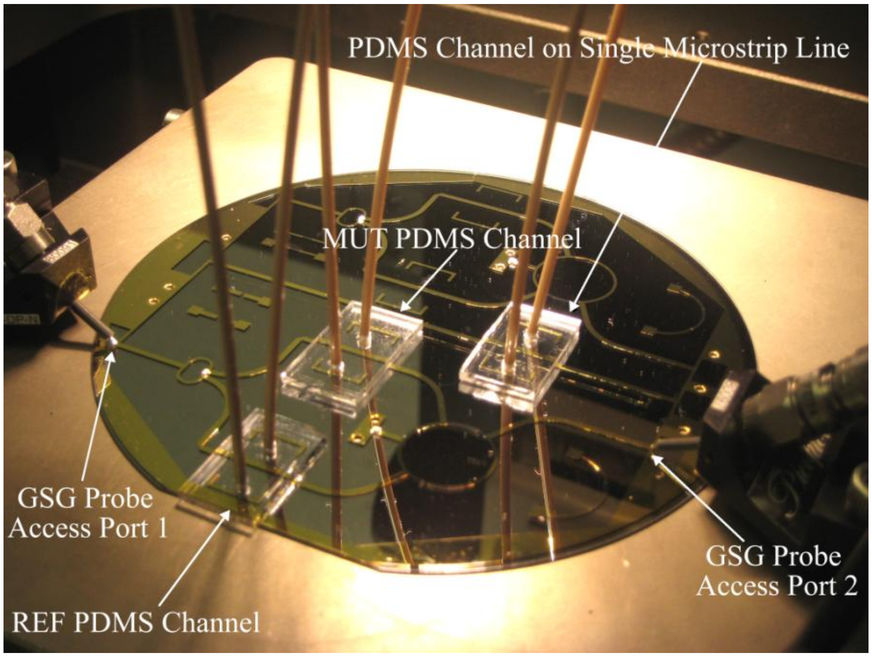

Figure 2.12: Fabricated RF device with PDMS microfluidic channels attached. A single microstrip line is also fabricated on the same wafer for the purpose of comparing background noise levels and measurement sensitivities.

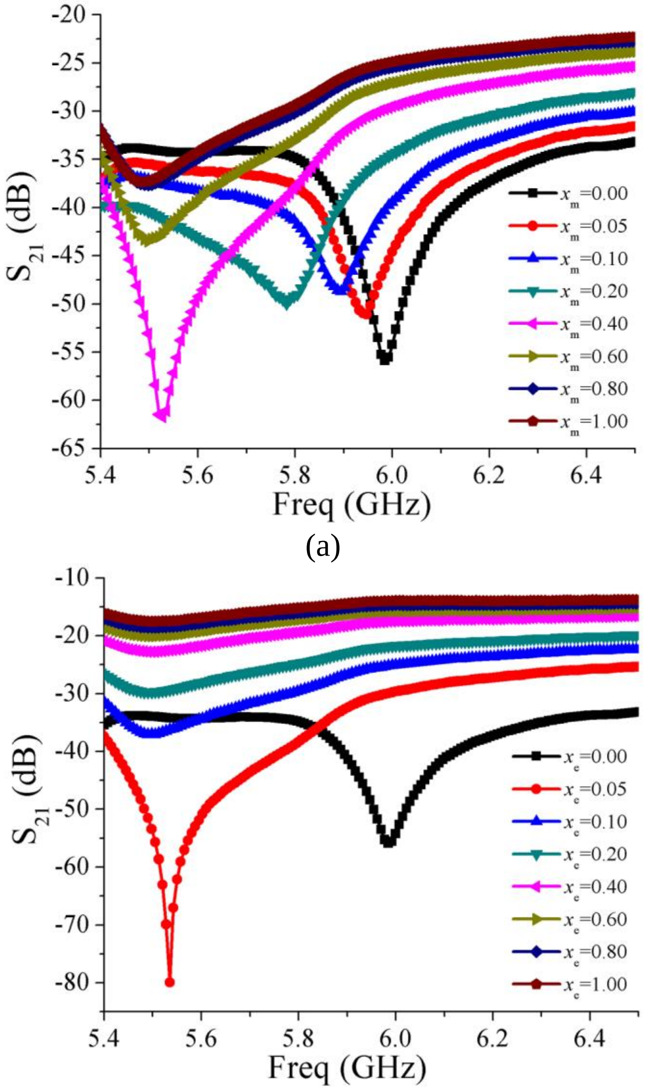

(a)

(b)

Figure 2.13: Measured S_{21} for (a) methanol-water mixtures, and (b) ethanol-water mixtures with different molar fractions, x_m and x_e, respectively.

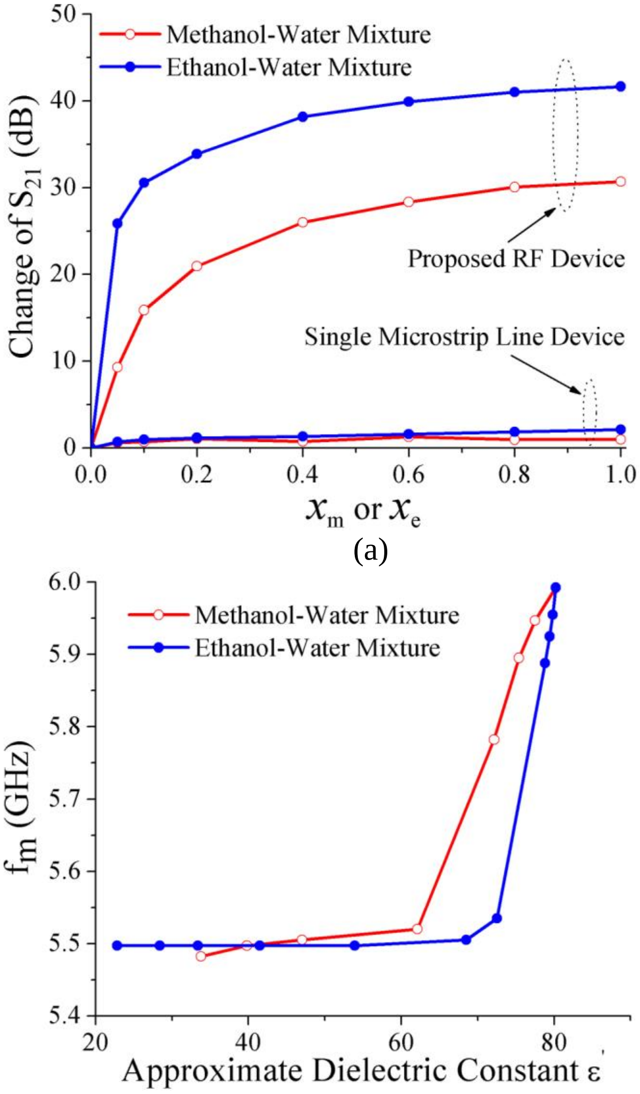

(a)

(b)

Figure 2.14: (a) Changes of transmission scattering parameter S_{21}, measured at 6 GHz, for the methanol-water mixtures and ethanol-water mixtures with different molar fractions by use of the proposed RF device and a comparison single microstrip line device as shown in Figure 2.12. (b) Variation of frequency f_m with approximate dielectric constant ε′ of methanol- and ethanol-water mixtures.

2.4 Sensitivity Improvement of Radio Frequency Devices through On-Chip Transmission Line Losses Compensation

2.4.1 Introduction

Measuring dielectric property change with microwave devices is of great interest in the development of sensors for bio-analysis [16, 22, 24, 36], biomaterial probing [23-25] and consumer product applications [28, 37] since it provides a relatively simple electronic way to gain information about subject under investigation without need for labeling, chemical modification or physical intrusion. Additionally, electronic methods are compatible with other sensor techniques and hold potentials for parallelization and integration.

Microwave sensor sensitivities, defined as the minimum amount of material property change ($\delta\varepsilon$) or the minimum amount of materials (δv) that can be detected, are key to their applications. There have been various efforts to improve them. For δv improvement, microfabrication and nanofabrication techniques are often used to integrate microfluidic and nanofluidic channels with on-chip microwave devices in the context of lab-on-chip development. Some recent examples include coplanar waveguide transmission lines (CPW) for sub-microliter fluid sample measurement in [29], a time-domain coplanar probe capable of 10 microliter water detection in [36], dielectric heating effect investigations in [30], single cells studies in [38], and on-chip CPW for biological cell characterization and analysis in [32]. Planar transmission lines are usually used in these integration efforts due to fabrication convenience. For $\delta\varepsilon$ improvement, a recent effort used a slot antenna/cuvette assembly [22] to demonstrate a sensitivity that is 30 times higher than that of fluorescence spectroscopy, which is the most sensitive conventional method for protein thermodynamics characterization. Resonant frequency shift was used in [22] as an indicator of dielectric property change.

In a recent letter [39], we demonstrated an integrated microwave sensor that is 2 times more sensitive than that reported in [22]. Volumes of the integrated microfluidic channels are 28 microliter. The device uses on-chip interference to cancel parasitic signals, therefore, to boost sensor sensitivity. In this section, we demonstrate that the cancellation level can be further boosted by compensating the line loss through adjusting thickness of λ/4 section of rat-race hybrid ring. Corresponding sensor fabrication process is described. We also analyze further possible sensitivity improvement by use of different transmission lines configurations that have stronger couplings.

2.4.2 Loss Compensation and Device Fabrication

Figure 2.15 shows a schematic of the high sensitivity microwave sensing structure as we described in previous sections.

As was mentioned in [39], the loss difference between the λ/4 section and 3λ/4 section of the hybrid ring is one of the main factors that affect the parasitic signal cancellation performance. Minimizing the loss difference is a key to improve the device sensitivity. Measured transmission scattering parameter S_{21} is

$$S_{21} = [\exp(-(\alpha + j\beta)\cdot\sum_i l_i)\cdot S_{21((PowerDivider)}\cdot S_{21(Hybrid)}]\cdot[\exp(-(\alpha_1 + j\beta_1)\cdot\frac{\lambda}{4})\cdot S_{21(MUT)} + \exp(-(\alpha_2 + j\beta_1)\cdot\frac{3\lambda}{4})\cdot S_{21(REF)}]. \tag{2.10}$$

where $S_{21(MUT)}$ is scattering parameter of transmission line section on which MUT PDMS channel is attached; $S_{21(REF)}$ is for transmission line section on which REF PDMS channel is attached; $\gamma = \alpha + j\beta$ is propagation constant for transmission line section l_1, l_2, l_3 and l_4; $\alpha_1 = \alpha_{c1} + \alpha_{d1}$ and $\alpha_2 = \alpha_{c2} + \alpha_{d2}$ are attenuation constants of the $\lambda/4$ section and $3\lambda/4$ section of hybrid ring transmission line, respectively, subscripts c and d indicate the attenuation due to conductor loss and dielectric loss, respectively; β_1 is phase constant of hybrid ring transmission line.

Consider TEM and quasi-TEM mode operation of the transmission lines, the attenuation due to dielectric loss is [40]

$$\alpha_d = \frac{\varpi\sqrt{\mu_0\varepsilon_0}\,\varepsilon_r(\varepsilon_{eff}-1)\tan\delta}{2\sqrt{\varepsilon_{eff}}(\varepsilon_r-1)} \text{ Np/m}, \tag{2.11}$$

where ε_r and $\tan\delta$ are dielectric constant and loss tangent of substrate, respectively, ε_{eff} is effective dielectric constant and ω is angular frequency. The attenuation due to conductor loss is

$$\alpha_c = \frac{R_s}{Z_0 W} \text{ Np/m}, \tag{2.12}$$

where R_s is surface resistivity of conductor, Z_0 and W are transmission line characteristic impedance and width, respectively.

Surface resistivity R_s is related to conductor thickness t and conductivity σ as follows:

$$R_s = \begin{cases} \dfrac{1}{\sigma t}, & \text{if } t \le \delta_s \\ \dfrac{1}{\sigma \delta_s}, & \text{if } t > \delta_s \end{cases} \tag{2.13}$$

where conductor skin depth $\delta_s = \sqrt{\dfrac{2}{\varpi \mu_0 \sigma}}$.

For a given substrate and transmission line width, (2.11) indicates $\alpha_{d1} = \alpha_{d2} = \alpha_d$, (2.12) and (2.13) indicate $\alpha_c \propto \frac{1}{t}$. This relationship implies that the α_c can be adjusted by tuning the conductor thickness. As a result, the loss difference (δL) can be represented by

$$\delta L = \alpha_1 \cdot (\frac{\lambda}{4}) - \alpha_2 \cdot (\frac{3\lambda}{4}) = (\alpha_{c1} + \alpha_{d1}) \cdot (\frac{\lambda}{4}) - (\alpha_{c2} + \alpha_{d2}) \cdot (\frac{3\lambda}{4}) \overset{\alpha_{d1}=\alpha_{d2}=\alpha_d}{=} (\alpha_{c1} - 3\alpha_{c2}) \cdot \frac{\lambda}{4} - \alpha_d \cdot \frac{\lambda}{2} \text{ Np.} \tag{2.14}$$

An optimum cancellation occurs at

$$\delta L = (\alpha_{c1} - 3\alpha_{c2}) \cdot \frac{\lambda}{4} - \alpha_d \frac{\lambda}{2} = 0 \tag{2.15}$$

Thus, we have

$$\alpha_{c1} - 3\alpha_{c2} = 2\alpha_d \tag{2.16}$$

Assume the conductor thicknesses of the λ/4 section and 3λ/4 section are t_1 and t_2, respectively. Together with (2.12), (2.13) and (2.16), the relationship between t_1 and t_2 for optimum loss cancellation is:

$$t_1 = \frac{1}{\frac{3}{t} + 2 Z_0 W \sigma \alpha_d}, \tag{2.17}$$

where $t = \begin{cases} t_2 & \text{if } t_2 \le \delta_s \\ \delta_s & \text{if } t_2 > \delta_s \end{cases}$

For low loss substrate, (2.17) shows that t_1 should be close to one-third of t_2 or δ_s, depending on the relative value of thickness t_2 and δ_s.

Under optimum cancellation condition, (2.10) is simplified to the following:

$$S_{21} = (-j) \cdot \exp(-(\alpha + j\beta) \cdot \sum_i l_i) \cdot S_{21(PowerDivider)} \cdot S_{21(Hybrid)} \cdot A \cdot (S_{21(MUT)} - S_{21(REF)}) \qquad (2.18)$$

where constant $A = \exp(-\alpha_1 \cdot \frac{\lambda}{4}) = \exp(-\alpha_2 \cdot \frac{3\lambda}{4})$.

Above analysis shows that tuning metal thickness of the λ/4 section and 3λ/4 section of the hybrid ring is a practical and easy method to minimize the conductor loss difference.

Devices with different λ/4 section thickness are fabricated to demonstrate the loss compensation effects. Fabrication of the 6 GHz microwave devices starts with a 4" Corning Pyrex 7740 wafer of thickness 500 µm. Its dielectric constant is 4.6 with a loss tangent of 0.004 @20 ℃ and 1 MHz. Microstrip lines are used as transmission lines for fabrication convenience. A two-mask process is used. The λ/4 section of the hybrid ring is first fabricated through lift-off process. It is a stack of Cr/Al/Au thin film with different metal thickness t_1, listed in Table 2.3. 20 nm Cr layer is used for adhesion purpose. 80 nm Au layer is for oxidization prevention, good probing contact, and good bio-compatibility considerations. Some 1 mm diameter holes are drilled mechanically. They provide electrical connection between 50 Ω termination resistor and the ground while a stack of Cr (20 nm) / Al (2000 nm) / Au (80 nm) metal thin film is deposited as ground plate on the backside of the wafer. Next, similar lift-off process is used to deposit a metal stack of Cr (20 nm) / Al (2000 nm) / Au (80 nm) for the rest structures of the device. 50 Ω and 100 Ω thin film chip resistors shown in Figure 2.15 are then attached to the devices. Figure 2.16 (a) shows a photo of fabricated microwave device before attachment of PDMS channels. Figure 2.16 (b) shows a zoom-in microscope image of thickness-tuned λ/4 section of the hybrid ring. Finally, tubes and PDMS microfluidic channels with 8 mm length, 10 mm width and 350 μm height are attached to the devices as described in Section 2.3.

2.4.3 Measurement Results

2.4.3.1 Loss Compensation

An HP8510C vector network analyzer is used to measure scattering parameters. A full two-port Short-Open-Load-Thru (SOLT) calibration procedure is conducted before measurements.

Figure 2.17 (a) shows the measured results for the devices with λ/4 section thickness listed in Table 2.3. Corresponding Advance Design System (ADS) simulation results are shown in Figure 2.17 (b). Frequency at which S_{21} has a minimum value is defined as f_m. Slight f_m frequency shift is observed for different metal thickness since different attenuation factors affect f_m, as implied by (2.10). Without any thickness tuning (i.e., metal thickness of λ/4 section t_1 = 2100 nm), the loss of the λ/4 section is less than the loss of the 3λ/4 section, and S_{21} at f_m is around 40 dB. The cancellation is improved while decreasing t_1. The best cancellation is achieved when t_1 is 500 nm, which is ~1/3 of the skin depth of the 3λ/4 section. The 500 nm is also very close to the theoretical predication obtained from (2.17). Continuing decreasing t_1, the loss of the λ/4 section is larger than the loss of the 3λ/4 section, thus the performance is deteriorated. When the metal thickness is very thin, e.g., t_1 = 200 nm, the cancellation performance is even worse than the one without any thickness adjustment (t_1 = 2100 nm). Some small peaks in the measurement results are probably from reflection due to discontinuities in the device. Figure 2.18 summarizes variation of simulated /measured S_{21} at 6 GHz with different λ/4 section metal thicknesses. The results show that a 25 dB cancellation performance improvement is obtained by adjusting the metal thickness of the λ/4 section.

2.4.3.2 Measurement of Small δε

Equation (2.18) shows that when the two identical PDMS channels are filled with the same materials, then $S_{21(MUT)} = S_{21(REF)}$. Thus, $S_{21} = 0$ when there is no loss difference between the λ/4 and 3λ/4 sections. As a result, the background signal is completely cancelled. If $S_{21(MUT)} \neq S_{21(REF)}$, their difference will appear at port 2, then $S_{21} \neq 0$. As a result, very small difference between the two PDMS channels can be detected since the background is dramatically reduced. A set of ethanol-water mixtures is prepared with very low concentration levels in terms of molar fractions x_e compared with the mixtures in [39]. The REF PDMS channel residing in the bottom path is filled with reference solution, deionized (DI) water in this case; the MUT PDMS channel residing in the top channel is filled with different sample solutions. Figure 2.19 shows the S_{21} responses to the ethanol-water mixtures. Good cancellation performance, ~56 dB, is observed when both channels are filled with DI water. Dielectric property changes in MUT cause the f_m

frequency shift and signal level change at the design frequency. Both changes can be used as sensing indicators of dielectric property changes as have been in Ref. [16] and Ref. [22]. The observed large f_m shift and signal level change at 6 GHz for the mixtures, summarized in Table 2.4, indicate the high measurement sensitivity ($\delta\varepsilon$). Signal level change at the design frequency can be simply explained using symmetry of the permittivity of the solutions inside two PDMS channels. When the MUT PDMS channel is filled with ethanol-water mixtures, the permittivity of the mixture deviates from the DI water permittivity. The symmetry of the structure is destroyed. Higher concentration levels induce bigger permittivity change, therefore, higher S_{21} at design frequency and larger f_m shift.

2.4.4 Discussions and Conclusions

For the device in Figure 2.16 (a), two attached PDMS channels do not yield obvious cancellation level change. However, when two attached PDMS channels are filled with DI water, observed S_{21} is about -56 dB at f_m, not about -66 dB shown in Figure 2.18. The deterioration of cancellation level is caused by asymmetries of the PDMS microfluidic channels. The asymmetry is manifested by large permittivity of water. Therefore, better symmetry in microfluidic channel fabrication and attachment should be explored to exploit the sensitivity potentials of the microwave sensors.

As shown in Figure 2.20 (a) (type A), the microwave device in Figure 2.16 (a) uses the top space of microstrip lines for MUT detection. This configuration is not sensitive to MUT since the microwave filed of the microstrip line is mainly concentrated between the signal line and the ground. Therefore, interaction between microwave field and MUT is weak. As a result, the sensitivity of the developed sensor is relatively low. Other transmission lines, such as a coplanar waveguide (CPW) in Figure 2.20 (a) (type B), have stronger interactions between microwave fields and MUT. Such interaction improvement was discussed and compared in [41]. A different microstrip line configuration, such as the one in Figure 2.20 (a) (type C) in which MUT is placed between the signal line and the ground, will also improve device sensitivity. The arrangement is similar to that of the capacitor sensor in [35]. For comparison purposes, assume the MUTs are ethanol-water mixtures with different molar fractions. Their permittivity ε' can be estimated using the equations in [34]. Effective permittivity ε'_{eff} is then estimated for MUTs under above three types of device configurations using equations in [42, 43]. Transmission line dimensions are chosen to be similar to those of our fabricated devices for sensitivity comparison purpose. Conductor width W = 36 mil, h_{MUT} = 350 μm, substrate is the Pyrex 7740 wafer with h = 500 μm. For CPW, the space between signal and ground conductor S = 4 mil in order to have a characteristic impedance Z_0 = 50 Ω when there are no mixtures. Figure 2.20 (b) shows that type A, which is the one used in our proposed device, is the least sensitive configuration among these three. Change of effective permittivity ε'_{eff} is less than 0.01 when MUT is changed from pure water to pure ethanol, and the change of effective permittivity ε'_{eff} is 21.49 and 41.83 for type B and type C configuration, respectively. If everything else is the same, type B is about 2100 times more sensitive than type A. Type C is about 4100 times more sensitive. It is also observed that type C configuration has higher sensitivity if h_{MUT} is thinner (e.g., h_{MUT} = 10 μm), which is a desired characteristic since thinner one is easier to be fabricated and needs smaller MUT volume. Considering type A is already more sensitive than the ultra-sensitive sensor in [22], the proposed microwave sensors have the potential to be super sensitive when type B and C configurations are used.

In conclusion, we have demonstrated that adjusting metal thickness of the $\lambda/4$ section of the rat-race hybrid ring can compensate loss differences of the proposed microwave sensor in [39] to greatly improve parasitic signal cancellation level. As a result, sensor sensitivity is significantly improved. We have also showed that the sensor sensitivity can be further improved dramatically by using transmission lines sensing configurations that have stronger couplings. Furthermore, fabrication and testing processes of the on-chip sensor are described.

ACKNOWLEDGMENT

We would like to thank financial support from NSF (#ECCS-0703042). Part of the fabrication was conducted at the Cornell NanoScale Science & Technology Facility (CNF), Cornell University.

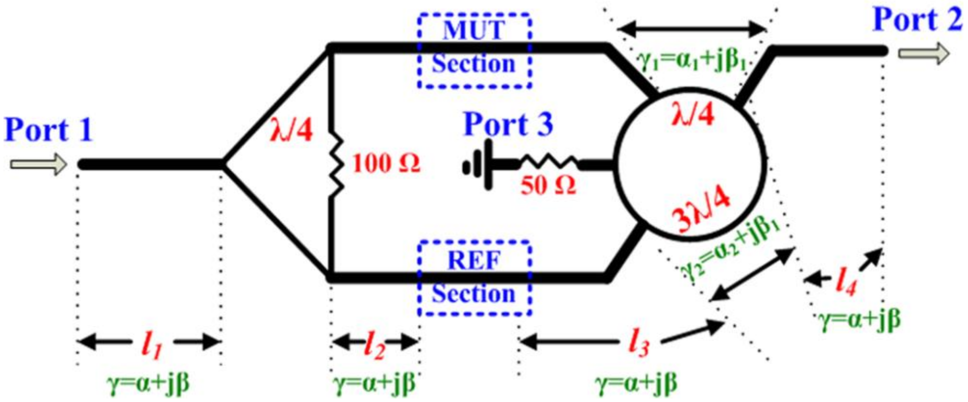

Figure 2.15: Schematic of proposed high sensitivity microwave sensing device. Dashed square boxes indicate sections where PDMS microfluidic channels are attached for Material Under Test (MUT) and Reference Material (REF).

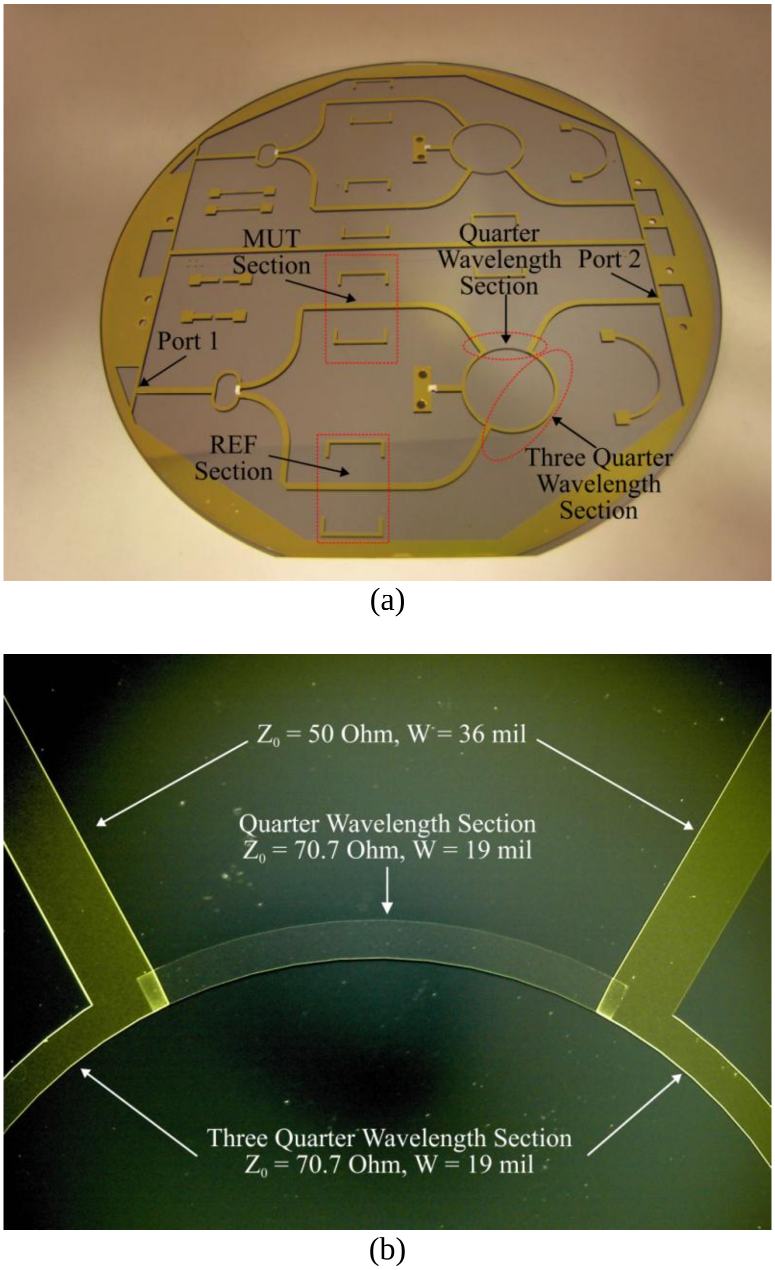

Figure 2.16: (a) Photo of microwave device without PDMS microfluidic channels attached. (b) Zoom-in microscope image of thickness-tuned λ/4 section shown in (a).

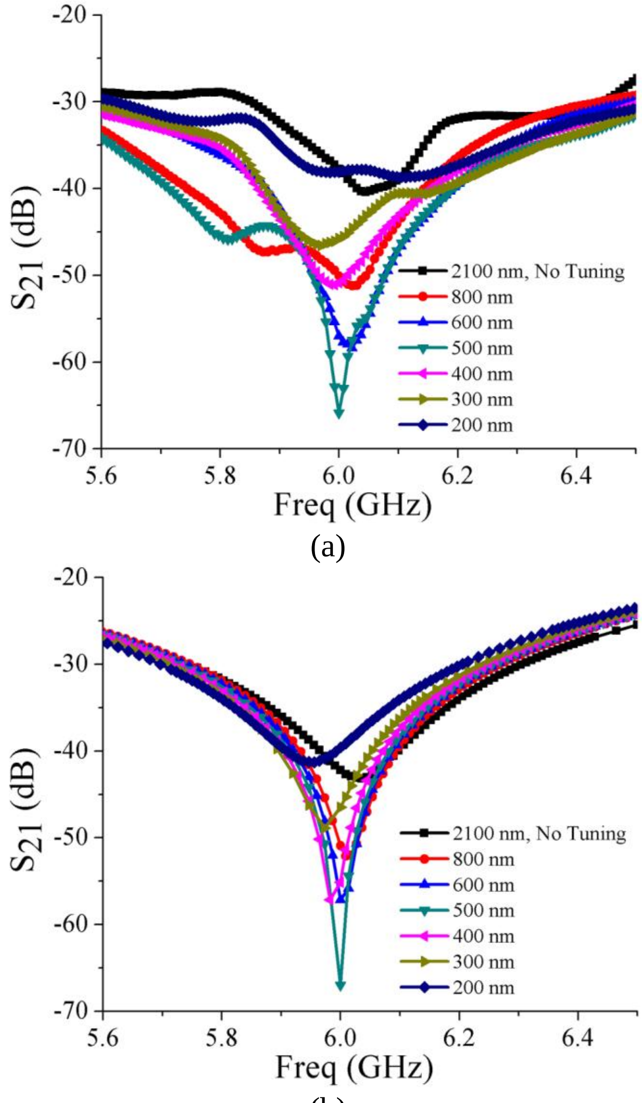

(a)

(b)

Figure 2.17: Loss compensation results with different metal thickness on λ/4 section of hybrid ring. (a) Measured. (b) ADS simulated.

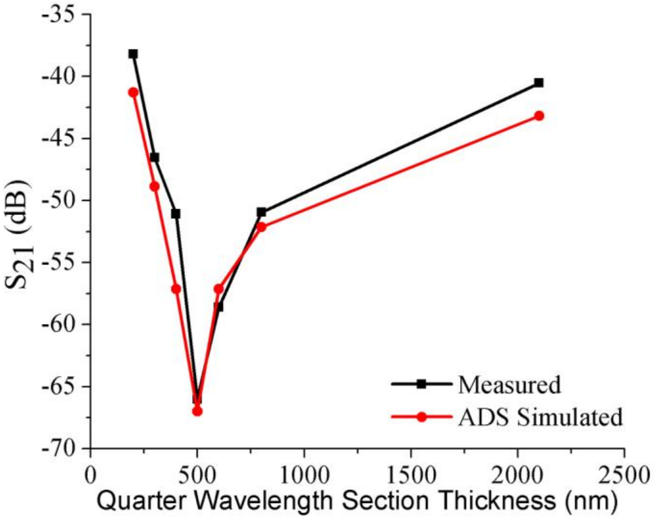

Figure 2.18: Variation of S_{21} at 6 GHz with different metal thickness on λ/4 section of hybrid ring.

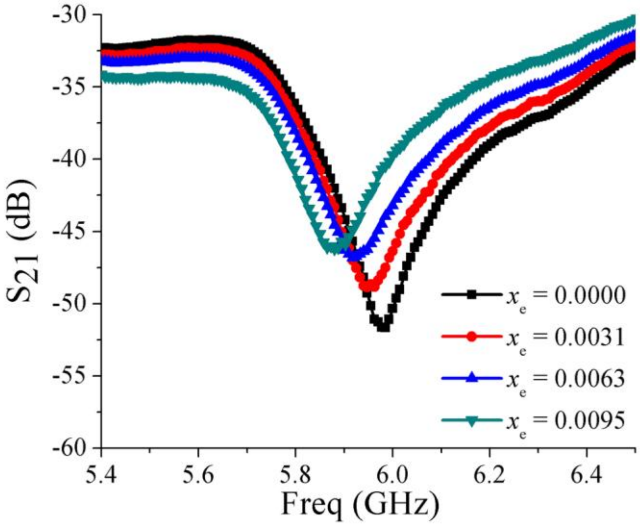

Figure 2.19: Measured S_{21} for ethanol-water mixtures with very small molar fractions.

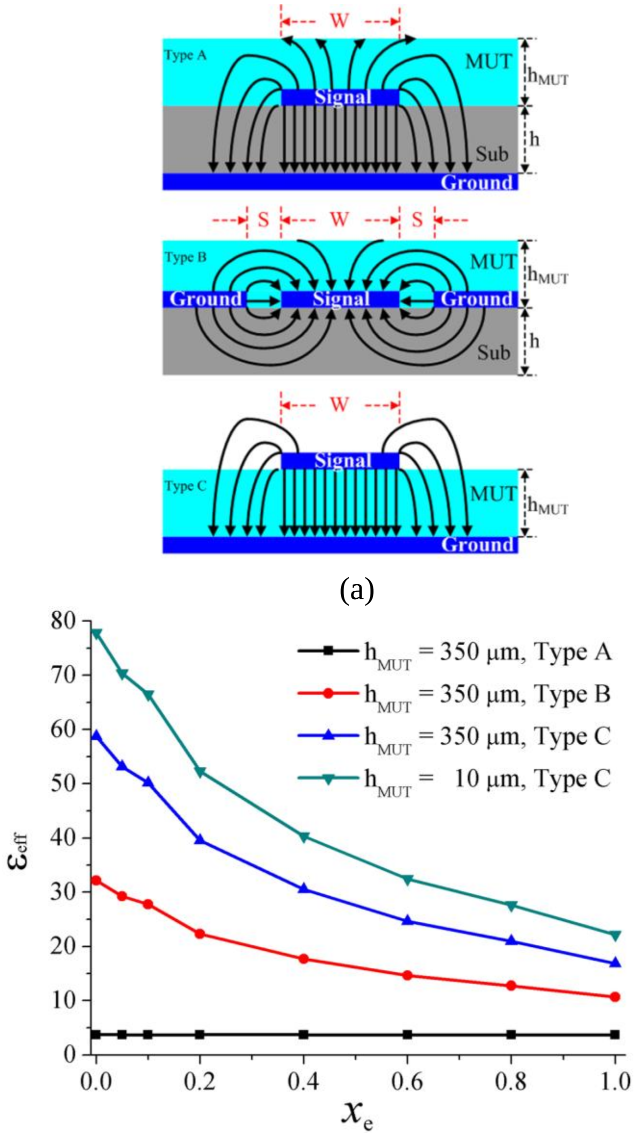

(a)

(b)

Figure 2.20: (a) Electric field distributions of three device configurations: MUT on top of a microstrip line (Type A), MUT on top of a coplanar waveguide CPW (Type B) and MUT on bottom of a microstrip line (Type C). (b) Variation of effective permittivity ε'_{eff} with ethanol-water mixture molar fraction x_e for different device configurations.

Table 2.3: Thickness of $\lambda/4$ section of hybrid ring

Device #	Thickness t_1 (nm)
1	2100
2	800
3	600
4	500
5	400
6	300
7	200

Note: Measured conductivity σ of metal stack is 1.6×10^7 S·m^{-1}, then skin depth δ_s is calculated as 1.6 μm at 6 GHz.

Table 2.4: Measured change of S_{21} at 6 GHz and shift of f_m for ethanol-water mixtures with small molar fractions

Molar Fraction x_e	[a]Change of S_{21} (dB) at 6 GHz	[b]Shift of f_m (MHz)
0.0000	0	0
0.0031	3.96	38
0.0063	7.14	68
0.0095	10.62	105

Note: [a]Change of S_{21} (dB) = $S_{21}(x_e) - S_{21}(x_e = 0)$.

[b]Shift of $f_m = f_m(x_e = 0) - f_m(x_e)$.

CHAPTER THREE

RADIO FREQUENCY MICROFLUIDIC DEVICES FOR MEASUREMENTS OF HIGH DC ELECTRIC FIELD EFFECTS ON DIELECTRIC PROPERTIES OF WATER

3.1 Microwave Dielectric Property Measurements of On-Chip Liquid Films

3.1.1 Introduction

Microwave dielectric spectroscopy, which measures the frequency responses of polarized molecules and charged molecules, has been one of the most reliable techniques for investigating bulk liquid dynamic relaxation and dynamic structures [44]. The method is also promising for on-line biomedical and chemical sensing due to its unique characteristics [16, 24, 45]: proteins and other biological molecules have rather large and distinct dielectric properties in microwave spectrum; ionic contributions to the conductivity of water under most physiologically useful systems is greatly diminished. Furthermore, rapid development of inexpensive integrated microwave systems in CMOS technology is expected to provide an ideal platform, such as the proposed network-analyzer-on-chip [46], for broad applications of this technology. The method may also be developed to provide lab-on-a-chip [47], a versatile, sensitive and selective scheme for analyte and process sensing with signal transduction capabilities. As a result, (analyte) liquids need to be incorporated with on-chip microwave sensing structures, such as microstrip lines. One of the challenges therein is the microstrip-line based dielectric measurement methodology when standard silicon substrate in CMOS technology, instead of lossless glass substrate [16, 24, 45], is used.

The incorporation of liquids on-chip is not only for convenience (such as system integration with less sample consumed), but also of necessity since many bio-chemical interaction processes involve liquid thin films and/or confined liquids, which have characteristics different from that of bulk liquids. The differences are caused by the confinement and surface interactions, such as surface tensions.

In this section, we report our preliminary results on microwave dielectric property characterization of on-chip liquid films, including ethanol-water mixtures and glucose-water mixtures at different concentration.

3.1.2 Dielectric Property Extraction

Figure 3.1 shows a schematic of an on-chip microstrip-line-based sensing structure. Blue lines indicate aluminum microstrip line structures. Yellow lines indicate walls for liquid confinement, which are made out of photo resist. Special caution is needed when measuring ethanol related liquids.

Figure 3.2 is a generic equivalent circuit model of on-chip transmission line. Line parameters can be obtained through $R = \mathrm{Re}\,(\gamma Z)$, $G = \mathrm{Re}\,(\gamma/Z)$, $L = \mathrm{Im}\,(\gamma Z)/\omega$, $C = \mathrm{Im}\,(\gamma/Z)/\omega$, where γ (propagation constant) and Z (characteristic impedance) of the transmission line can be extracted from S-parameters [48].

There are multiple dielectric layers for the microstrip line shown in Figure 3.1. Assume quasi-TEM mode wave propagation and linear, homogenous and isotropic dielectric layer, then effective dielectric constant, $\varepsilon_{eff} = \varepsilon_{eff}^{'} - j\varepsilon_{eff}^{''}$, can be expressed in terms of line parameters C and G.

$$\varepsilon_{eff}^{'} = CZ_0^{air}\upsilon_p \tag{3.1a}$$

$$\varepsilon_{eff}^{"} = \frac{G}{C\omega}\varepsilon_{eff}^{'} = GZ_0^{air}\upsilon_p / \omega \tag{3.1b}$$

Here C and G are total line capacitance and conductance per unit length with existence of multiple dielectric layers, respectively. Z_0^{air} is impedance when replacing dielectric layers by air. υ_p is phase velocity of light in vacuum. ω is radian frequency.

For microstrip line with double-layer substrate, capacitance of each layer is connected in series fashion and equivalent dielectric constant ε_{eq} of double-dielectric-layer substrate is given in [49]. Thus,

$$\varepsilon_{eq} = \frac{d_{SiO_2} + d_{Si}}{d_{SiO_2} \big/ \varepsilon_{SiO_2} + d_{Si} \big/ \varepsilon_{Si}} \tag{3.2}$$

where

$d_{SiO_2} = \dfrac{K(k_1)}{K^{'}(k_1)}$, and $d_{Si} = \dfrac{K(k)}{K^{'}(k)} - \dfrac{K(k_1)}{K^{'}(k_1)}$

$k_1 = \dfrac{1}{\cosh(\frac{\pi w}{4h_1})}$, and $k = \dfrac{1}{\cosh(\frac{\pi w}{4h})}$

$k^{'} = \sqrt{1-k^2}$, and $k_1^{'} = \sqrt{1-k_1^2}$

$h_1 = h_{SiO_2}$, and $h = h_{SiO_2} + h_{Si}$

w is width of microstrip line,

$K(k)$ is complete elliptic integral of the first kind.

A simple expression of effective dielectric constant ε_{eff} of multilayer microstrip line has been derived using conformal mapping method in [50]. For our narrow microstrip (w/h <<1), we get

$$\varepsilon_{eff} = \varepsilon_{eq} q_1 + \varepsilon_{Fluid} \frac{(1-q_1)^2}{\varepsilon_{Fluid}(1-q_1-q_2)+q_2} \tag{3.3}$$

where

$$q_1 = \frac{1}{2} + \frac{0.9}{\pi \cdot \ln \frac{h}{w}}$$

$$q_2 = \frac{1}{2} - \frac{0.9 + \frac{\pi}{4} \ln(\frac{h_2/h+1}{h_2/h+w/4h-1})}{\pi \cdot \ln \frac{8h}{w}} \cdot \arccos\left\{\left[1-\frac{h}{h_2}(1-\frac{w}{8h})\right] \cdot \sqrt{\frac{h_2/h+1}{h_2/h+w/4h-1}}\right\}$$

$$h_2 = h_{SiO_2} + h_{Si} + h_{Fluid}$$

Finally, by substituting (3.1) and (3.2) into (3.3), we get

$$\varepsilon_{Fluid} = \frac{q_2(\varepsilon_{eq} q_1 - \varepsilon_{eff})}{(1-q_1-q_2)\cdot(\varepsilon_{eff} - \varepsilon_{eq} q_1) - (1-q_1)^2} \tag{3.4}$$

3.1.3 Results and Discussions

Figure 3.3 and Figure 3.4 show Cole-Cole diagrams for ethanol-water and glucose-water mixtures at room temperature. ε' and ε'' are real and imaginary part of the dielectric constant, respectively, obtained by use of (3.4). Semicircle curve indicates a single relaxation time, and deviation from the semicircle implies a relaxation time distribution. The results also show that there are distinctively different dielectric properties for different liquids, including liquid mixtures at different concentrations. The higher concentration level is, the smaller radius of the semicircle is, which indicates different molecular interaction.

3.1.4 Conclusions

In conclusion, a microwave characterization method for on-chip liquid film dielectric property measurement is developed. Microstrip-line-based on-chip test devices are fabricated to characterize the microwave dielectric properties of various on-chip liquid films: binary mixtures of DI water with ethanol and glucose. The obtained microwave dielectric properties are presented in Cole-Cole diagrams. Different concentration of ethanol-water mixtures and glucose-water mixtures shows different dielectric characteristics, which provides a promising and inexpensive on-chip sensing mechanism for biomedical and chemical applications. Issues that need to be further exploited are: (i) to develop more accurate de-embedding procedures, such as multi-line de-embedding [51] even though the method requires larger chip areas; (ii) to develop more sensitive test structures. Current test-structures use only part of the electric fields; (iii) liquid confinement arrangement need to be further improved.

ACKNOWLEDGMENT

We would like to thank Dr. Jena Steinle for providing bio-samples.

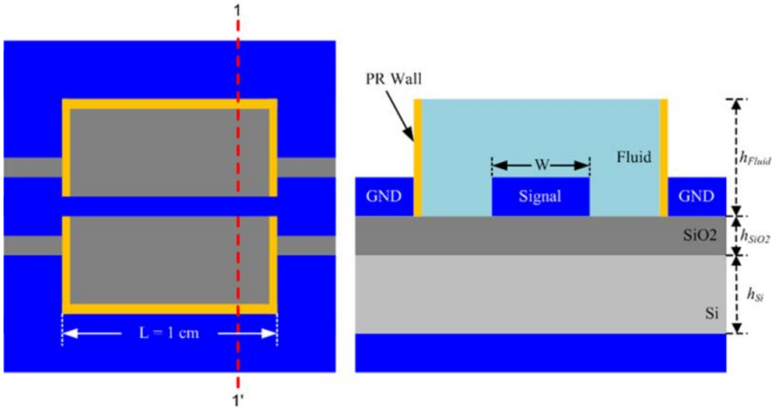

(a) (b)

Figure 3.1: Schematic of an on-chip microstrip-line-based test structure. (a) Top view. (b) Cross-section view at plane 1-1'. Drawing not to scale.

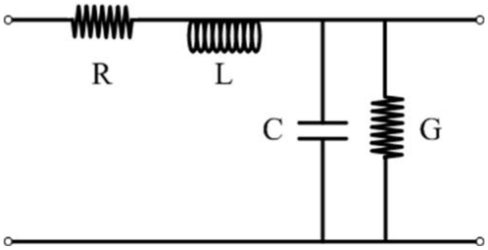

Figure 3.2: A generic high frequency equivalent circuit model of on-chip transmission line.

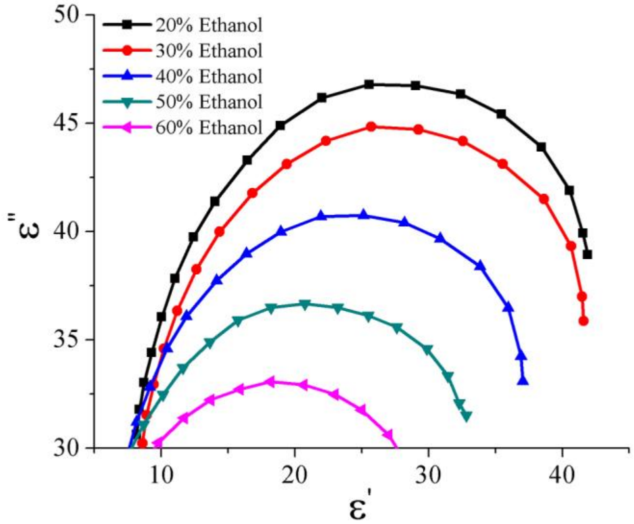

Figure 3.3: Cole-Cole diagram for five ethanol-water mixtures at room temperature.

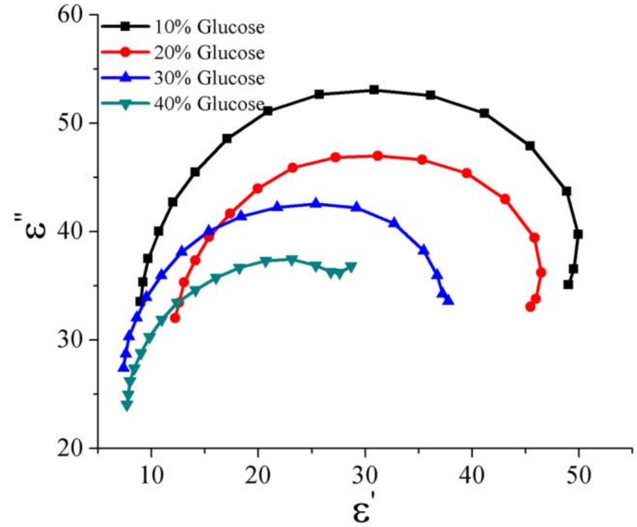

Figure 3.4: Cole-Cole diagram for four glucose-water mixtures at room temperature.

3.2 Dielectric Breakdown of Water Subjected to Uniform DC Electric Field Measured with Radio Frequency Microfluidic Devices

3.2.1 Introduction

Due to its high permittivity and high dielectric strength, water is a good dielectric medium for pulsed power systems [52], for which water dielectric properties, including electrical breakdown properties, are of great interest. The study of such properties started more than a century ago, yet there are still ongoing efforts to understand them. This is because the omnipresent water is a complex fluid and new applications of water keep emerging. For instance, water breakdown at a 50 µm gap under microsecond and sub-microsecond electrical voltage pulses was recently reported in [53] for bioelectronics system development. Common to all previous water breakdown experiments are (i) sphere electrode geometry is usually involved, where non-uniform field distribution is formed. Therefore, obtained breakdown voltage and electric field is geometry dependent; (ii) the electrode gaps are large even though a 50 µm gap was used in [53], which is the smallest electrode gap that has been tested for breakdown purposes so far. Large electrode gap complicates characterizations and understanding of water breakdown processes, including controversial initiation process, since micro-bubbles and impact ionization can coexist. Therefore, new approaches need to be developed to understand water dielectric properties, especially water breakdown processes. Miniaturizing the electrode gap to reduce applied voltage level for breakdown is one possible approach. In this section, we report our initial results on water breakdown with a ~ 300 nm planar microfluidic channel in which DC electric field is also uniform.

3.2.2 Device Fabrication and Experimental Setup

Figure 3.5 illustrates schematics of top view and cross section view of proposed test structure for water breakdown probing. A gold (Au) microstrip signal line and a platinum (Pt) ground plate act as electrodes. A 300 nm gap between them is filled with water, which is subjected to a uniform DC electric field from an externally applied DC voltage across the gap.

There are three main steps in device fabrication: bottom wafer fabrication, top wafer fabrication and wafer bonding.

Bottom wafer is a 4-inch in diameter, 550 μm thick Si wafer with 1 μm thick thermal SiO_2. First, a 500 nm thick Pt thin film is evaporated as ground plate with a 10 nm thick Titanium (Ti) as adhesion layer. A three-mask process then follows. A 150 nm thick Plasma-Enhanced-Chemical-Vapor-Deposition (PECVD) SiO_2 is grown to be the insulating layer of the device and its thickness will be part of the gap thickness. Dielectric strength of the PECVD oxide is ~ 10 MV/cm. A trench is formed by use of standard photolithography steps and CHF_3/O_2 SiO_2 anisotropic Reactive-Ion-Etching (RIE) processes, which forms straight sidewalls necessary to avoid potential oxide breakdown complications. Via holes are then formed with standard photolithography steps and SiO_2 wet etch via buffered-Oxide-Etchant (BOE). Sloped sidewalls of via holes are desired for continuous metal connection along the sidewall in later Au deposition. Figure 3.6 shows SEM images on top view and cross section view of via hole with sloped sidewall. Finally, metallization of signal pads and ground pads, a 10 nm thick Ti adhesion layer and a 150 nm thick Au layer, is finished through standard photolithography and lift-off processes.

Top wafer is a 4-inch in diameter, 300 μm thick double-side-polished (DSP) Si wafer with 1 μm thick thermal SiO_2. A stack of Ti (10 nm) / Au (150 nm) signal line with width of 20 μm and length of 1 mm is fabricated on the top wafer through standard photolithography and lift-off processes. Windows need to be opened for two purposes, including probe access to signal/ground pads that are on the bottom wafer, inlet and outlet formation for liquid sample injection. Deep RIE Si etch (Bosch process) is used to etch through the 300 μm thick Si wafer with SiO_2 as etching mask.

An Au-Au thermo-compression bonding [54] is applied to bond the top wafer and the bottom wafer together. Thus the etched trench on the bottom wafer is sealed by the top wafer, and then a 300 nm gap is formed. A complete microstrip line structure is formed by conductive contact between the signal pad on the bottom wafer and the signal line on the top wafer. Photos of the bonded wafer and microscopy images of fabricated devices are shown in Figure 3.7.

An HP8510C network analyzer is used as a breakdown indicator together with a Cascade probe station. Ground-Signal-Ground (GSG) probes are used to measure scattering parameters of microstrip line with water or air as substrate under high frequency and DC electric field. It is worth to be noted here that the same setup can also be used to study non-linearity of water under high electric field stress. A full two-port Short-Open-Load-Thru (SOLT) calibration procedure is conducted before taken measurements. Reservoirs made by nylon shoulder spacers and Polydimethylsiloxane

(PDMS) [55] are attached into inlet/outlet for deionized (DI) water injection. DC voltages from a Keithley 2612 System Source Meter are applied across the Au microstrip signal line (+V) and the Pt ground plate (-V).

3.2.3 Results and Discussions

Possible air breakdown and contact pads breakdown are examined first when there is no water injected into the channel. High frequency measurements are conducted at different DC voltages up to 38 V, which corresponds to a field intensity of 1.27 MV/cm. No breakdown is observed over applied voltage range. Typical measured transmission coefficient S_{21} is shown in Figure 3.8 (a). Voltage polarities are also reversed, and no polarity effect is observed. The measurement instruments prevent the use of higher voltages. Nevertheless, the 1.27 MV/cm field is much higher than conventional air dielectric strength which is in a range from ~30 kV/cm to ~100 kV/cm. This increase of air dielectric strength can be explained by "*pd* scaling"[56], breakdown voltage depends on product of pressure *p* and electrode separation *d* even though the 300 nm gap is still a few mean-free-path long. The results indicate that air breakdown is much more difficult to occur for a small gap.

DI water with a resistivity of 16 MΩ·cm is then injected into the channel. Similar measurements are conducted. Figure 3.8 (b) shows measured S_{21} for different applied voltages. It shows that there is no visible difference in S_{21} when the applied voltage is below 3 V. However, when the applied voltage is increased to 3 V, the S_{21} is observed to increase ~10 dB right after voltage applies, and then suddenly decreased to -80 dB, which indicates a broken circuit. Measured DC resistance between the microstrip line and the ground is ~37 Ω, a dramatic drop from MΩ range for DC voltages below 3 V. The significant drop of DC resistance indicates a short to ground. Thus water breakdown occurs under the current system setup when a voltage of 3 V is applied, which corresponds to an electric field of 100 kV/cm.

The observed water breakdown voltage is low and the 300 nm gap is small compared with previous breakdown experiments [52, 53, 57-59]. Furthermore, the applied DC field is uniform across the gap, which is different from the field distributions in spherical geometries. To understand the water breakdown processes, we first investigated surface roughness since its effect on the water breakdown may be more pronounced for small gap systems. Both electrode surfaces are deposited through e-beam evaporation. Au evaporation needs some extra cautions due to its easy spitting and then cause rough surface. Longer soaking time and slowly increased power are preferred to alleviate the Au spitting. The use of tungsten crucible can greatly help to solve Au spitting problem [60]. Figure 3.9 shows microscope images of Au surfaces evaporated with or without help of the tungsten crucible. It clearly shows the surface roughness can be improved with the help of tungsten crucible. In addition, different choices of fabrication processes will bring different edge finish for the Au signal line. Figure 3.10 (a) and (b) show Atomic Force Microscope (AFM) images when two common metallization processes, lift-off process and wet-etch process, are applied. Some sharp tips are observed along the Au signal line edges in a 3-D AFM image in Fig. 3.10 (a). These tips (edges) are common to lift-off process. However there are no tips observed along the edges in Figure 3.10 (b) when the Au signal line is formed through wet-etch process, which is more favorable to form smooth edges. Figure 3.10 (c) shows the Au signal line surface with rms. roughness of 2.5 nm. Nevertheless, a few sharp micro protrusions are still observed on flat Au surfaces shown in Fig 3.10 (a) and (b) although the surfaces are thought to be smooth enough with rms roughness of only 2.5 nm. Figure 3.10 (d) shows the Pt ground surface with rms. roughness of 10.4 nm, which is worse than the Au signal line surface because the Pt is more difficult to be evaporated and the thicker Pt film (500 nm) is deposited. Field enhancements at those sharp tips make them critical spots for possible initiation of water breakdown [59, 61].

Two leading theories about water breakdown mechanisms need to be evaluated. The two mechanisms are charge injection at the electrode/water interface [62] and electron impact ionization in a low-density region in water, e.g., a bubble [63, 64]. The first one needs energetic electrons emitted from cathode to go through ionization and multiplication processes for the development of breakdown along the electric field in the gap. Simulation in [63] indicates that the injected electrons are likely to be scattered in a random manner with low energy in liquid water. For our system setup with 300 nm gap, it is unlikely that product of impact ionization coefficient α and gap distance d is large enough for avalanche breakdown process to occur. Thus the first mechanism may not explain the observed breakdown process. The second one may be more favorable. The DI water used in our experiment did not go through any de-aeration process, dissolved air bubbles are believed to pre-exist randomly in water and on the electrode surfaces [65]. The presence of air bubbles strongly affect water breakdown as demonstrated in [66]. Additionally, there is another possibility for bubble generation: hydrogen and oxygen bubbles generated on the Pt and Au electrode surface through electrolysis of pure water. Electrolysis of pure water is very slow due to its small conductivity but can occur due to self-ionization of water. Minimal potential for decomposition of pure water into hydrogen and oxygen at 25 ℃ is only 1.23 V, which is below 3 V in our experiment. In particular, Pt, the material used as one of our electrode, has shown great activity for high efficient water electrolysis. As a result, the micro bubbles will act as micro-charge sources due to enhanced electric field inside them. They may contribute to large plasma creation and multiplication within the water. Existence of the micro protrusions/tips on the electrode surfaces will help to trap micro bubbles, and probably initialize the observed water breakdown.

3.2.3 Conclusions

In conclusion, water dielectric breakdown subjected to uniform DC electric field in 300 nm planar microfluidic channels is experimentally studied. RF test devices with microstrip line configurations are fabricated and the results show that water breakdown occurs at ~ 100 kV/cm electric field under current system setup. The initiation process of water breakdown in a small gap is discussed. It is most likely being initialized by pre-existed bubbles or bubbles generated from electrolysis of water. Electrode surface roughness is examined and it may be a critical factor affecting the observed water breakdown. Therefore, the process for electrode fabrication needs to be carefully chosen and the fabrication procedures need to be optimized to provide smooth surfaces without sharp tips or micro protrusions for future water breakdown investigations.

ACKNOWLEDGMENT

The fabrication is conducted at the Cornell NanoScale Science & Technology Facility (CNF) in Cornell University and the Microelectronics Research Center (MiRC) in Georgia Institute of Technology.

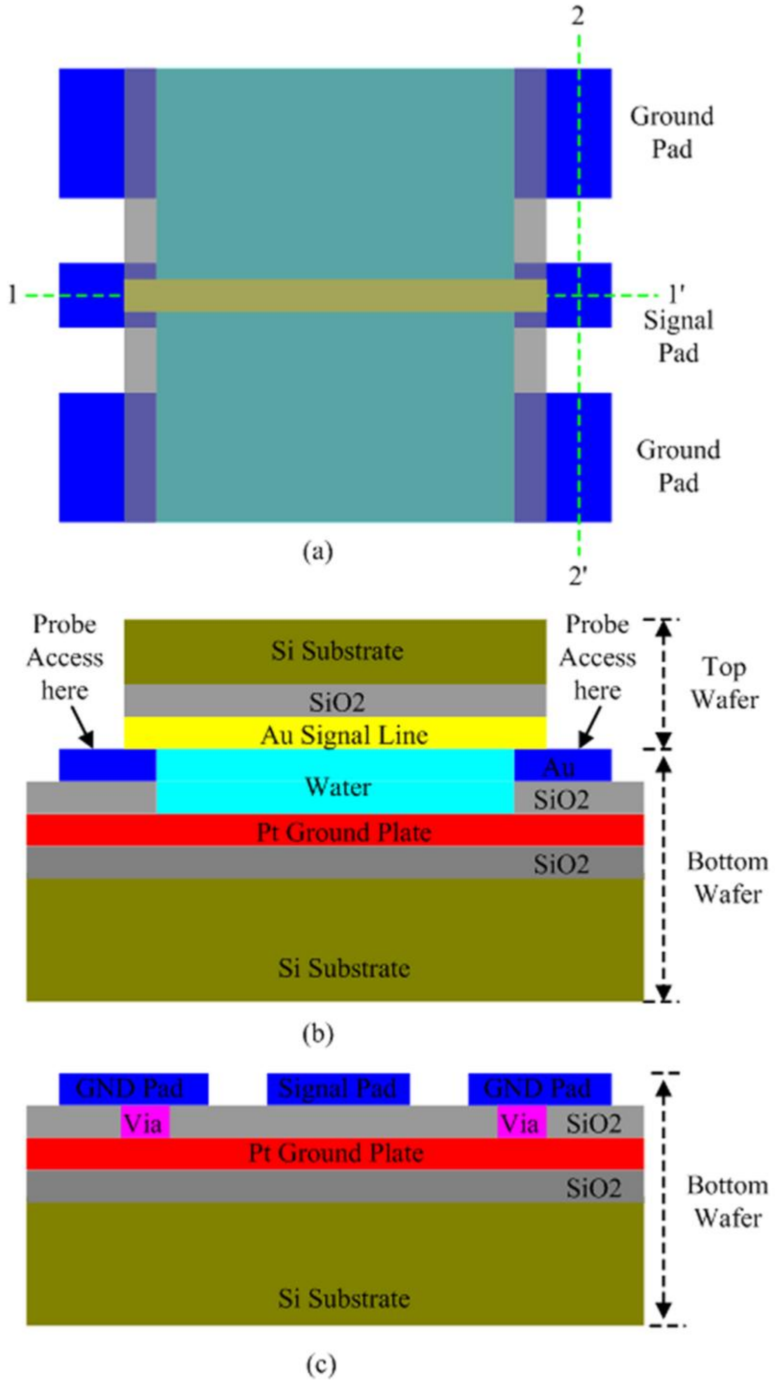

Figure 3.5: Schematic of RF microfluidic device. (a) Top view. (b) Cross section view at plane 1-1΄. (c) Cross section view at plane 2-2΄.

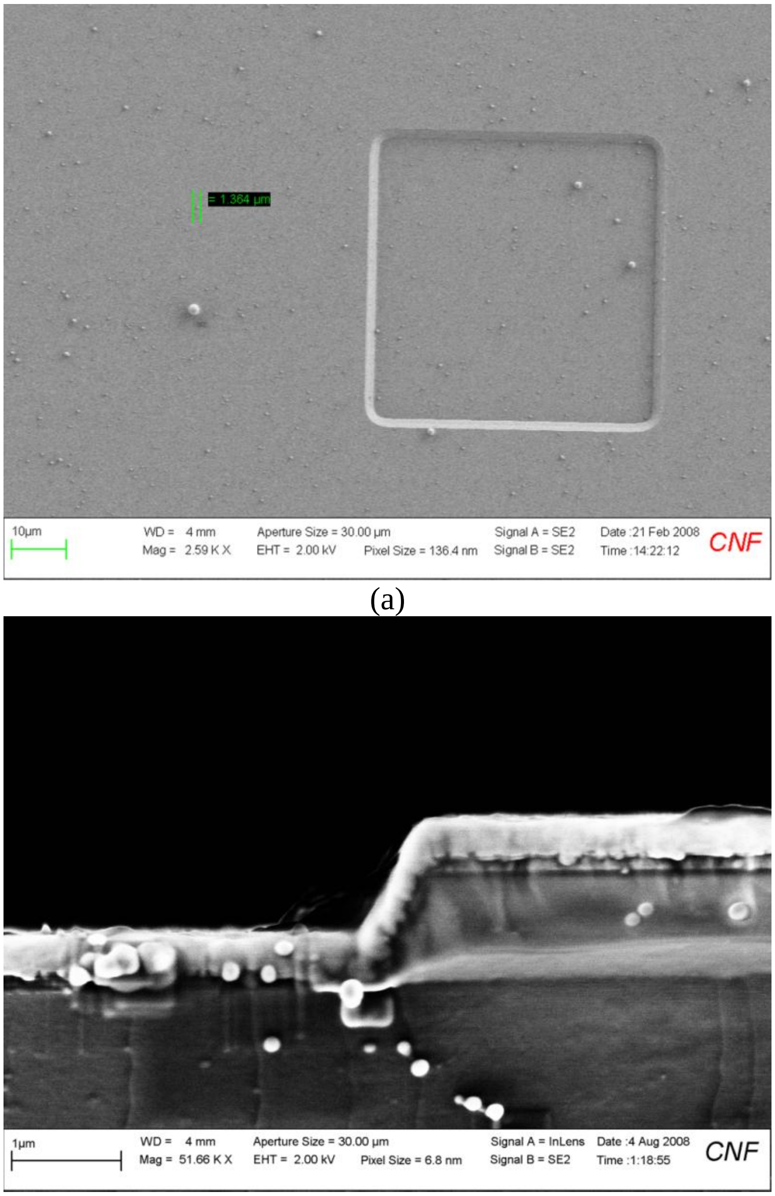

(a)

(b)

Figure 3.6: SEM images of a via hole with sloped sidewall. (a) Top view. (b) Cross section view.

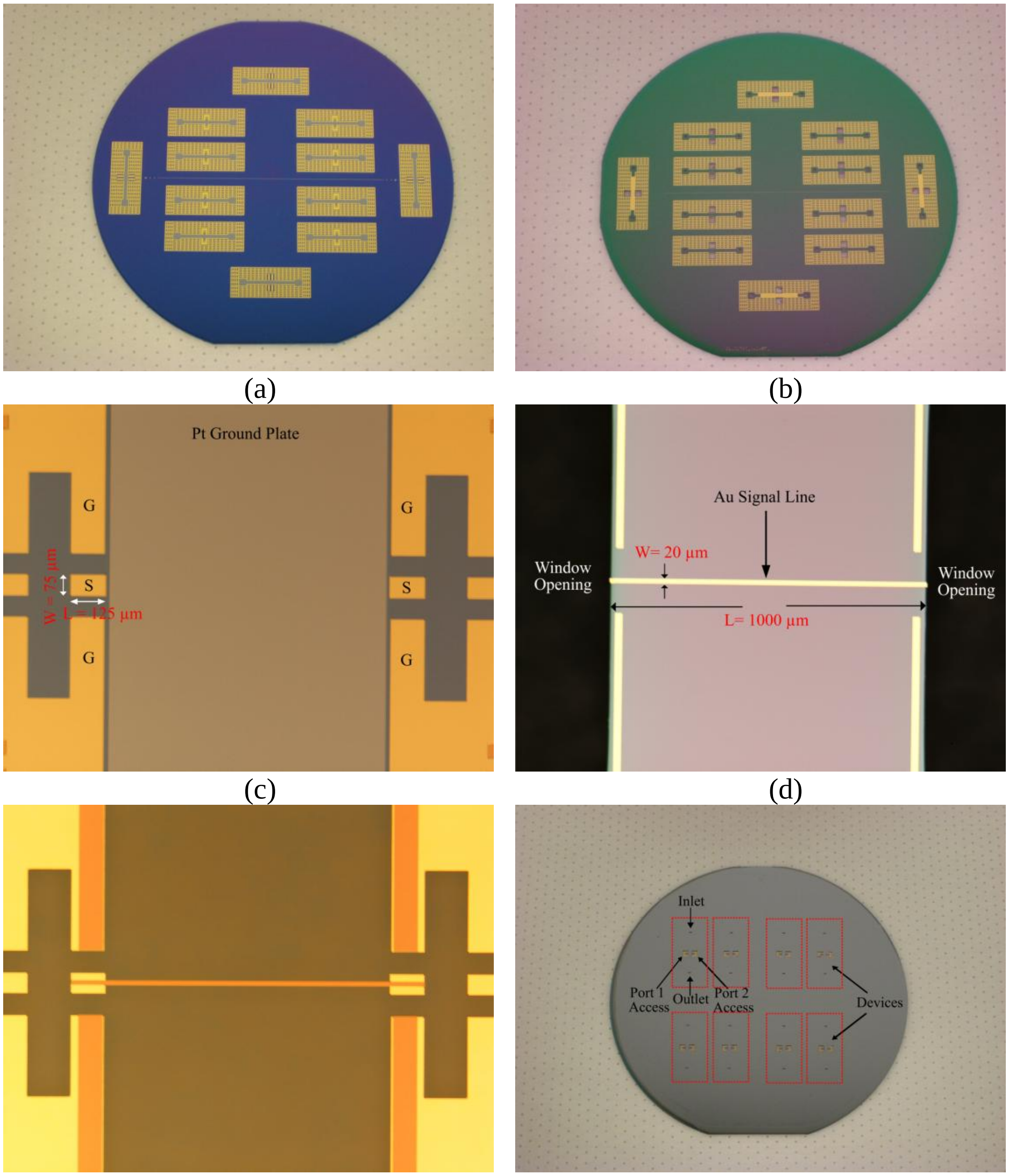

(a) (b)

(c) (d)

(e) (f)

Figure 3.7: Photos of fabricated (a) bottom wafer and (b) top wafer. Microscopy images of device fabricated (c) in the bottom wafer and (d) in the top wafer. (e) Microscopy image of bonded device. Pyrex glass substrate is used for visualization purpose. (f) Photo of bonded wafers. Eight devices are included.

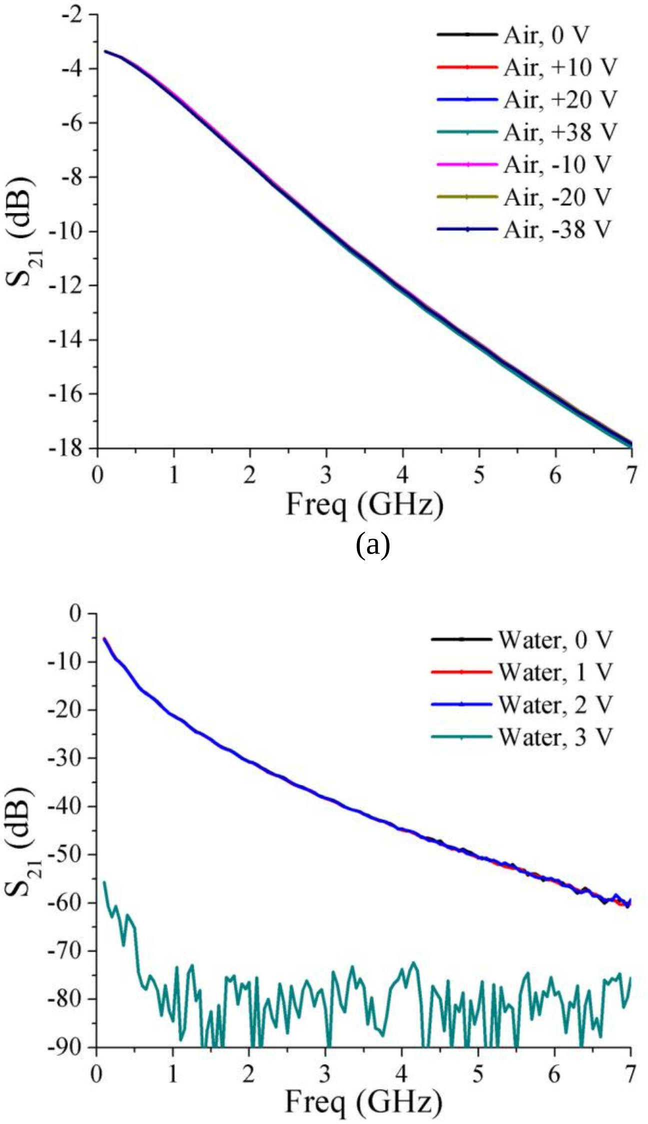

(a)

(b)

Figure 3.8: Measured S_{21} for different applied voltages for (a) air filled channel and (b) water filled channel.

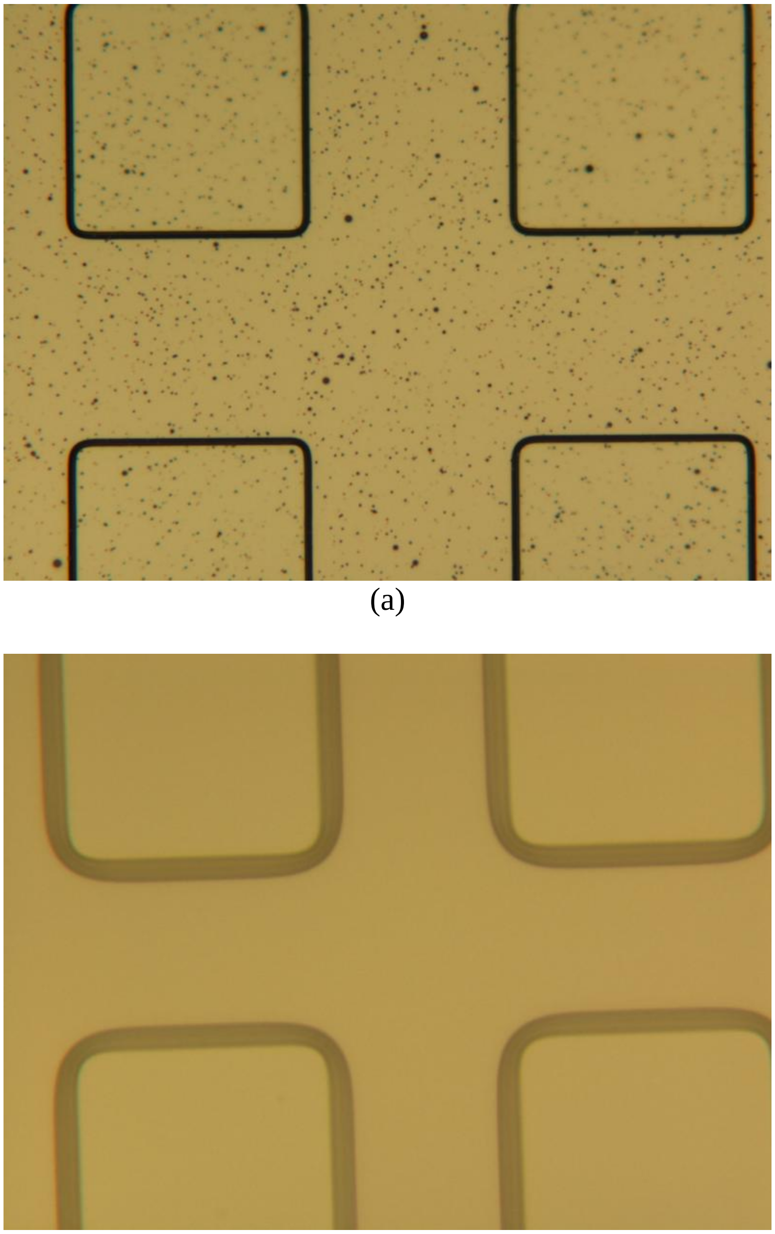

(a)

(b)

Figure 3.9: Microscope images of evaporated Au surfaces (a) without the help of tungsten crucible and (b) with the help of tungsten crucible.

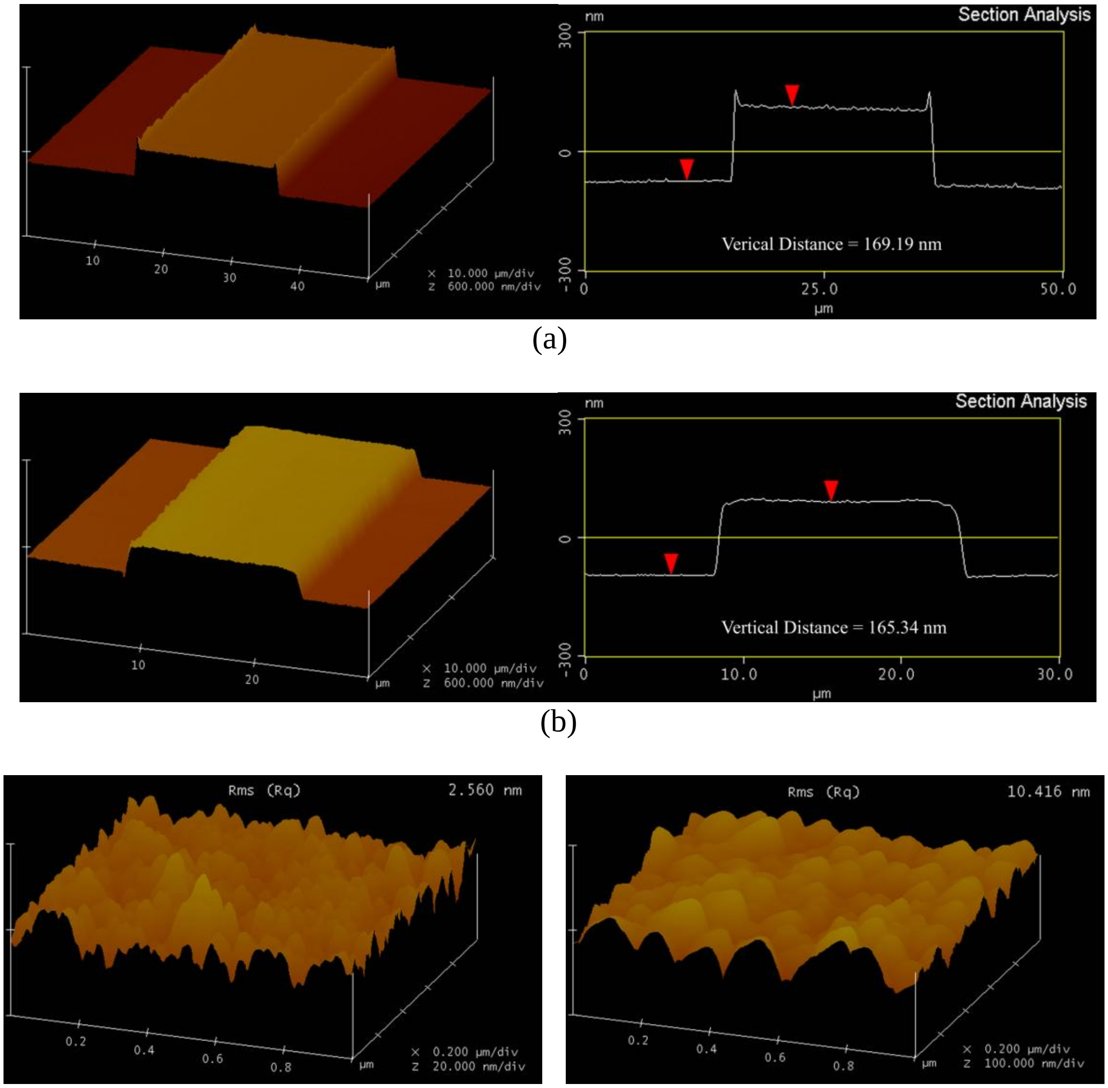

(a)

(b)

(c) (d)

Figure 3.10: AFM 3-D images and their section analysis of Au electrode fabricated through (a) lift-off process and (b) wet-etch process. Some sharp tips are observed along the Au edges when lift-off process is used. (c) AFM 3-D images of Au electrode surface with rms. roughness of 2.5 nm. (d) AFM 3-D images of Pt electrode surface with rms. roughness of 10.4 nm.

3.3 High DC Electric Field Effects on Microwave Dielectric Properties of Water Measured with Radio Frequency Microfluidic Devices

3.3.1 Introduction

Radio frequency (RF) and microwave dielectric properties of water under high electric fields, i.e., dielectric saturation of water, are essential for the understanding of a wide range of systems. For instance, such water plays a critical role in protein systems [67], ion-DNA interactions [68], thin films of aqueous electrolytes, ionic solutions within charged membrane pores [69, 70] and cell membranes [71]. They are also important in the estimation of ion salvation free energy. In these studies, the dielectric saturation of water is usually introduced in Poisson-Boltzmann equation by means of the Booth theory [72]. Furthermore, water dielectric properties are important for the development of compact pulsed power systems where water is a principal dielectric medium [73, 74].

Experimental investigations of water dielectric saturation include a widely quoted work that achieved a field intensity of ~ 150 kV/cm with a ~ 6 μs electrical pulse at a measuring frequency of ~ 10 MHz [75]. More recently, Kerr-effect was used to measure water dielectric permittivity with 20 ns electrical pulses applied between a hemispherical and a plane electrode [76]. Up to 4 MV/cm peak electrical fields were obtained. Water refractive index change at 474 terahertz was observed. Despite these results, experimental studies of water dielectric saturation are technically very difficult [67, 77]. Challenges include introducing uniform, high electric fields across water samples without causing water breakdown and temperature change while enabling use of sensitive test equipments. For instance, it is well known that breakdown happens at a DC field of ~

100-200 kV/cm in experimental setups filled with deionized (DI) water [78, 79]. The field intensity is far below 1-10 MV/cm at which significant saturation effects occur [67, 77]. On the other hand, commercial vector network analyzers (VNA), which are standard instruments for dielectric spectroscopy characterizations of materials, are limited to 40 V DC voltages [80]. The voltage restriction prohibits the use of VNAs in high-voltage systems that have been developed for water dielectric saturation studies. As a result, most of water dielectric saturation work is conducted either theoretically or through computer simulations. Consequently, various water dielectric permittivity values, from 5 to 80, have been suggested in different research efforts [67]. Contradictions may arise as well. For instance, a molecular dynamics (MD) simulation [77] shows ~ 50 % DC water permittivity reduction when a 5 MV/cm DC electric field was applied while a ~ 100 MV/cm DC field was needed for water dielectric saturation to occur in another MD simulation [81].

In this section, we develop a RF microfluidic device and investigate water dielectric saturation effects under GHz range. We report our fabrication and characterization of the devices as well as our measurement results of DI water at ~ 1 MV/cm DC electric field levels.

3.3.2 Device Fabrication and Experimental Setup

3.3.2.1 Device Design and Configuration

Figure 3.11 shows schematics of top view and cross section view of the proposed RF microfluidic device.

Heavily doped silicon wafers are used to build electrodes to support high DC electric fields while forming microwave transmission lines for DI water dielectric property characterization under GHz range. A silicon-on-insulator (SOI) wafer is used as bottom wafer, which has a 25 µm thick n-type device layer (resistivity of 0.001-0.002 Ω·cm) and a 1.5 µm thick oxide layer. Top wafer is a double-side-polished (DSP) p-type Si wafer with thickness of 350 µm and resistivity of 0.001-0.002 Ω·cm. A ~260 nm deep, 75 µm wide and 500 µm long Si trench is patterned and wet etched into the device layer of the SOI wafer. Signal line which bears the 260 nm trench is patterned and fabricated into the bottom SOI wafer. The line also serves as a DC electrode. After Si-Si direct fusion wafer bonding and subsequent high-temperate annealing to improve bonding strength, an inverted microstrip line is formed. The top DSP wafer is the ground plane for the inverted microstrip line and serves as the second DC electrode.

3.3.2.2 Device Fabrication

Figure 3.12 shows process flow of the RF microfluidic device fabrication. The devices are layout by use of software L-Edit Version 13 (Tanner EDA, CA) and transferred into 5" Soda Lime chrome mask (Nanofilm, Westlake Village, CA) by use of GCA/MANN 3600F Optical Pattern mask generator with a resolution of 2 µm. All following fabrication processes are conducted in a class 100 cleanroom at Cornell University and Georgia Institute of Technology. There are three parts in the device fabrication: bottom wafer fabrication, top wafer fabrication and wafer bonding between the top wafer and the bottom wafer. Figure 3.13 shows photos of fabricated RF microfluidic devices. Detailed fabrication procedures are described as follow.

Surface roughness and cleanness need special attentions during whole fabrication process, which are critical for high quality wafer bonding and subsequent water dielectric property study under high electric fields. In order to protect the surface from damage during the processes, plasma-enhanced chemical vapor deposition (PECVD) SiO_2 is grown to be mask layer if needed. The wafers are thoroughly cleaned after each fabrication process to ensure that there is a clean surface to start with for the next process.

3.3.2.2.1 Bottom Wafer Fabrication

A three-mask process is conducted to fabricate the bottom wafer.

Firstly, Alignment marks with depth of ~1 µm are pre-etched into the Si device layer for alignments of next two layers and wafer bonding alignment at the end. Standard photolithography and SF_6/O_2 RIE Si dry etch (200 mTorr, 200 W, 30 sccm SF_6 and 10 sccm O_2) is used to etch those marks.

Secondly, a shallow Si trench with depth of ~260 nm is fabricated into Si device layer. Standard photolithography is used to transfer trench patterns into SOI wafer. In order to obtain smooth trench surfaces, two commonly used processes, Si wet etch and Si dry etch, are conducted to make comparisons. CF_4 RIE Si dry etch (40 mTorr, 150 W, 30 sccm CF_4) and SF_6/O_2 RIE Si dry etch (200 mTorr, 200 W, 30 sccm SF_6 and 10 sccm O_2) have been tested to fabricate the trenches with PECVD SiO_2 as mask material, which give Si etch rate of ~46 nm/min and ~900 nm/min, respectively. A Si wet etch process developed in Ref [82] is tested to fabricate the Si trench as well. A commercially available developer MF-322 (Shipley Company) is used as etchant which contains 2.44% Tetramethylammonium Hydroxide (TMAH) with less than 1% surfactant. Buffered

Oxide Etchant (BOE) 30:1 is used to etch native SiO_2 to form mask. Then MF-322 is used to wet etch Si trench with Si etch rate of ~3.0 nm/min. Etched surfaces of obtained trenches are examined through Scan Electronic Microscopy (SEM) first. Figure 3.14 shows two SEM images on the etched Si trench surfaces fabricated through Si dry etch and wet etch processes. There are some craters clearly observed in the CF_4 dry etched trench surface due to ion bombing action during RIE dry etch process. However MF-322 Si wet etch process gives much smoother trench surface, which is almost as smooth as un-processed Si surface. The surface roughnesses of obtained trenches are measured using Atomic Force Microscopy (AFM). Figure 3.15 shows AFM 3-D images on the trench surfaces fabricated through MF-322 wet etch, CF_4 dry etch and SF_6/O_2 dry etch. Their measured surface roughnesses are 0.835 nm, 2.211 nm and 21.858 nm, respectively. It clearly shows that the MF-322 wet etch process provides the smoothest trench surface. The obtained 0.835 nm rms roughness is comparable to that of the un-processed DSP wafer surface. The slower Si etch rate, the smoother etched surface.

The surface smoothness is one of the most important factors in nanofluidics. It also has big impact on the initialization of water breakdown on the systems with small gaps between electrodes. Smooth electrode surface is critical in reducing field enhancement effects caused by possible sharp conducting spurs [61]. It may also help surface wetting, hence eliminating trapped air bubbles [63]. Thus the smooth surface is very important for the device to sustain high DC electric fields when DI water is under test. Therefore MF-322 Si wet etch process is a better candidate for shallow Si trench fabrication. The MF-322 Si wet etch rates are carefully calibrated for Si wafers with different doping types and doping levels. Figure 3.16 shows obtained Si trench depths for different MF-322 etching time for four different Si wafers. The etch rate is extremely slow for highly Boron-doped p-type Si wafer. Thus this process is not suitable for Si etch for p-type Si wafer with very low resistivity. For medium Boron-doped p-type Si wafer, its etch rate is close to the etch rate of medium Arsenic-doped n-type Si wafer. The highly Arsenic-doped n-type Si wafer has the highest etch rate, which is of our interests since the device layers of our SOI wafers are highly-doped n-type Si. The trench depth of up to 500 nm is achievable with the native SiO_2 as mask. The obtained Si etch rate is ~3 nm/min. Trench depth and its surface roughness are examined through AFM. Figure 3.17 shows AFM 3-D image of the obtained shallow 260 nm deep Si trench. The rms. surface roughness of the trench surface is 0.835 nm as shown in Figure 3.15 (a).

Thirdly, microstrip signal line and coplanar waveguide (CPW) contact pads are patterned and transferred to the SOI wafer using standard photolithography. They are fabricated through the SF_6/O_2 RIE Si dry etch until SiO_2 box layer (insulating layer) is reached. Figure 3.18 shows a microscopy image of fabricated patterns in the bottom SOI wafer. The center portion of the microstrip signal line bears the Si trench which is etched down by 260 nm.

3.3.2.2.2 Top Wafer Fabrication

The top DSP Si wafer acts as a ground plate of the Si microstrip line fabricated in the bottom wafer. No patterning is conducted on the top wafer for microstrip line formation. But in order for the access of the contact-pads (on bottom SOI wafer) during on-chip measurements, accurate wafer bonding alignment and process-control, a two-mask process is conducted to fabricate the top wafer.

Firstly, alignment marks and some process-control marks are etched down 1 μm deep into back side of the top wafer through standard photolithograph and SF_6/O_2 Si dry etch. Alignment marks are used for the second mask alignment, the wafer bonding alignment at the end as well.

Secondly, open windows are fabricated in the top wafer. After final wafer bonding step, the microstrip line is sandwiched in between the top wafer and the bottom wafer. In order to access the signal/ground pads which are on the bottom wafer during high frequency measurement, the top wafer needs to open some windows for probing access. Inlet and outlet for sample injection are needed as well. Deep Reactive Ion Etch (DRIE) Si etch (Bosch Process) is used to etch through the 350 μm thick Si top wafer. First, PECVD SiO_2 is grown on both sides of the wafer: 1 μm thick SiO_2 on the front side of the wafer acts as stop layer for DRIE Si etch, and 3 μm thick SiO_2 on back side of the wafer acts as mask layer for DRIE Si etch. Then the windows are patterned through standard photolithograph and SiO_2 mask is formed by CHF_3/O_2 SiO_2 dry etch on the back side of the wafer. Then wafer is DRIE etched through from the back side of the wafer using Bosch process and the etching is stopped at SiO_2 stop layer due to high etching selectivity between SiO_2 and Si (~200). Finally the SiO_2 on both sides of the wafer are released by SiO_2 wet etch using BOE 6:1. Till now, the open windows for probe access and inlet/outlet for sample injection are formed. They are clearly shown in Figure 3.13.

3.3.2.2.3 Wafer Bonding

Si-Si direct fusion wafer bonding technique is applied to integrate the top wafer and the bottom wafer together to seal microfluidic channels. Standard RCA 1 (NH_4OH: H_2O_2: H_2O = 1:1:4, 70 ℃) and RCA 2 (HCl: H_2O_2: H_2O = 1:1:4, 70 ℃) clean of 10 min each are used to clean both wafers. Then a 1 min HF dip (100:1) is followed to remove the native SiO_2 on both wafers right before wafer bonding since hydrophobic Si-Si fusion bonding is needed in order to have good electrical contact between the ground pads on the bottom wafer and the top ground wafer.

Wafers are aligned (Karl Suss MA6/BA6 Mask Aligner) and quickly transferred to wafer bonder (Suss MicroTec SB8e Wafer Bonder) for wafer pre-bonding. Wafers are pre-bonded for 60 min under 4400 N tool force and temperature of 400 ℃, then the temperature is cooling down to 100 ℃ with small tool force still applied. Pre-bonded wafer stack is immediately transferred to furnace for high temperature annealing. N_2 annealing (N_2 flow of 8L/min) under 1100 ℃ (ramp time of 10 ℃/min) is applied for 120 min in order to obtain strong bonding strength. Bonding interface is examined using SEM. Figure 3.19 shows SEM images on cross section of the Si-Si bonding interface. Seamless bonding interface indicates good bonding strength is achieved between the top wafer and the bottom wafer. The photo of the bonded wafer has shown in Figure 3.13 (a).

3.3.2.3 Experimental Setup

An HP8510C VNA is used to measure the effects of high DC electric fields on microwave dielectric properties of water through an on-chip transmission-line measurement method [83]. Two-port approach is more accurate than a one-port capacitance measurement method (i.e., impedance measurement) [84] since it minimizes uncertainties caused by large contact resistance between probe tips and silicon contact pads. Ground-signal-ground (GSG) probes are used to measure scattering parameters of the microstrip line with or without water injected into the microfluidic channels. At each end of the inverted microstrip line, there is a 400 µm long 50 Ω silicon CPW transition section for GSG probing. Reliable electrical contacts between GSG probe tips and the silicon CPW electrodes are obtained and verified through DC resistance measurements. A full two-port short-open-load-through (SOLT) calibration procedure is performed before microwave measurements. High frequency measurements are conducted from 1 GHz to 16 GHz at a power level of 10 dBm. Results are relevant to water saturation effects under nanosecond electrical pulses (e.g., in a compact pulsed power systems). DC voltages are applied between Si microstrip signal line (+V) and the Si ground plate (-V).

Large aspect ratio of the planar microfluidic channel (i.e., 75 µm vs. 260 nm) provides uniform electric fields across DI water that fills the channel since fringe fields are negligible. In addition, very smooth electrode surface with rms roughness of 0.835 nm is obtained. Both factors are very important for the devices to sustain high DC electric fields when DI water is under test. Furthermore, silicon surfaces form 1-2 nm native silicon dioxide, which has well defined (i.e., nearly constant) broadband dielectric properties that do not change under high electric fields (such as ~ 10 MV/cm in silicon field effect transistors). The thin layer of native oxide prevents DC current conduction between the two electrodes. Therefore, electrolysis of water, which occurs when the applied DC voltages are larger than ~ 1.2 V, is precluded. As a result, DC current induced water temperature change, which affects water dielectric properties significantly, is minimized.

3.3.3 Results and Discussions

Figure 3.20 (a) shows measured transmission coefficients, S_{21}, of the device before water is injected into its channel. Applied DC voltages are up to 35 V, which corresponds to a field intensity of ~ 1.34 MV/cm. Higher DC voltages are not used due to measurement instrument limitations. Reflection coefficient, S_{11}, is shown in Figure 3.20 (b). No visible changes of S_{11} and S_{21} are observed for different DC voltages. Relatively low S_{11} magnitude is obtained even though significant mismatch exists due to small microstrip line characteristic impedance. The small S_{11} is partly due to conductive loss of the silicon CPW transition sections, which effectively reduce the reflected signal level. When DC voltage polarities are reversed, no effects are observed as well. Neither is breakdown. These observations indicate that effects of thin silicon depletion layers are negligible, which is expected from extremely high doping levels. Figure 3.20 shows that the device is lossy as expected, yet, the signal level is adequate for line property characterization. Therefore, the device is well behaved for water property studies under GHz range.

Figure 3.21 shows measured S_{21} and S_{11} for various applied voltages after DI water with a resistivity of 18 MΩ·cm is drawn into the device channel via capillary force. No channel flushing is conducted right before water injection since our channels are free of particles and residues due to stringent wafer cleanness control during device fabrication. Compared with Figure 3.20, water induces higher loss and larger reflection (due to smaller microstrip line characteristic impedance), as expected. Figure 3.21 also shows that there is no visible change in S_{11} and S_{21} when the applied voltage is below 10 V, which corresponds to a field of ~294 kV/cm. When the applied voltage increases further, S_{21} increases. S_{11} does not change significantly except for 35 V DC voltages. A 1-2 nm thick native silicon dioxide with a relative dielectric constant (ε') of 4 is assumed on each of the two silicon electrode surfaces. Direct charge tunneling, instead of Ohmic conduction, is dominant conducting mechanism for these ultra thin native SiO_2 layers (1-2 nm) under high DC electric fields [85-87]. From Fig. 2 in Ref. 20 and Fig. 2 in Ref. 21, we estimate that effective resistivity of the native oxide films is 8 or more orders of magnitude lower than bulk SiO_2 resistivity (10^{14}-10^{16} $\Omega \cdot$cm) if a 4.5 V voltage drop is considered across a single oxide layer. The 4.5 V voltage drop corresponds to a capacitive voltage division if we assume the relative dielectric constant are 4 for SiO_2 and 80 for water. Therefore, a DC field of ~ 1.03 MV/cm is achieved in water with the applied 35 V DC voltage. The increase of S_{21} is anticipated since the dielectric saturation of water causes lower water permittivity under high electric fields, therefore, smaller dielectric loss and smaller resistive loss (due to larger line characteristic impedance). Correspondingly, S_{11} is reduced due to better match. Repeatable measurement results are obtained while the applied DC voltages are cycled up and down. No breakdown is observed in all measurements. Water breakdown strength of the device is improved by a few factors [59, 64], including atomically smooth (silicon) electrode surfaces (with a rms. surface roughness of 0.835 nm), small electrode area ($75\,\mu\text{m} \times 500\ \mu\text{m}$), and small electrode separation distance (260 nm). In addition, field enhancements at the edge of our channel are limited due to edge curvatures, which form from high-temperature annealing processes [88].

Unfortunately, it is difficult to obtain absolute water permittivity values directly from the measured S-parameters with conventional approaches [83]. Issues include strong silicon line resistive loss (which is also coupled with water dielectric properties that is to be determined), uncertainties between CPW and inverted microstrip line transitions, uncertainties of probe-tip contact (even though the contact is reliable), and a lack of reliable on-chip de-embedding structures. However, we can assume that the signal differences between different measurements (i.e., under different DC voltages) are caused by water property differences since silicon line resistive loss may be approximated as the same. Then, let $\Delta\alpha_{i+1} = \alpha_{i+1} - \alpha_i$ be the loss difference between two different measurements, the water permittivity, $\varepsilon_i = \varepsilon_i^{'} + j\varepsilon_i^{''}$, can be extracted through

$$\varepsilon_i^{'} = (\beta_i / \beta_0)^2 \times \varepsilon_0^{'} \tag{3.5}$$

$$\varepsilon_{i+2}^{''} = (1 + \Delta\alpha_{i+2} / \Delta\alpha_{i+1}) \times (\beta_{i+2} / \beta_{i+1}) \times \varepsilon_{i+1}^{''} - \varepsilon_i^{''} / (\varepsilon_i^{'})^{0.5} \tag{3.6}$$

where α_i and β_i are attenuation constant and phase constant, respectively, of the inverted microstrip line at different DC voltages V_i (i = 0, 1, 2, $\cdots$) with V_0 = 0 V, V_1 = 10 V, V_2 = 15 V, and so on. These constants are obtained from signal propagation constant, $\gamma_i = \alpha_i + j\beta_i$, which is directly extracted from measured S-parameters [89]. We further assume frequency dependence of water permittivity for V_0 = 0 V, ε_0, is governed by Debye equation[90]. Then obtained water permittivity under different electric fields is shown in Figure 3.22. It is shown that with 1 MV/cm electric field, ε' and ε'' are changed up to 70%

and 50%, respectively. The change ratio is much higher than value predicated by Booth model, which indicates that ε' at DC is changed by 50% under ~5 MV/cm electric field [72]. Further work is needed to understand the discrepancies. Nevertheless, we notice that high-frequency, not DC, dielectric properties are measured in this work. Furthermore, neither frequency dependence nor ε'' is included in Booth model.

Temperature change, which affects water dielectric properties significantly [90], is not monitored in this experiment. Microwave probing signals and possible DC currents through water (via tunneling through native oxide layers) could heat up the water under test. However, following observations indicate that the temperature change is not main reason for the observed permittivity change. First, the same microwave probing signal is applied to the measurements when there is no DC electric field. Thus the observed ε' and ε'' changes are not from microwave heating. Secondly, the observed finite, 100 MΩ level DC resistance between the two DC electrodes does not change much during the measurements, which indicates that the applied DC voltages do not induce obvious water temperature change [91]. Additionally, estimated pull-in displacement at center of the channel plates is less than 2 nm at 35 V [92]. Therefore, the displacement causes negligible transmission line property changes.

3.3.4 Conclusions

In conclusion, highly-doped silicon microstrip-line-based devices with 260 nm deep planar microfluidic channels are fabricated and used to investigate water dielectric saturation effects. Microwave scattering parameter measurements are conducted to study water dielectric properties from 1 GHz to 16 GHz under different uniform DC electric fields. When the applied DC field is increased to ~ 1 MV/cm, measured S_{21} is increased up to 18 dB, which indicates a large change of water dielectric properties. The extracted water permittivity values show that ε' and ε'' are changed up to 70% and 50%, respectively. Further work is needed to improve data extraction accuracy and to conduct a greater array of measurements in similar devices with different channel depth over a broader frequency range in order to better understand water dielectric saturation properties. The obtained devices can also be used to study high electric field effects on other dielectric fluids, such as glycerol [93].

ACKNOWLEDGMENT

The work is supported by Air Force Research Office under contract # FA 9550-06-1-0505. The fabrication is conducted at the Cornell NanoScale Science and Technology Facility (CNF) in Cornell University and the Microelectronics Research Center (MiRC) in Georgia Institute of Technology.

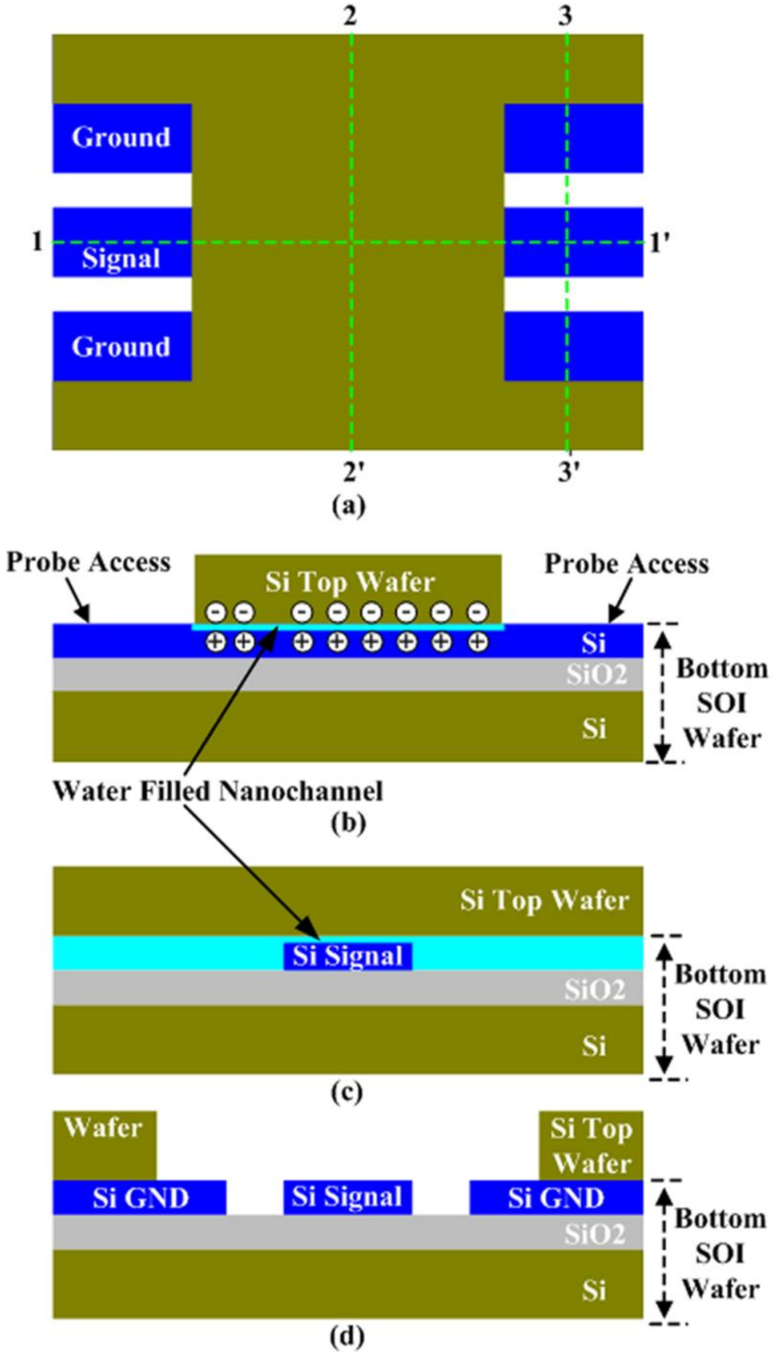

Figure 3.11: Schematic of RF microfluidic device. (a) Top view. (b) Cross section view of plate 1-1'. (c) Cross section view of plate 2-2'. (d) Cross section view of plate 3-3'.

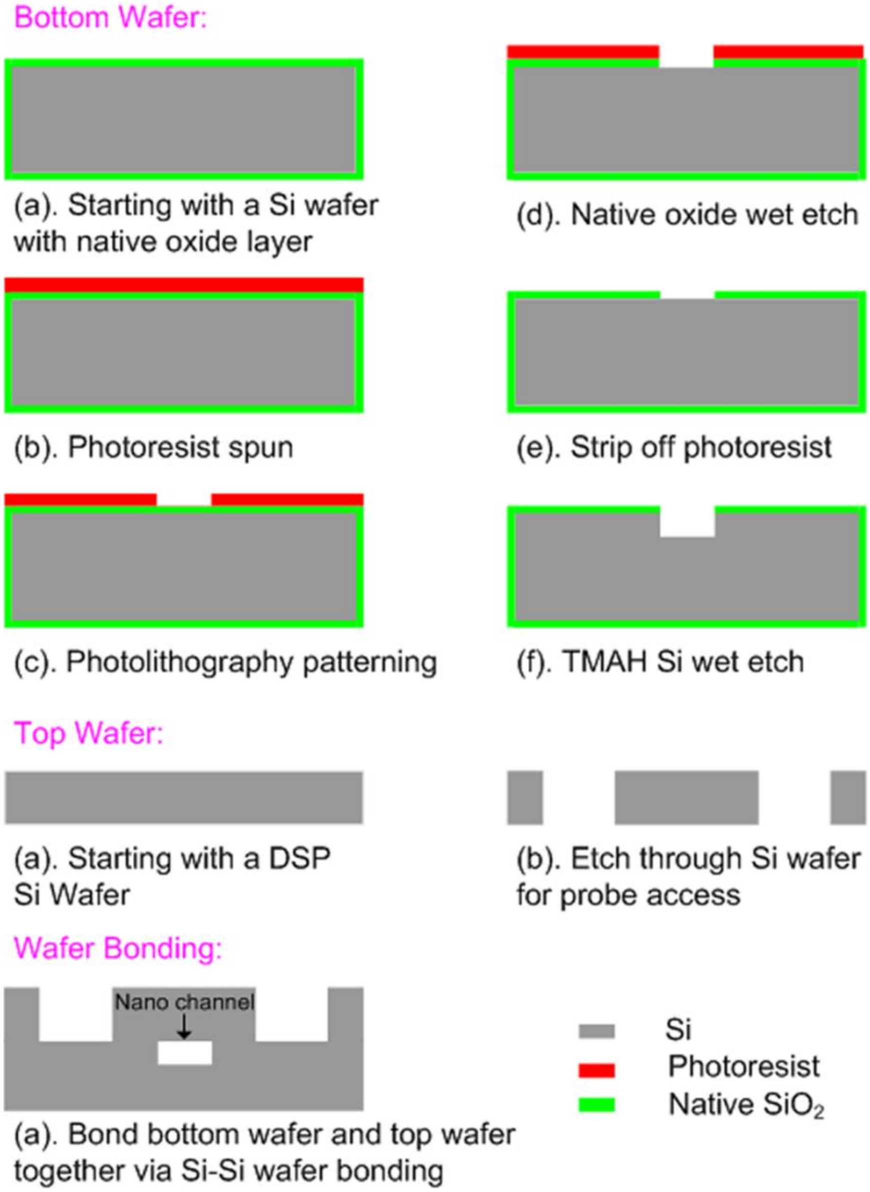

Figure 3.12: Process flow for RF microfluidic device fabrication.

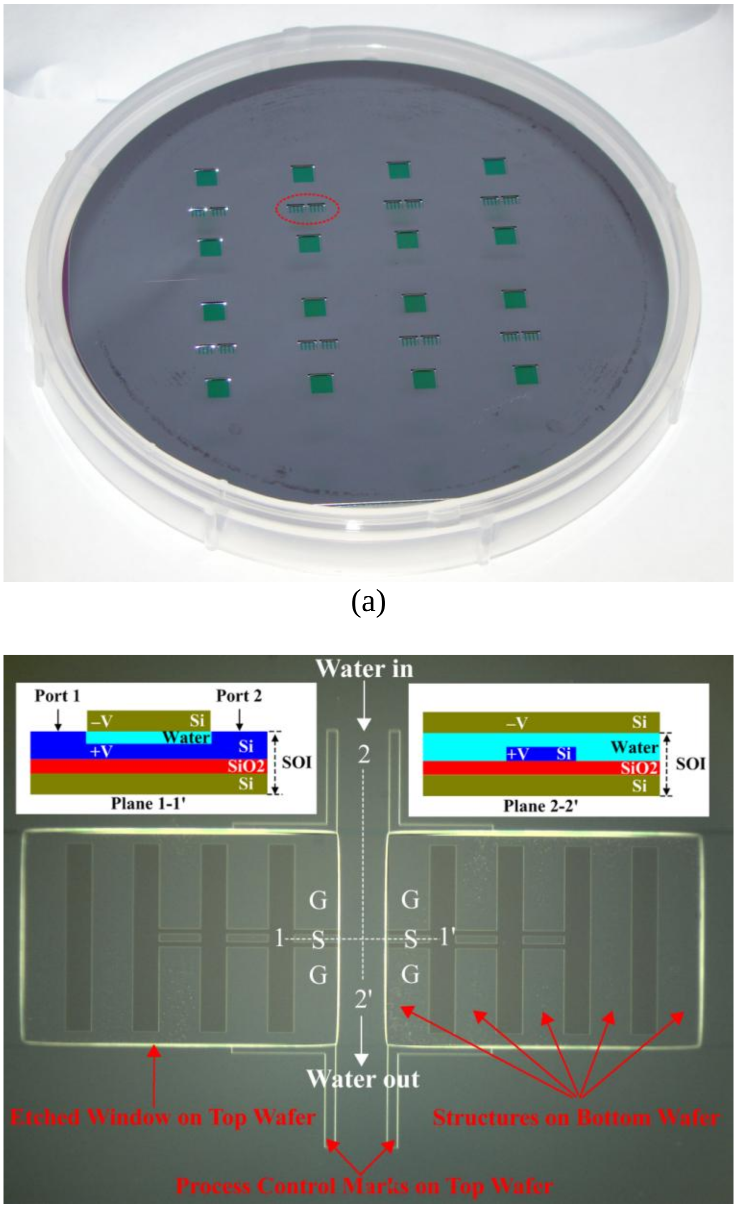

Figure 3.13: (a) Photo of fabricated RF microfluidic devices. There are eight devices on a wafer. (b) Zoom-in microscopy image on device area indicated with red-dashed circle in (a). Two insets show cross section views (not drawn for scale) of plane 1-1' and plane 2-2'. Two windows are opened in top Si wafer for probe access of GSG pads fabricated on bottom SOI wafer during microwave measurement.

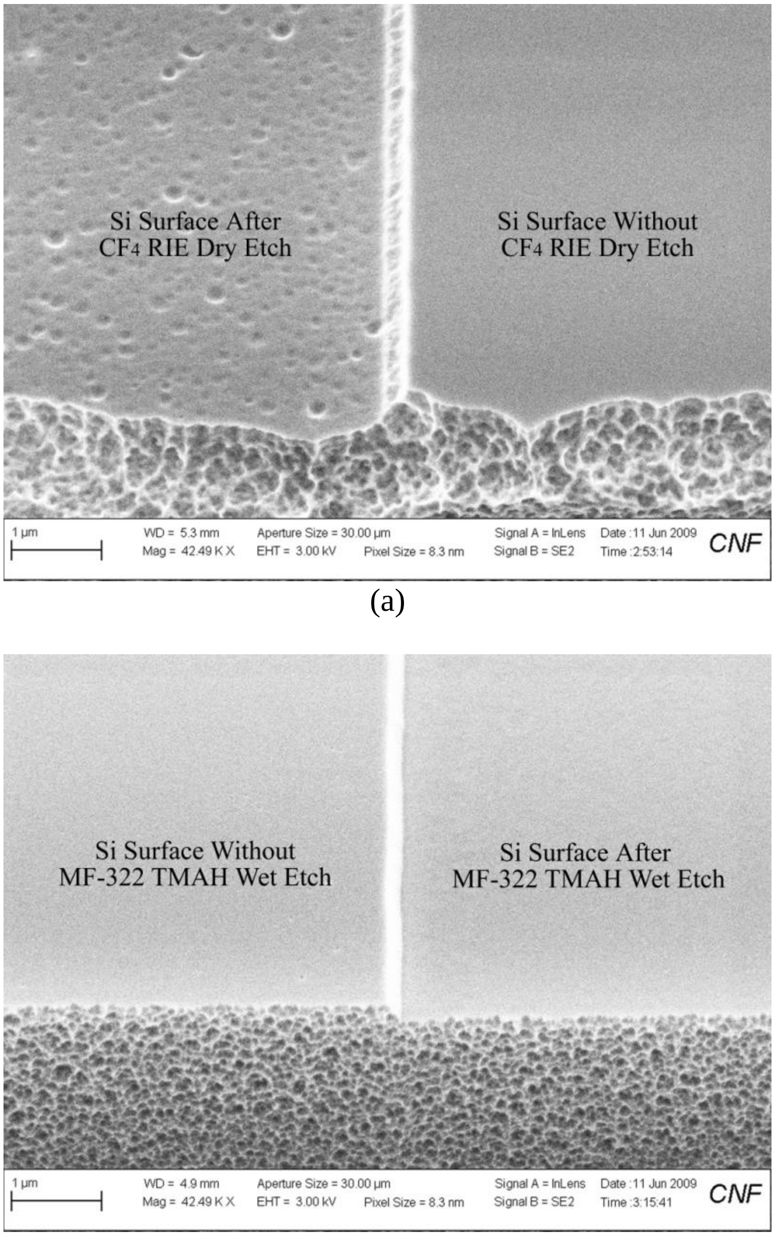

(a)

(b)

Figure 3.14: SEM images on Si trench surfaces fabricated through (a) CF_4 RIE dry etch and (b) MF-322 TMAH wet etch. It clearly shows that wet etch process provides much smoother surface.

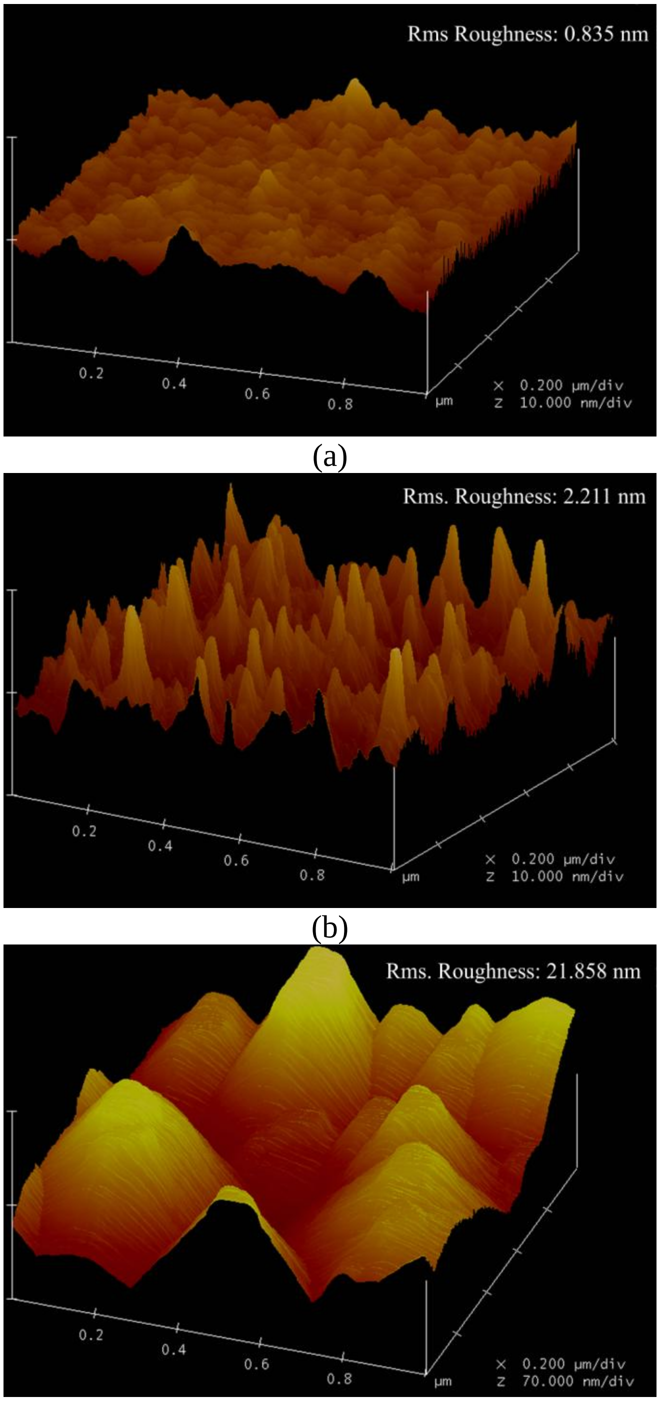

(a)

(b)

(c)

Figure 3.15: AFM 3-D images on roughness measurement for Si trench surfaces fabricated via (a) MF-322 wet etch, (b) CF_4 RIE dry etch and (c) SF_6/O_2 RIE dry etch.

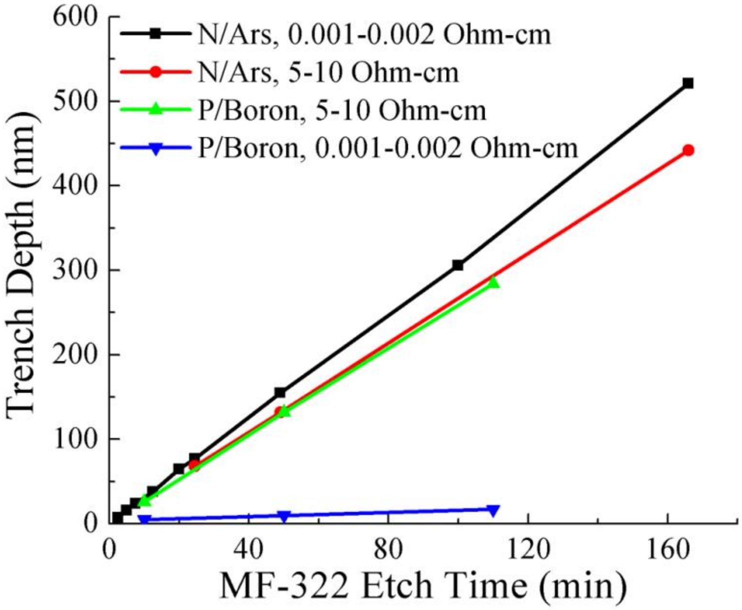

Figure 3.16: MF-322 Si wet etch rates for Si wafer with different doping type and resistivity. Obtained Si etch rate is ~3 nm/min for highly Arsenic-doped n-type Si wafer.

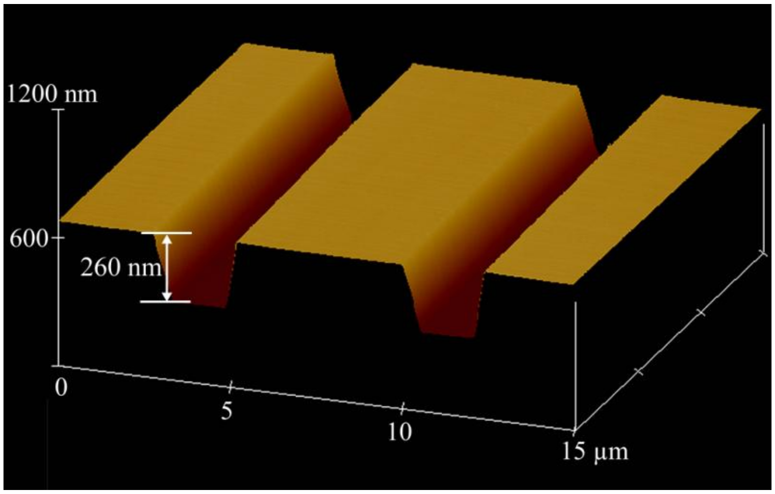

Figure 3.17: AFM 3-D image of obtained 260 nm deep Si trench.

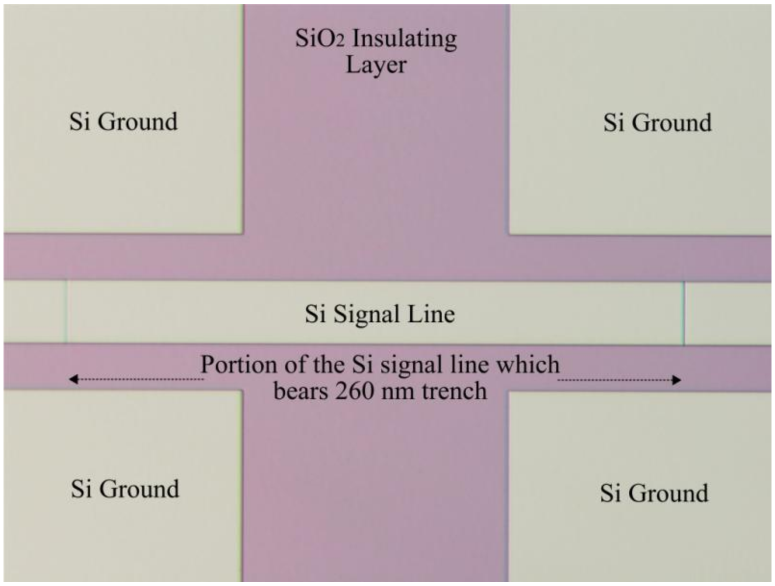

Figure 3.18: Microscopy image of patterns fabricated in bottom SOI wafer. Center portion of Si microstrip signal line is etched down by 260 nm.

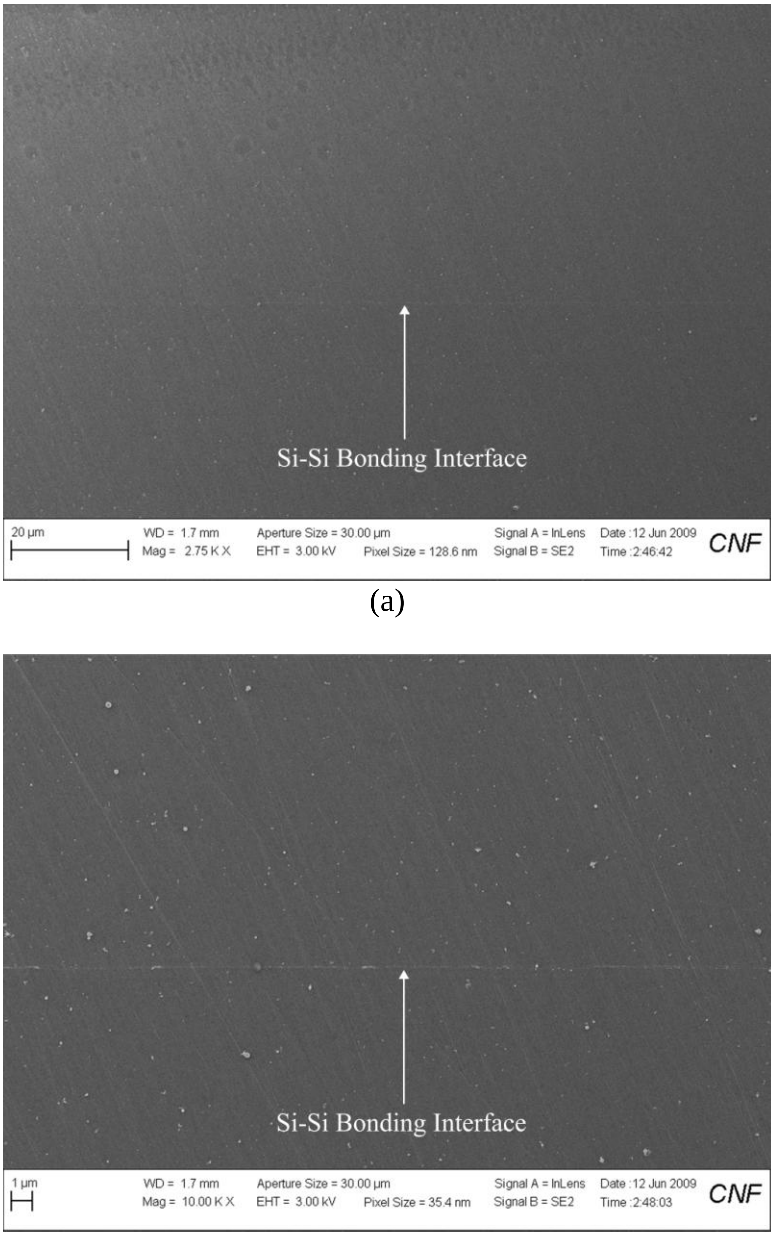

(a)

(b)

Figure 3.19: SEM images on cross section of bonding interface after Si-Si direct fusion wafer bonding.

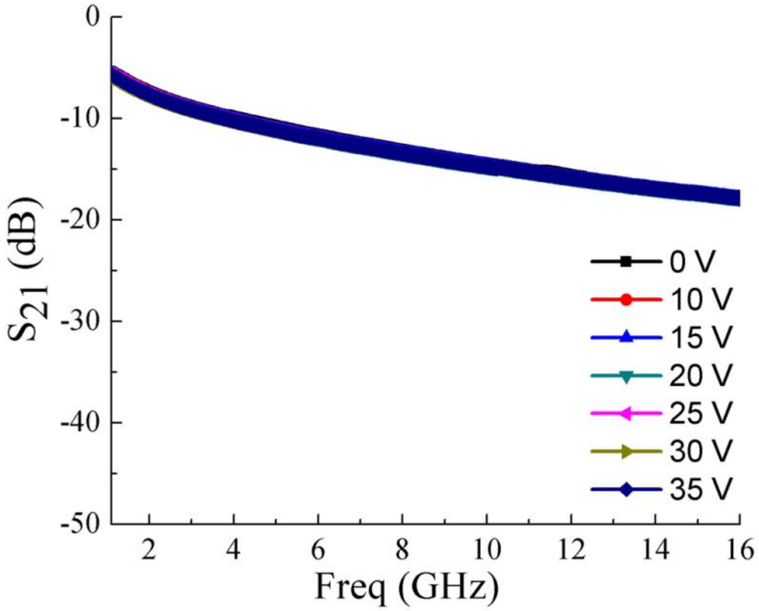

(a)

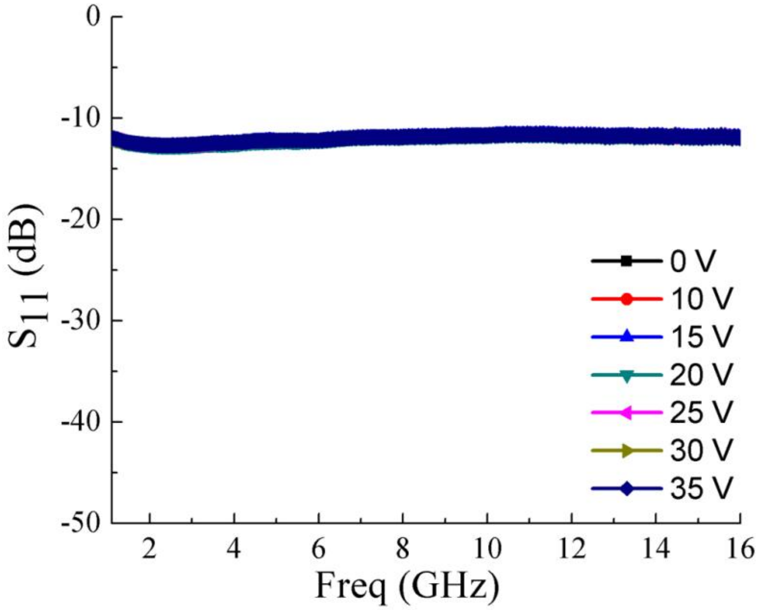

(b)

Figure 3.20: Measured transmission and reflection coefficients under various applied voltages when channel is filled with air. (a) S_{21}. (b) S_{11}.

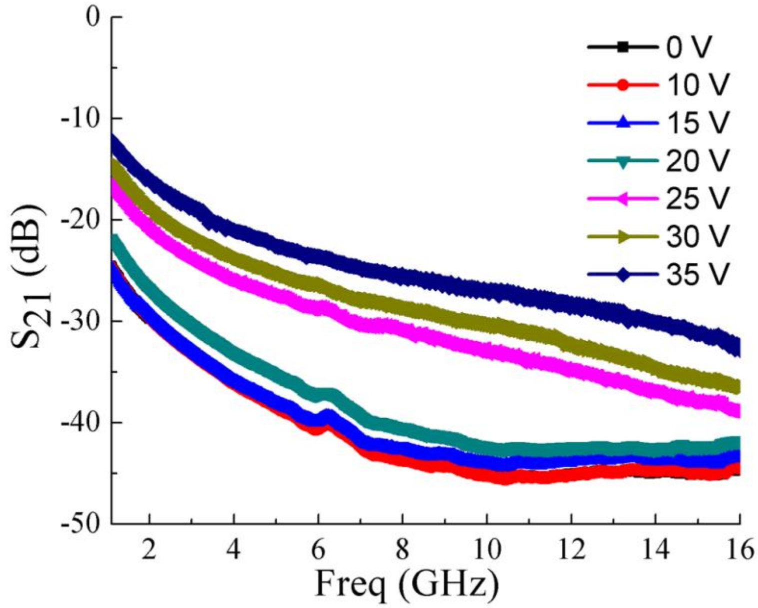

(a)

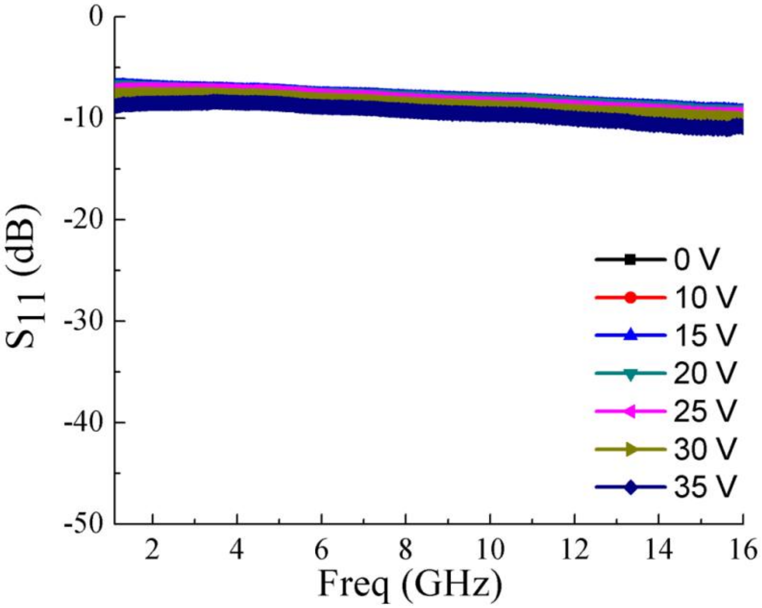

(b)

Figure 3.21: Measured transmission and reflection coefficients under various applied voltages when channel is filled with DI water. (a) S_{21}. (b) S_{11}.

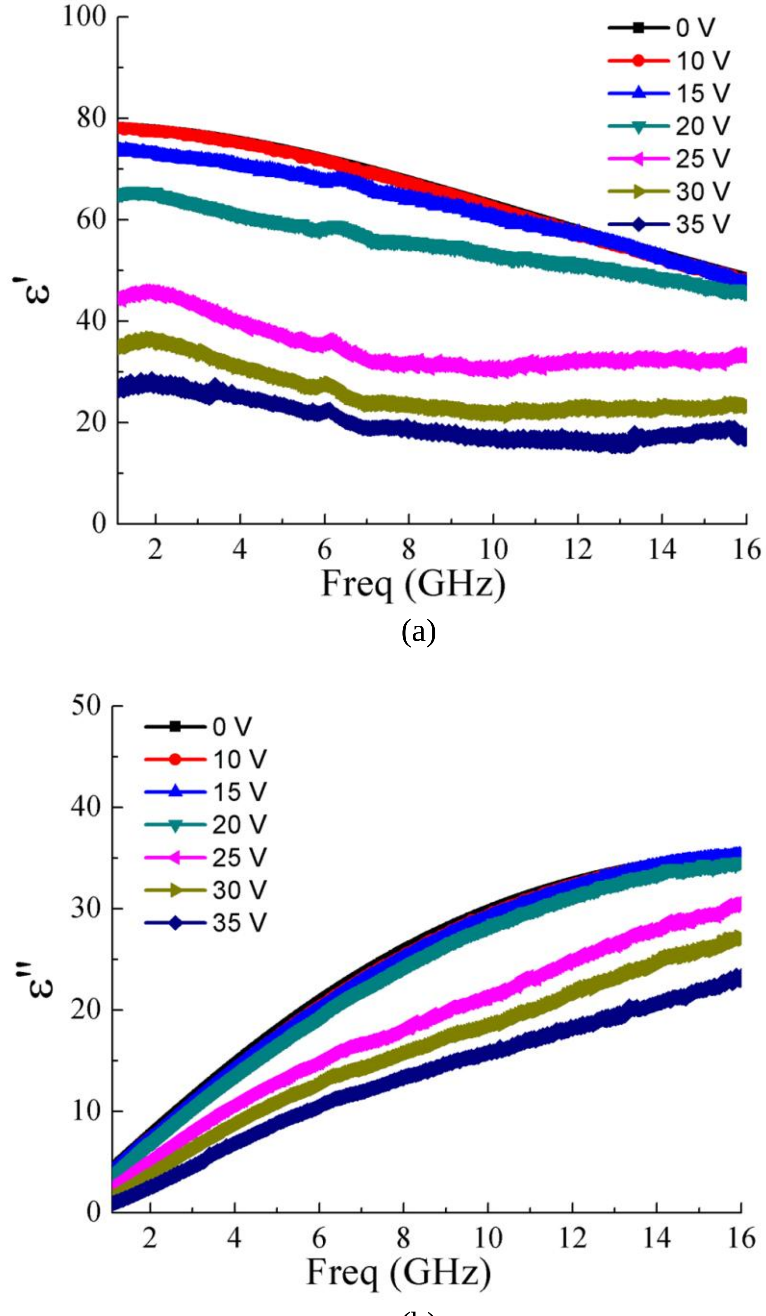

(a)

(b)

Figure 3.22: Extracted water permittivity ($\varepsilon = \varepsilon' + j\varepsilon''$) for different applied voltages. (a) ε'. (b) ε''.

CHAPTER FOUR

RADIO FREQUENCY NANOFLUIDIC DEVICES FOR DIELECTRIC PROPERTY CHARACTERIZATIONS

4.1 Fabrication of Sub-10 nm Planar Nanofluidic Channels through Native Oxide Etch and Anodic Wafer Bonding

4.1.1 Introduction

When critical dimension of a nanofluidic channel approaches 1 nm, new material properties and new applications emerge. For instance, confinement induces water molecular-structure change and permittivity decrease [94, 95]. Extremely small channel dimensions make it possible to fully stretch single DNA strands for their analysis and manipulations [96, 97]. Therefore, fabricating such nanochannel devices in a controllable fashion is currently one of critical issues in nanofluidics [98], nanobiotechnology, and fluidic electronics [99]. As a result, many efforts have been devoted to developing a reliable and reproducible fabrication strategy to build sub-10 nm nanofluidic channels. The efforts include a 9-nm wide self-enclosed, self-limited silicon-dioxide ($SiO_{2)}$ nanofluidic channel through nanolithography [96], a 7 nm slit-like non-planar nanofluidic channel through a nanoglassblowing method [100], a 10 nm enclosed nanofluidic channel through nanoimprint lithography [101], a 10 nm channel through polysisesquioxane sealing [102], and 5-6 nm planar nanofluidic channels through wafer fusion bonding [103, 104]. Among these nanofluidic channels, shallow planar ones, sometimes called nanoslits, are attractive because expensive nano-lithography processes are avoided [105]. To build such channels, wet etch is often used to form shallow trenches on a wafer, followed by wafer-bonding with a second flat wafer to form channels. The critical dimension of the obtained channels is the channel depth, which is usually the same as the trench depth [105]. As a result, sub-10 nm trench etch and wafer bonding are two key process steps.

Tetramethylammonium hydroxide (TMAH) silicon etch and dilute hydrofluoric (HF) SiO_2 etch are two main approaches studied for shallow trench formation. Due to start-up problems, TMAH etch is usually used for Si trenches that are 20 nm or deeper. On the other hand, SiO_2 trench depth is mainly determined by space layer (oxide) thickness [103] or HF etch time [104]. 5-6 nm thermal oxide trenches [103] are the shallowest reported so far despite the fact that 2-3 nm thick gate oxide are routinely obtained in silicon field effect transistor fabrication, for which stringent process control is required and expensive furnace growth process is involved. HF SiO_2 etch is hard to control if shallow trench depth needs to be precisely determined. Additionally, surface roughness increases during etch process [98]. Therefore, a simple approach that enables sub-10 nm trench formation is desired. Furthermore, the approach should not damage wafer properties, such as surface roughness, flatness, and induce stress since the damages will affect wafer bonding significantly.

Compared with Si/glass fusion bonding, anodic bonding is popular due to its high bonding quality (strength) and less stringent process requirement. However, channel collapse is a major challenge for sub-10 nm channel formation. The collapse happens when elastic recovery forces of substrates around the channel areas are weaker than van der Waals forces (surface energy). The electrostatic attraction force from an applied voltage will aggravate channel collapse problems by initiating surface contacts. Therefore, low voltage and low temperature (i.e., low surface energy) anodic bonding is desired. With the anodic bonding approach, a 20 nm deep channel is the shallowest channel reported so far [105]. Corresponding aspect ratio, 0.004, is also the smallest.

In this section, we report fabrication of sub-10 nm deep planar nanofluidic (silicon-glass) channels/slits with a simple process, which includes etching native oxide to form extremely shallow trenches and a low-temperature, low-voltage anodic wafer bonding process.

4.1.2 Fabrication of Nanofluidic Channels

Figure 4.1 illustrates layout considerations of the nanochannels. A total of 10 parallel nanochannels are included in each group. Channels are 15 mm long with different channel width varying from 2 μm to 50 μm. Inlet and outlet are included for fluidic filling test. All fabrications are conducted in a class 100 cleanroom.

Figure 4.2 shows a process flow of nanochannel fabrication. It includes two major parts: one is to develop a simple process to fabricate very shallow Si trenches with very smooth trench surfaces in a controllable manner; the other is to develop a proper wafer bonding process to seal the trenches to form nanochannels.

4.1.2.1 Shallow Silicon Trench Etch through Multiple-HF-Dip Process

The fabrication starts with a bare n-type silicon wafer with resistivity of 0.001-0.002 Ω·cm. Idea of proposed multiple-HF-dip process for sub-10 nm Si trench formation is to etch native oxide, which is 1-2 nm thick, with diluted 100:1 HF. Then let native oxide re-grow at the etched area under ambient conditions for a certain period of time, e.g., 1 day in this work, followed by another oxide HF etch step. Iterate above processes until desired trench depth is achieved. Since 44% of the native oxide layer thickness is from Si substrate, therefore, the obtained trench depth, H, is $H=0.44\times n\times T$, where n is number of HF dips and T is thickness of the native oxide which can be easily and accurately obtained in a temperature and humidity controlled environment [106], e.g., in a cleanroom. The process applies to any type of Si wafers with different doping levels.

The class 100 cleanroom environment has an average temperature of 22 ℃ and a average humidity of 44% RH. Photoresist S1818 with a thickness of ~1.8 µm is used to pattern the trenches through standard photolithography procedures. The photoresist serves as mask material during HF dip etch. At the end of trench etch, the photoresist mask is removed by soaking into heated solvent 1165 (~70 ℃). Wait time between successive HF dips is user defined and it can be reduced if throughput is a concern, e.g. 1-2 hours wait time would be sufficient to grow 0.6 nm thick oxide based on characteristics of native oxide growth in an ambient environment [106].

Figure 4.3 shows the obtained trench depths measured with Atomic Force Microscopy (AFM) for different number of HF dips. It shows that well controlled shallow Si trenches can be obtained at an etch rate of ~1 nm/HF-dip. Thus, a ~ 1 nm trench is readily obtained by one HF dip. Furthermore, good etch uniformity is achieved across the wafer since etch time is not critical due to extremely high HF selectivity between Si and SiO_2. The high selectivity implies very low Si etch rate even when defects are present in Si substrates [107]. Therefore, the multiple-HF-dip process is not susceptible to possible Si substrate defects. Similar etch rates are obtained for Si wafers with different type and resistivity. Figure 4.4 shows AFM 3-D images of Si trenches obtained through different number of HF dips and their section analysis.

Surface roughness of obtained trenches is measured through AFM. Figure 4.5 shows AFM rms. surface roughness analysis over a $1\ \mu m \times 1\ \mu m$ area of the etched surface. Very smooth etched surfaces are obtained with RMS roughness of 0.4-0.6 nm for all obtained trenches. The roughness is comparable to polished bare Si surface. Thus, the etched surface does not deteriorate after many HF dips, which also indicates that the etch process is insensitive to substrate defects. Therefore, the process preserves trench surface smoothness, which is critical for nanofluidics studies [98], especially for sub-10 nm channels. Furthermore, the surfaces that are protected by photoresist are intact, and the etch process is at room temperature and stress free, which do not cause wafer deformation. These conditions are important for wafer bonding later on.

For comparison purpose, TMAH-based Si wet etch process is also conducted to fabricate Si trenches. The MF-322 is applied as etchant as described in Section 3.3.2. The results on etched trench depths and trench surface roughness are summarized in Table 4.1. The trenches obtained through MF-322 wet etch has little bit worse surface roughness than the ones obtained through multiple-HF-dip process, but they are still comparable in general. Difficulty of using MF-322 etch process for very shallow Si etch is its start-up problem: its etch rate is not well predicable in beginning of the etch process. Therefore it is good for fabricating Si trench with depth at least > 20 nm, but not suitable for very shallow Si etch (1-20 nm). Unlike TMAH-based Si etch, start-up problem is eliminated if multiple-HF-dip process is used for shallow Si etch.

4.1.2.2 Low-Temperature and Low-Voltage Anodic Bonding

A 500 µm thick, 100 mm diameter Pyrex 7740 (borosilicate glass) wafer with 15 Å or less surface roughness, R_a, and better than 10 µm flatness is used as top wafer for channel formation. Inlet/outlet access holes are mechanically drilled through the glass wafer for liquid sample injection. Temperature and voltage of anodic bonding is very process specific because it is affected by electrical and mechanical properties of both Si and Pyrex wafers. Both wafers are thoroughly cleaned and their surfaces are treated to be hydrophilic prior to anodic wafer bonding, which is performed at a temperature of 225 °C and a voltage of -400 V. Tool force of 660 N is applied to counteract any wafer bowing and ensure the wafers are in uniform contact. The bonding process is terminated when 10% of initial current is reached. After bonding, no voids are observed. When insert a sharp blade at edges, the wafers are not separated and the edges are chipped, which indicates good bonding strength [108].

The low bonding temperature makes glass deformation unlikely to occur, and displacement resulted from electrostatic force during bonding is negligible since a thick glass wafer is used [109]. In addition, channel widths (< 20 µm) are relatively small compared with glass wafer diameter. As a result, possible channel height non-uniformity due to possible glass wafer bowing is negligible.

4.1.2.3 Si-Si Direct Fusion Wafer Bonding

In addition to anodic wafer bonding technique, Si-Si direct fusion wafer bonding technique is also applied to bond two wafers together on order to seal the nanofluidic channels. A DSP Si wafer with resistivity of 0.001-0.002 Ω·cm is used as the top wafer. Standard RCA 1 (NH_4OH: H_2O_2: H_2O = 1:1:4, 70 ℃) and RCA 2 (HCl: H_2O_2: H_2O = 1:1:4, 70 ℃) wafer cleaning of 10 min each are used to clean both wafers. Wafers are aligned and quickly transferred to wafer bonder for wafer pre-bonding. Wafer is pre-bonded for 60 min under 4400 N tool force and temperature of 400 ℃, then the temperature is cooling down to 100 ℃ with small tool force still applied. Pre-bonded wafer stack is immediately transferred to furnace for high temperature annealing. N_2 annealing (N_2 flow of 8L/min) under 1100 ℃ (ramp time of 10 ℃/min) is applied for 120 min in order to obtain strong bonding strength. Bonded wafer stacks pass the inserting blade tests, which indicate good bonding strength.

4.1.3 Results and Discussions

Nanochannel fabrication through bulk nanomachining and wafer bonding is subjected to an issue: channel collapse during wafer bonding. Gösele et al. have presented a criterion to predict channel collapse [110]. For substrates with same thickness *d*, if channel width *R* < 2*d*, which is relevant to our case, the channel between a wafer pair collapse if $h < 3.6 \times (R\gamma / E)^{1/2}$, where *h* is channel depth, *γ* is surface energy and *E* is Young's modulus. This criterion implies that the channel collapse intends to occur if depth to width aspect ratio is small, surface attraction between two substrates is large, or plastic deformation of substrates is easy to happen.

Anodic wafer bonding commonly uses high temperature and high voltage. Induced glass deformation and strong force caused by applied electrical field increase possibilities for channel collapse. In addition, strong capillary force in very shallow nanochannel is another force trying to bring top surface and bottom surface together. Mao et al. have reported that a 20 nm channel with aspect ratio of 0.004 was fabricated through normal anodic bonding condition (350 °C, -800 V, 2000 N tool force), and implied that decreasing the bonding temperature and the voltage might achieve nanochannels with lower aspect ratio but it was not tested yet [105].

Therefore nanochannels with different depths and widths are fabricated and low temperature (225 °C) and low voltage (-400 V) anodic bonding is used to investigate limit of our technique in the nanochannel fabrication. Table 4.2 summarizes the results of channel survival or collapse for different depths and widths by microscopy inspection.

It is difficult to observe liquid flowing through a sub-10 nm nanofluidic channel due to its low contrast [103]. Therefore, water filling test cannot be used to visually determine whether a sub-10 nm channel is collapsed or not. Instead, optical inspection [103, 105] is used to determine channel collapse or survival after wafer bonding. The deeper channel, the bigger contrast and easier inspection between the survived and the collapsed channels. A simple and effective optical inspection scheme is used here for examination according to the channel depth: For depth < 20 nm, the contrast between the survived and the collapsed channels is not very big, thus differential interference contrast (DIC) mode is preferred and then images are converted to grayscale with slight contrast adjustment; For depth > 20 nm, both bright field (BF) mode and DIC mode can give the easy inspection since the contrast between the survived and the collapsed channels are big enough.

Figure 4.6 (a) and (b) shows microscopy images under DIC mode for bonded 6 nm deep channels with a width of 3 µm and 4 µm. The images are converted to grayscale and the contrast is slightly adjusted to show difference. Even tone inside the 3 µm wide channels indicates that the channels are survived from the bonding. Uneven tone inside the 4 µm wide channels indicates the collapse of the channels. When the depth of the channels increases, the contrast between the collapsed and the survived channels increases. The observation method for channel collapse/survival is further applied to 12 nm and 15 nm deep channels. Figure 4.6 (c) clearly shows that the 12 nm deep channels with a width of 10 µm survived, the 15 µm ones mostly collapsed. Figure 4.6 (d) clearly shows that 15 nm deep channels with a width of 15 µm survived, the 20 µm ones partially collapsed and the 25 µm ones totally collapsed.

In addition, water filling (through capillary force) tests are conducted with the 15 nm deep and 15 µm wide channels to verify the optical inspection results. Deionized (DI) water is introduced into the inlet hole and flows through the 15 mm long nanochannels. Figure 4.7 shows a still microscopy image of the filling process under BF mode. The image is taken at a position which is close to the outlet side, and we observe that the 15 µm wide channels are fully filled with DI water eventually, but no water is observed in 20 µm or 25 µm wide channels. Air bubbles are observed during water movement due to very shallow channels [111]. Figure 4.8 shows a fluorescence image of 24 nm deep channels, which are filled with high concentrated FITC dye in buffer solution. High yield of survived channel is obtained. Most of the channels are survived except three indicated collapsed ones. The fluidic filling observations agree with the optical inspections.

Table 4.2 shows that minimum aspect ratio obtained from our technique is around 0.001-0.002, which are significantly lower than those channels that were previously reported with anodic wafer bonding techniques [105]. The applied voltage and temperature, which are the lowest reported so far for anodic wafer bonding, are important for achieving our nanochannels with low aspect ratios. For the last row in Table 4.2, higher temperature and higher voltage are used during its anodic bonding for 37 nm channels fabrication. Its maximum allowed channel width is 30 μm, which is even smaller than the maximum allowed width (40 μm) for 24 nm deep channels. This is another indication that low temperature and low voltage anodic bonding can help to push the limit of this technique to a lower value.

We have attempted, but failed, to obtain scanning electron microscopy (SEM) images of cross section view for Si-Pyrex bonded channels due to SEM resolution limitation and sample preparation difficulties (e.g., cross section polishing for SEM imaging, especially for cross sections formed with two different materials, such as Si and Pyrex). Charge accumulation on the non-conductive Pyrex (cross-section) further complicates our effort. Such difficulties are documented in literature [103]. However, we obtained SEM images of 10 nm, 20 nm and 30 nm planar channels formed through Si-Si fusion bonding. These channels are fabricated by use of the multiple-HF-dip trench formation techniques. Figure 4.9 demonstrates that the channels are uniform with their heights equals to the trench depths before wafer bonding, similar to the Si-Pyrex channels

[105]. Furthermore, possible wafer bowing effects on channel height and uniformity can be neglected since the channels are narrow. Wafer deformation during bonding (due to temperature and voltage pulling) can also be ignored. Therefore, the obtained Si-Pyrex channel height equals to the Si trench depth, and the control of trench depth transfers to the control of channel height.

Compared with other nanochannel fabrication approaches (e.g. those mentioned in Section 4.1.1), the above results and discussions show that our approach in this work is simple, easy to control and low-cost for sub-10 nm planar Si channel fabrications. Nevertheless, further work is needed to develop channels that approach 1 nm and techniques for their characterizations in addition to exploring nanochannel applications.

4.1.4 Conclusions

In conclusion, a simple, multiple-HF-dip process is developed and characterized to etch native SiO_2 to obtain shallow silicon trenches. The room-temperature SiO_2 grow-etch-grow process yields an etch rate of ~1 nm/HF-dip with atomically smooth trench surfaces with rms. roughness of 0.4-0.6 nm. The ~1 nm/HF-dip etch rate allows for precise and repeatable control of the trench depth. The well controlled etch process and the obtained smooth surface make this process a good candidate of fabricating planar Si nanofluidic channels that approach 1 nm. The trenches are sealed with Pyrex glass wafers through a low-temperature and low-voltage anodic bonding process. The obtained channel aspect ratios are as small as 0.001-0.002. The obtained smallest channel height is 6 nm. The whole process is straightforward, repeatable and low-cost, which makes it readily applicable for sub-10 nm deep planar Si nanofluidic channel applications.

ACKNOWLEDGMENT

This work is supported by AFOSR under Grant #FA9550-06-1-0505. The fabrication is conducted at the Cornell NanoScale Science & Technology Facility (CNF), Cornell University.

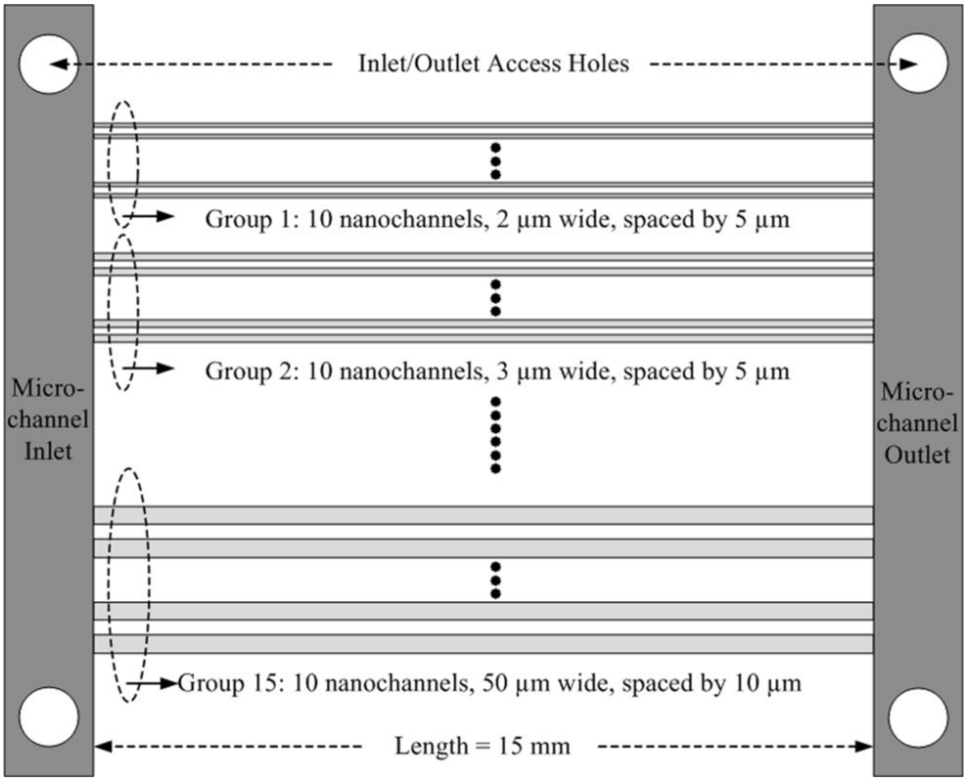

Figure 4.1: Layout considerations of test nanochannels.

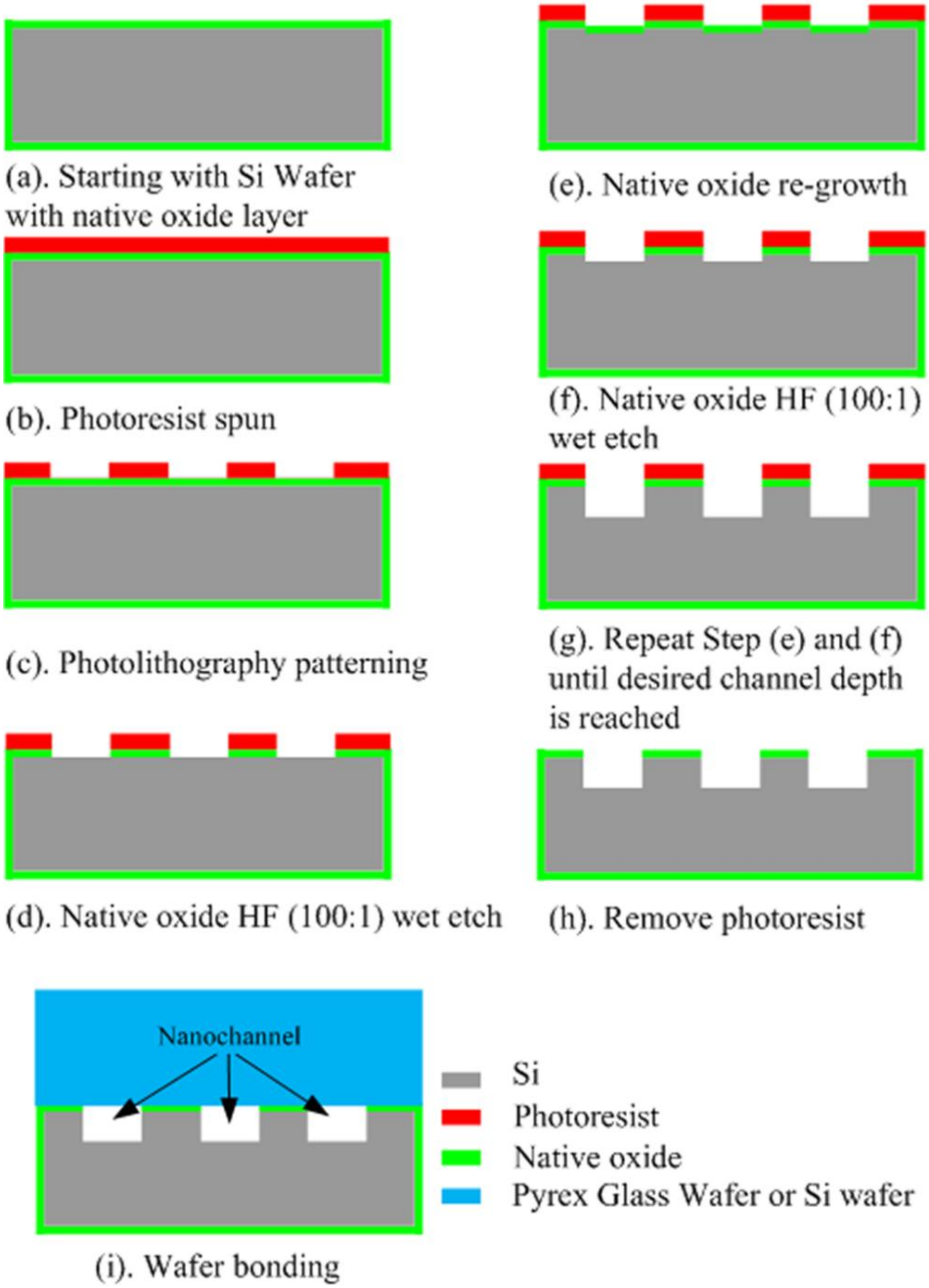

Figure 4.2: Process flow of nanochannel fabrication.

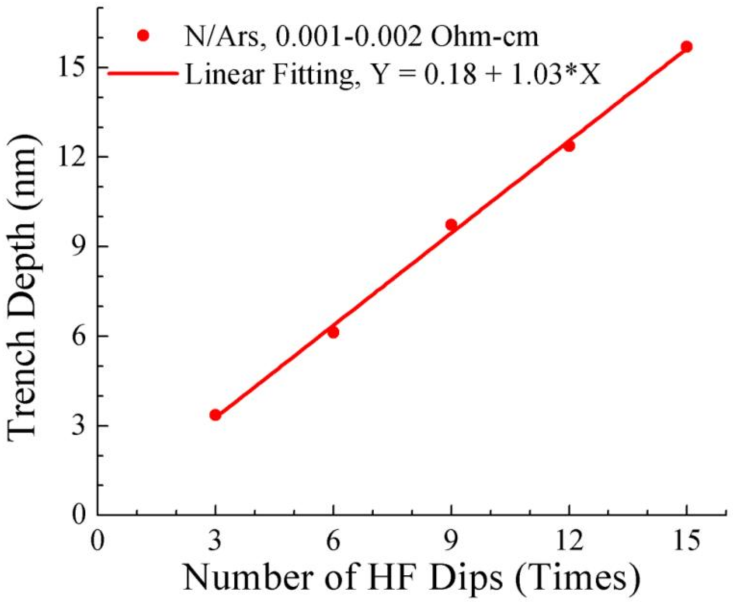

Figure 4.3: Trench depth versus number of HF dips. Very slow Si etch rate, ~1 nm/HF-Dip, is obtained for proposed multiple-HF-dip process.

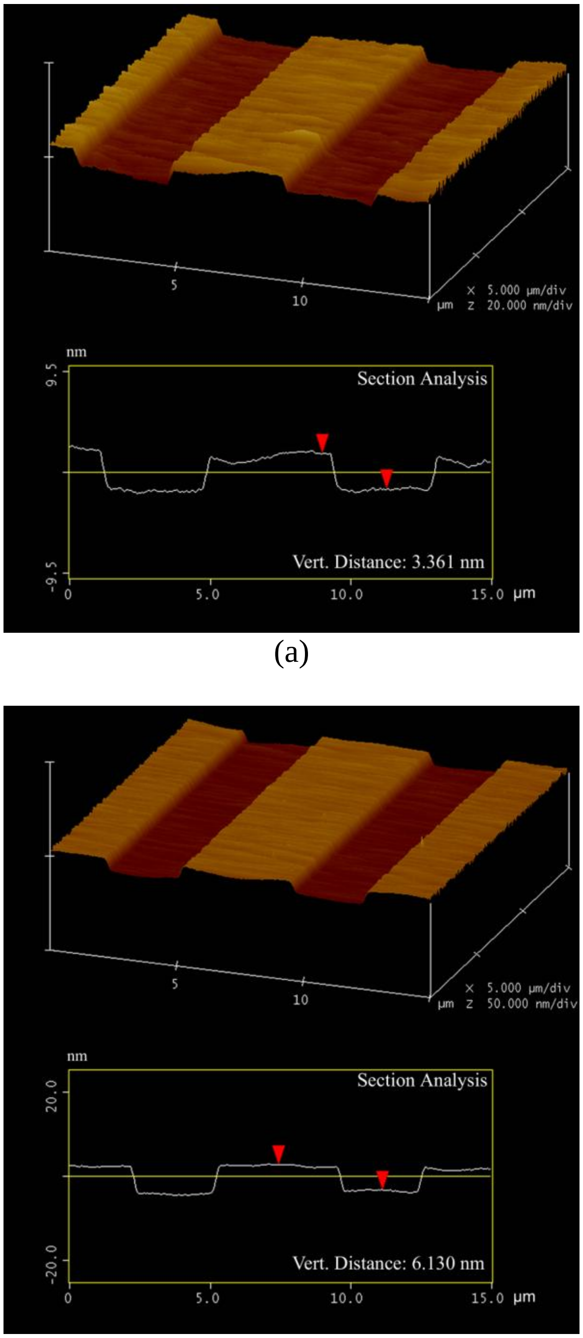

(a)

(b)

Figure 4.4: AFM 3-D images and its section analysis of shallow Si trenches obtained by use of (a) 3 times and (b) 6 times HF-dips.

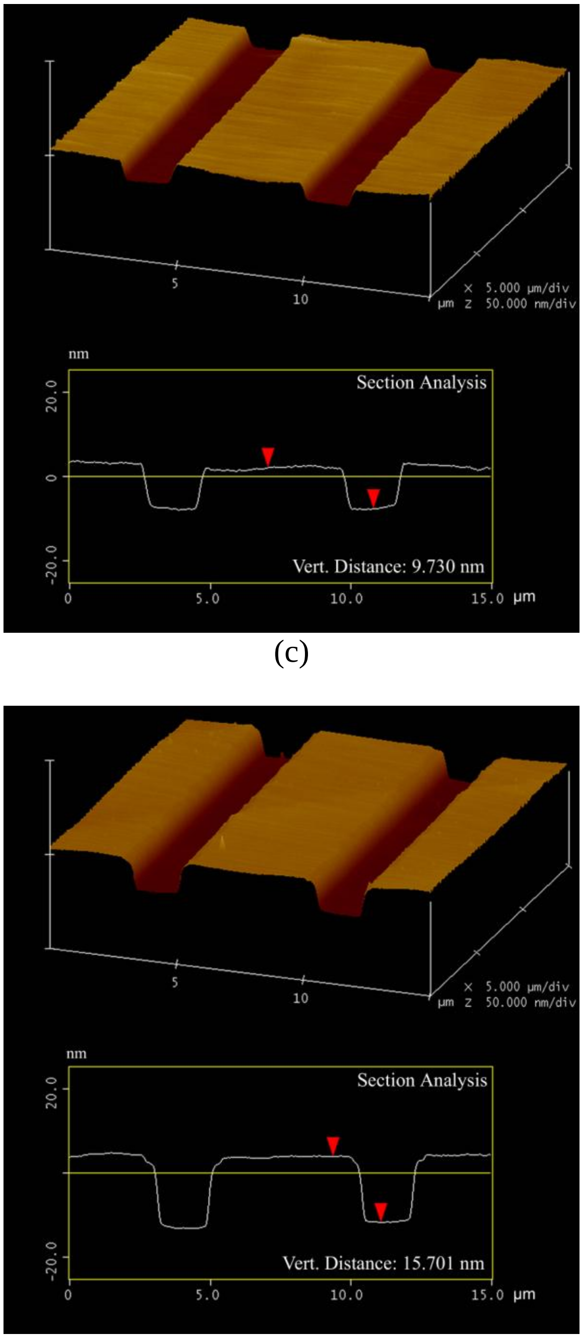

(c)

(d)

Figure 4.4 (Continued): AFM 3-D images and its section analysis of shallow Si trenches obtained by use of (c) 9 times and (d) 15 times HF-dips.

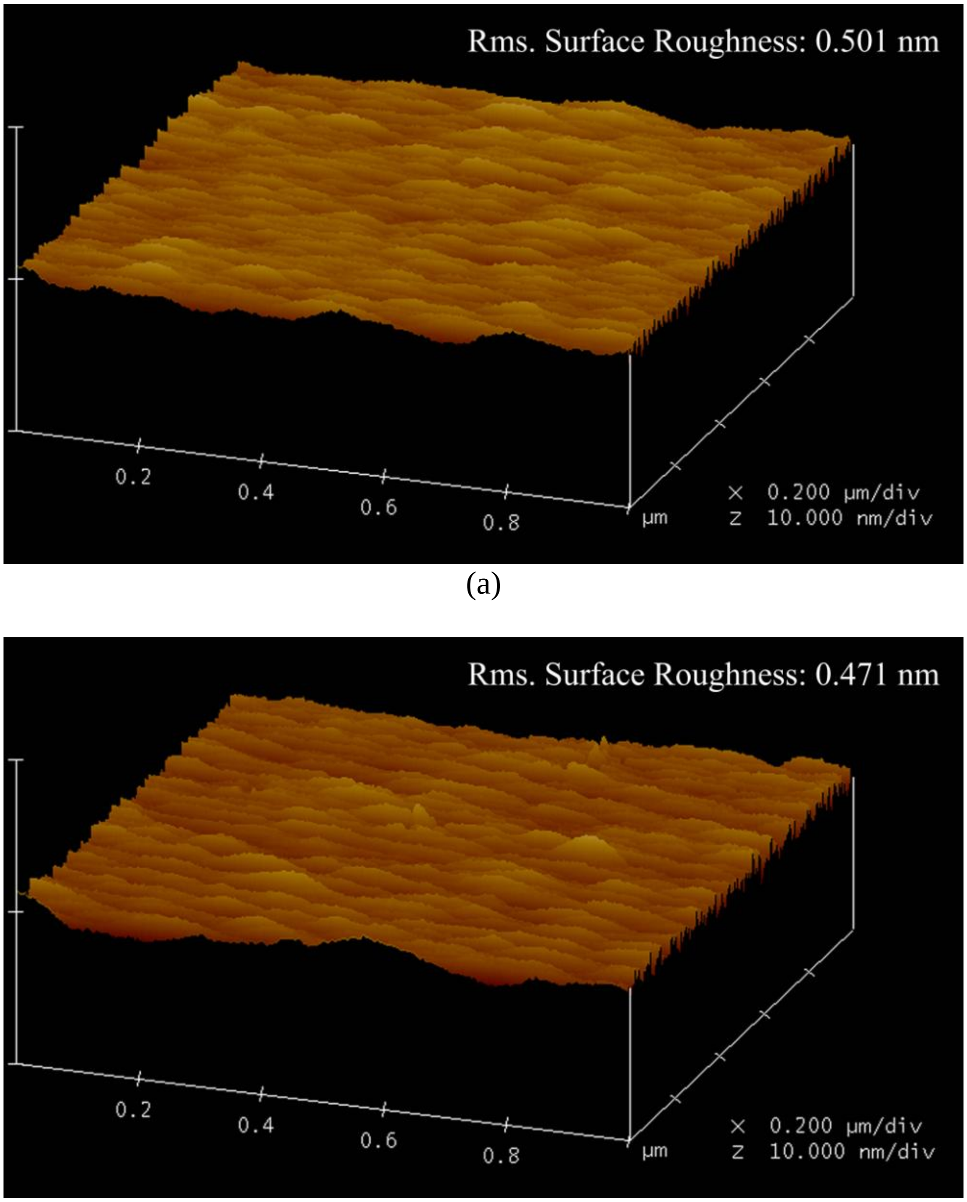

Figure 4.5: AFM surface roughness measurements and their 3-D images for trenches fabricated through (a) 3 times and (b) 6 times HF-dips.

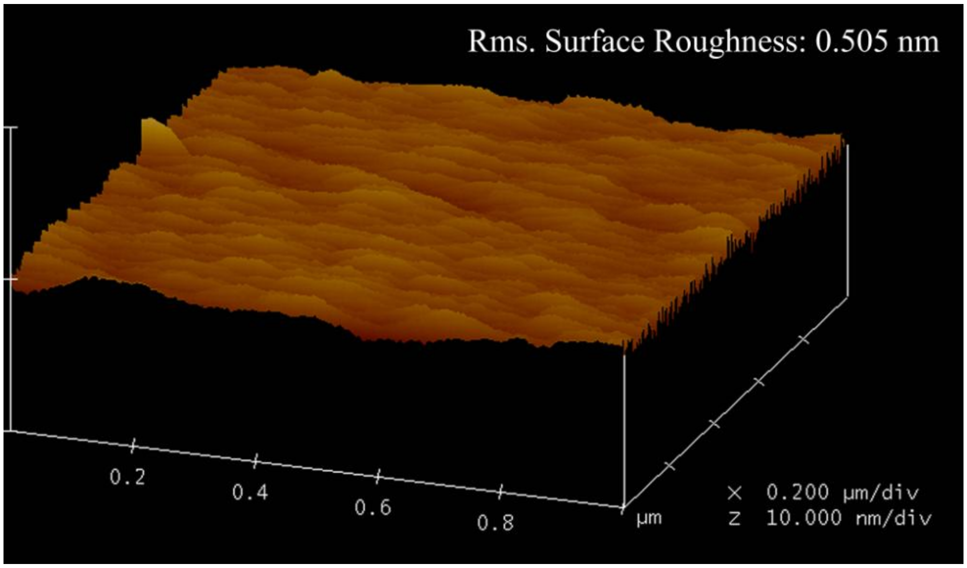

(c)

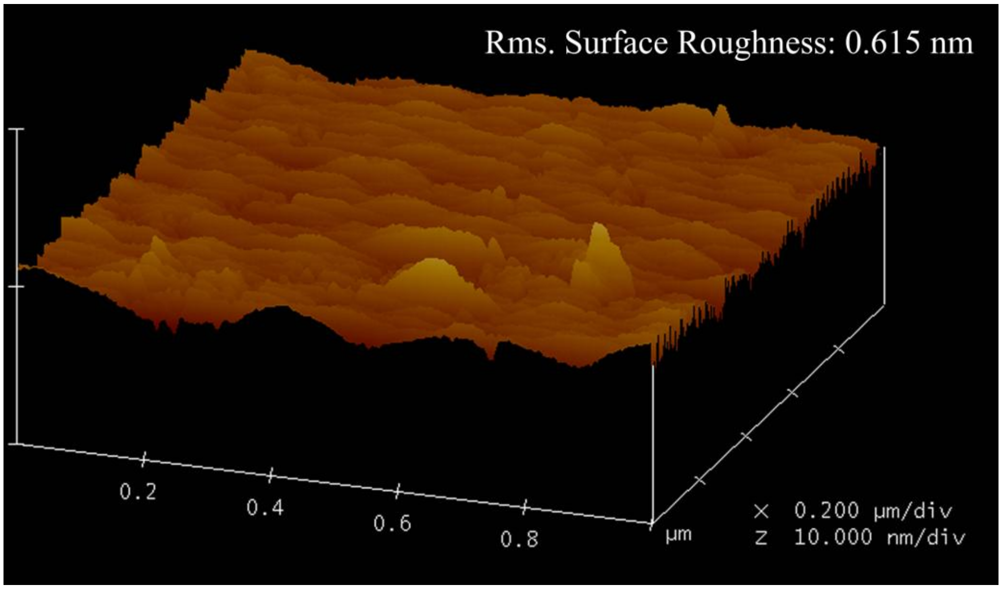

(d)

Figure 4.5 (Continued): AFM surface roughness measurements and their 3-D images for trenches fabricated through (a) 9 times and (b) 15 times HF-dips.

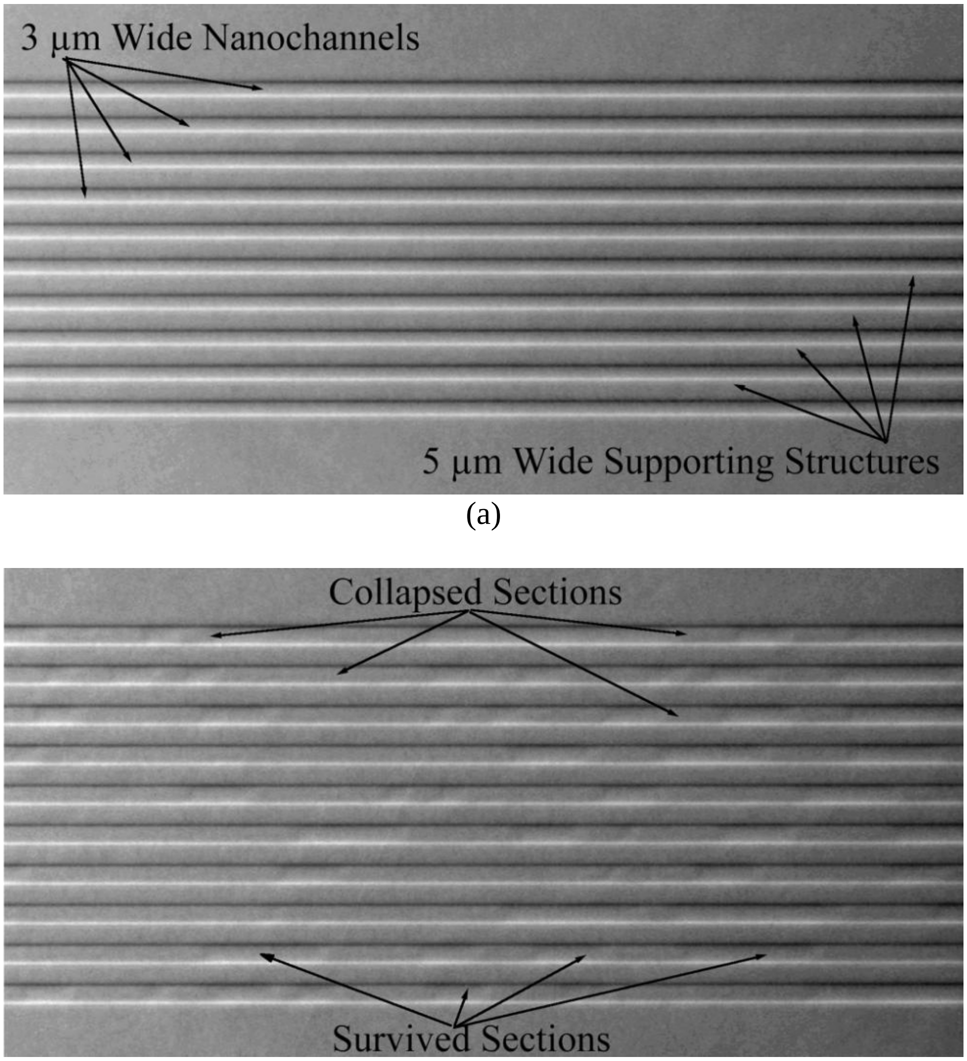

(a)

(b)

Figure 4.6: Grayscale microscopy images (DIC mode). (a) 6 nm deep, 3 µm wide channels with 5 µm spaces. (b) 6 nm deep, 4 µm wide channels with 5 µm spaces. Contrast is slightly adjusted.

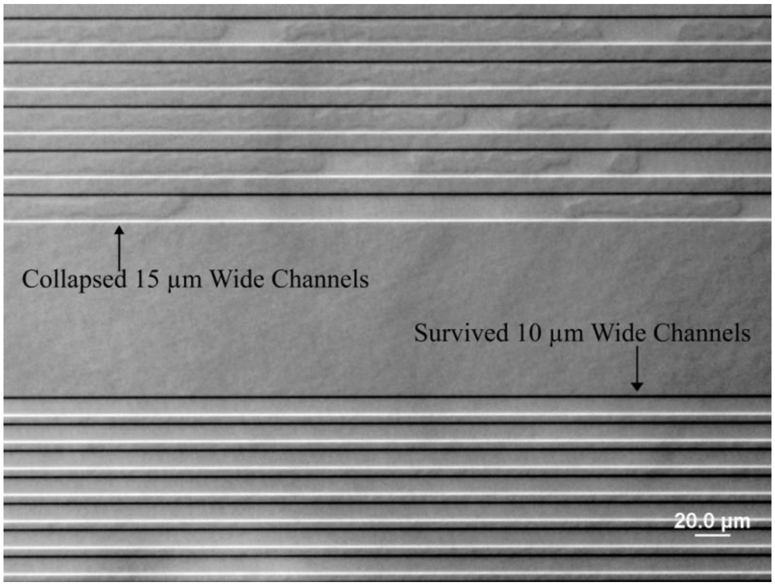

(c)

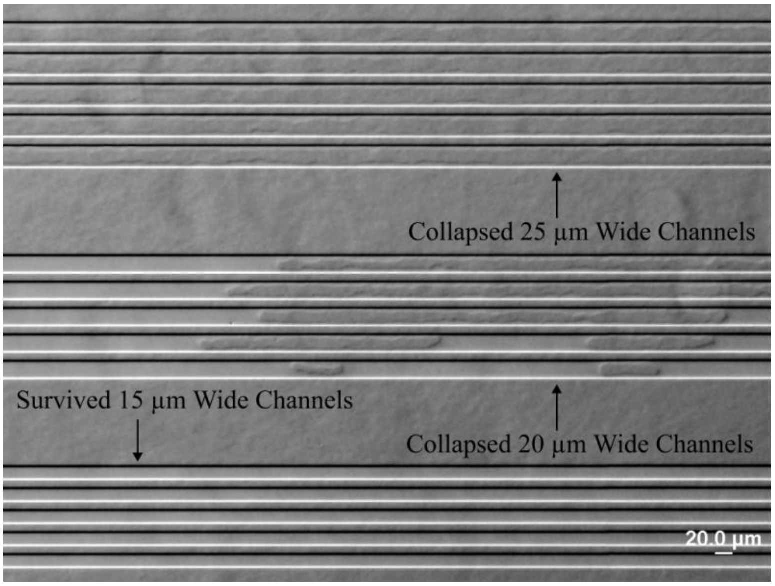

(d)

Figure 4.6 (Continued): Grayscale microscopy images (DIC mode). (c) 12 nm deep channels with channel widths of 10 µm and 15 µm, respectively. (d) 15 nm deep channels with channel widths of 15 µm, 20 µm and 25 µm, respectively. Contrast is slightly adjusted.

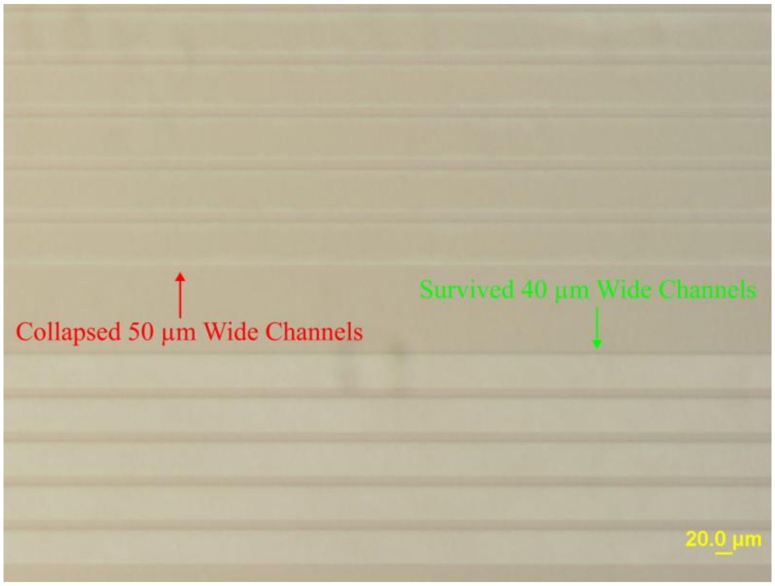

(e)

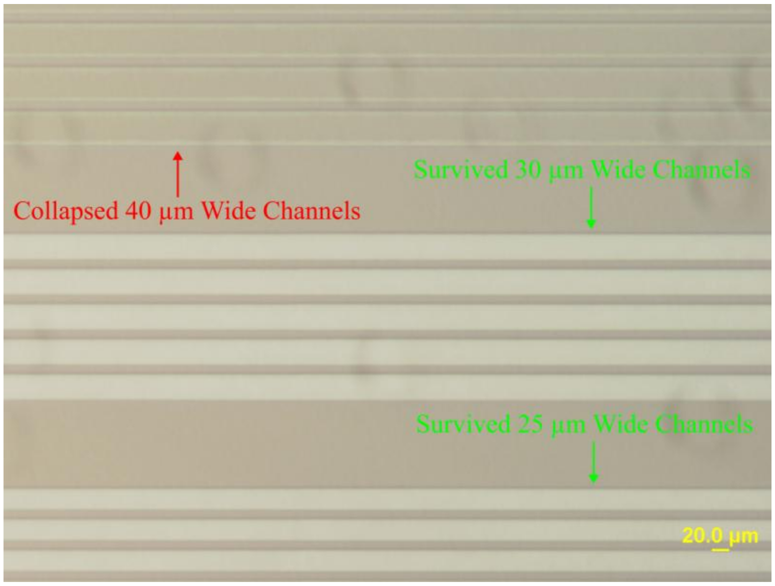

(f)

Figure 4.6 (Continued): Microscopy images (BF mode). (e) 24 nm deep channels with channel widths of 40 µm and 50 µm, respectively. (f) 37 nm deep channels with channel widths of 25 µm, 30 µm and 40 µm, respectively.

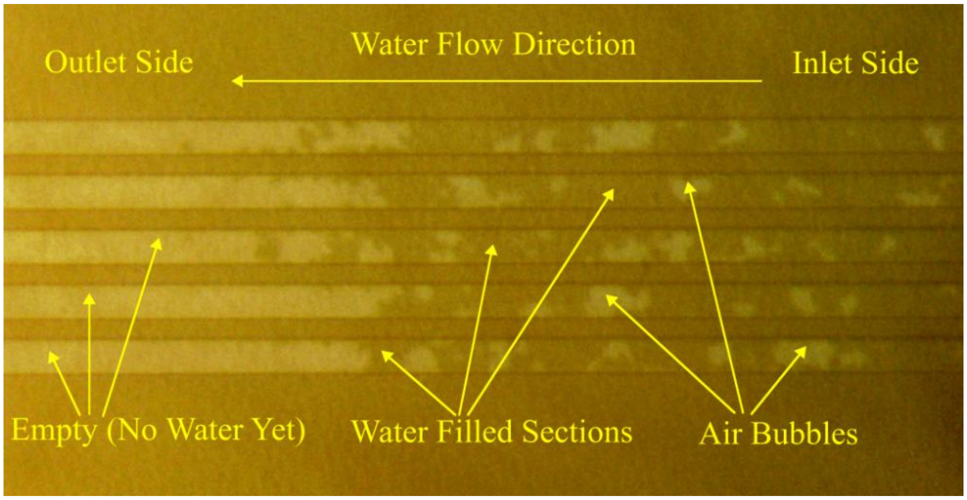

Figure 4.7: Still microscopy image (BF mode) of DI water flowing through 15 nm deep, 15 µm wide and 15 mm long channels. Contrast is slightly adjusted.

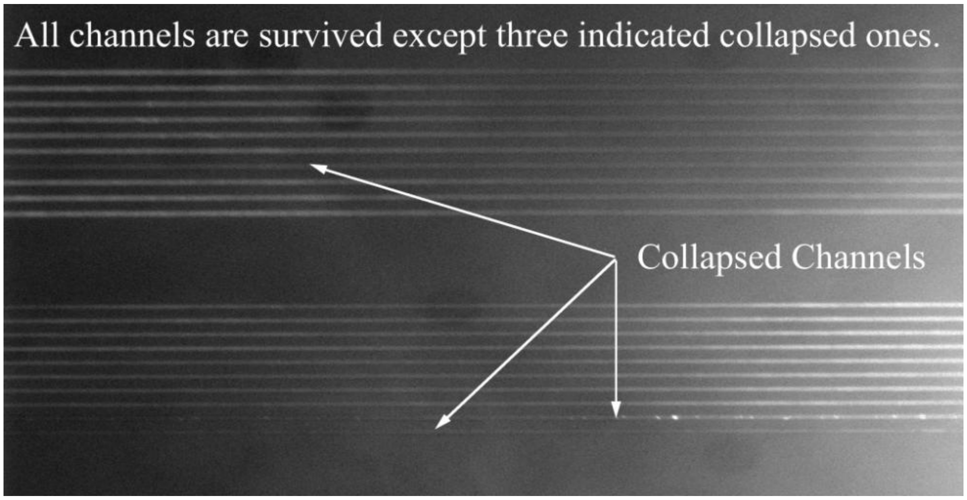

Figure 4.8: Fluorescence image of 24 nm deep channels which are filled with high concentrated FITC dye in buffer solution. Two groups of channels are shown here. Each group contains 10 nanochannels with same width (3 µm or 4 µm) and spaced by 5 µm.

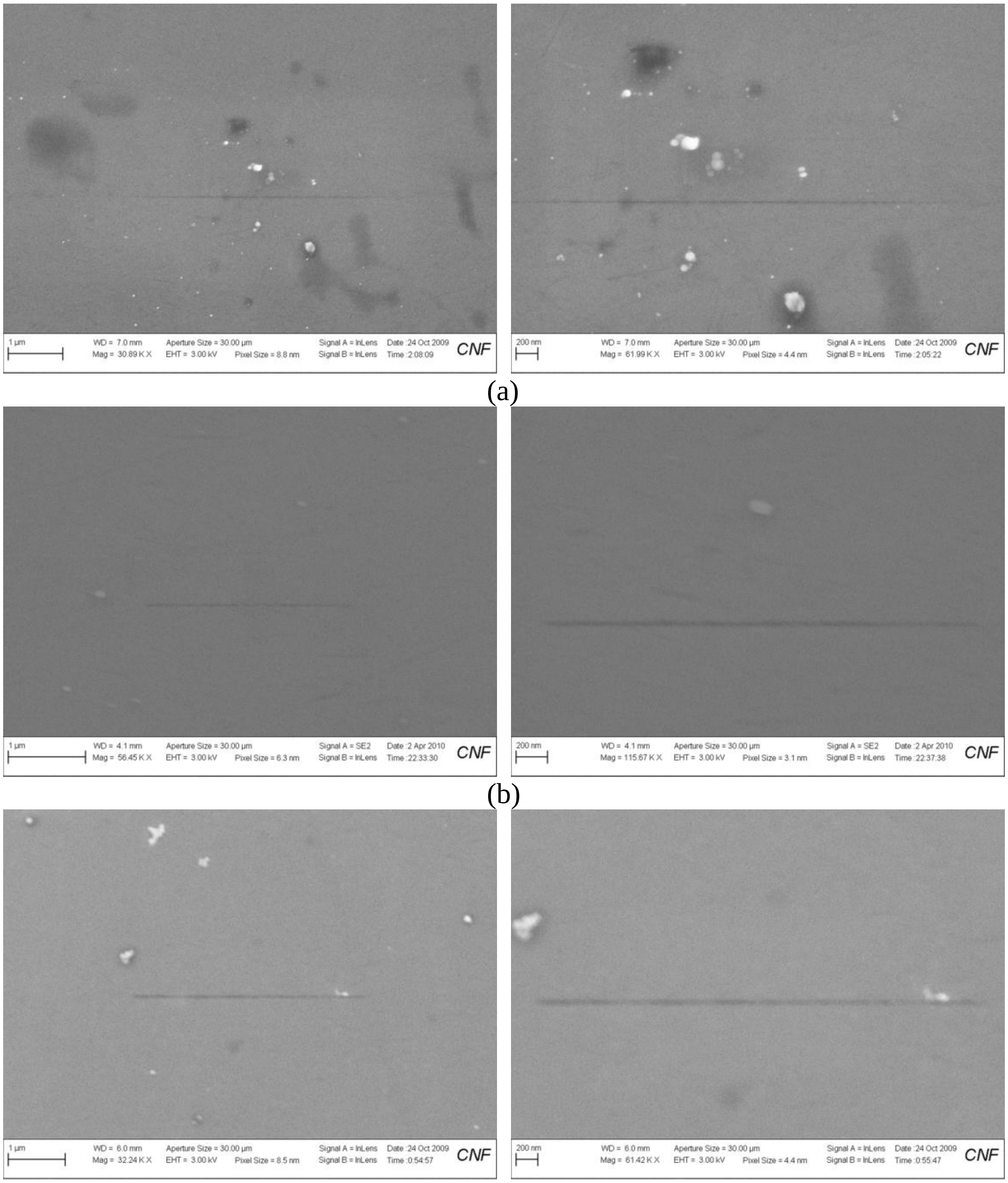

(a)

(b)

(c)

Figure 4.9: SEM images of cross sections of (a) 10 nm (b) 20 nm (c) 30 nm deep nanochannels fabricated via Si-Si fusion wafer bonding.

Table 4.1: AFM measured results of etched depths and surface rms. roughness for multiple-HF-dip and MF-322 Si etch processes.

Multiple-HF-Dip Si Etch Process			MF-322 Si Etch Process		
Number of HF Dips	Depth (nm)	Surface rms. Roughness (nm)	Etch Time (min)	Depth (nm)	Surface rms. Roughness (nm)
3 Times	3.3	0.501	5.0	16.0	0.679
6 Times	6.1	0.471	7.5	24.3	0.965
9 Times	9.7	0.505	12.5	37.9	1.091
12 Times	12.3	0.544	30.0	93.4	0.559
15 Times	15.7	0.615	100.0	306.3	0.835

Table 4.2: Optical inspection results on channel survival (√) or collapse (×) after anodic wafer bonding (225 ℃, -400 V, 660 N tool force)

Channel Depth (nm)	Channel Width (µm)															Minimum Aspect Ratio (Depth/Width)
	2	3	4	5	6	7	8	9	10	15	20	25	30	40	50	
6	√	√	×	×	×	×	×	×	×	×	×	×	×	×	×	0.0020
9	√	√	√	×	×	×	×	×	×	×	×	×	×	×	×	0.0022
12	√	√	√	√	√	√	√	√	√	×	×	×	×	×	×	0.0012
15	√	√	√	√	√	√	√	√	√	√	×	×	×	×	×	0.0010
24	√	√	√	√	√	√	√	√	√	√	√	√	√	√	×	0.0006
37[a]	√	√	√	√	√	√	√	√	√	√	√	√	√	×	×	0.0012

Note: [a] Anodic bonding parameters: 300 ℃, -800 V, 660 N tool force.

4.2 Design of Broadband Dielectric Spectrometer with Sub-10 nm Nanofluidic Channels and its Microwave Characterizations

4.2.1 Introduction

The dynamics of liquids, particular liquid water, in restricted environments comes under intensive investigation because it is recognized that the role of water in chemical and biological systems is often played by a limited number of water molecules in a strongly restricted molecular environment [112, 113], from a few angstroms to ~ 10 nm. Water in such a restricted environment is often called confined water as opposed to bulk water. Confined water and bulk water are expected to have different properties. Intensive molecular dynamics simulations have been conducted to investigate the water electrostatic, dielectric and dynamical properties under confined nanoscale spaces, such as single-walled Carbon nanotube [114], graphite channels [115], quasi-two-dimensional hydrophobic nanopore slit [116], nanodimensional spherical cavity [117], two parallel rough walls which are realized by frozen amorphous configurations of the same liquid [118], etc.. Due to confinement effect, strong directional dependence of the dynamics and dielectric properties is observed. A nearly 50 % decrease of the dielectric constant is observed when water is confined in a nanocavity of about 12 Å in diameter [117].

A few measurement methods have been developed and used for the study of confined liquid dynamics. A dielectric property measurement, also called dielectric spectroscopy, is one of them. In comparison with other methods, dielectric spectroscopy has its unique advantages, such as broadband measurement capability, label-free interactions with molecules in addition to non-contact sensing. Obtained dielectric permittivity of liquid provides information of dipolar relaxation dynamics. This method has been applied to study the dielectric property of liquid crystals and strong confinement effects are observed [119, 120]. The first application of this method for confined water dynamics research was recently published [121]. A few available dielectric spectroscopy data include dielectric property study of water confined in nanopores of nanostructured silica materials (e.g., MCM-41) [122-124]or silica gels [125], water droplet confined by ionic surfactants [126] or water molecules enclosed by acetone molecules [127], etc.. There is also a relatively large uncertainty of the confined water dimensions due to a wide distribution of the pore diameters of the nanoporous material used. For water confined in randomly oriented, interconnected nanopores, it is bound on the substrate on one side only and therefore less confined. The water will be more confined and have better dimension control if it is in between two rigid substrates which are highly charged. In addition, the majority of available results are limited to low frequency water measurement with frequency up to several MHz. It will be very interesting to investigate the water dielectric dynamics in the higher frequency range since orientational polarization has maximum influence on the permittivity of water at microwave frequencies. An on-chip, broadband microwave characterization device, to be developed in this paper, can help solve those problems and provides a new technique for confined water dynamics research.

The objective of this paper is to develop a broadband dielectric spectrometer with 1-10 nm planar nanofluidic channels for the study of confinement effects of fluids and molecules. The approach is to use wet etch of native silicon dioxide and wafer bonding to form planar nanofluidic channels and to use doped silicon as transmission lines to provide broadband measurement capabilities. Measured water properties will serve to demonstrate the functionality of the developed spectrometers.

4.2.2 Device Fabrication and Experimental Setup

A transmission-line-based configuration is adopted in the device design. Bulk micromachining and wafer bonding technique are applied to form sub-10 nm deep planar nanofluidic channels and an inverted microstrip line test structure. Heavily-doped Silicon is used to build the transmission line. There are three major steps in the device fabrication: Bottom wafer fabrication, top wafer fabrication and wafer bonding. The fabrication procedures are outlined as follows:

Bottom wafer is started with a 4 inch in diameter, Silicon-On-Insulator (SOI) wafer. It has a 25 μm think n-type Si device layer with resistivity of 0.001-0.002 Ω·cm, 2 μm thick SiO_2 box layer and 500 μm thick n-type Si handle layer with resistivity of 1-10 Ω·cm. An array of nanotrench are formed using a technique, called as multiple-HF-dip, developed in [128]. This technique repeatedly utilizes native oxide hydrofluoric (HF) etch and native oxide re-growth process to etch Si with a very slow etch rate in a controllable fashion. After 10 times HF etches, trench depth of ~10 nm is obtained. Figure 4.10 shows the 3-D images of obtained Si nanotrenches and the trench surface through Atomic Force Microscope (AFM) measurement. The obtained trench surfaces are very smooth with rms. roughness of 0.336 nm, which is comparable to the unprocessed Si wafer surface. The smooth trench surface is very favorable in the nanofluidics, especially for very shallow planar nanochannel formations. The trenches are 2 μm wide, 75 μm long and spaced by 5 μm. Next, the microstrip signal line with the length of 500 μm and width of 75 μm are patterned and etched through SOI Si device layer until SiO_2 box layer is reached. At each end of the microstrip line, a 400 μm long 50 Ω silicon coplanar waveguide (CPW) transition section for ground-signal-ground (GSG) probe contacts during on-chip measurements is fabricated in the same way as well. Figure 4.11(a) shows a microscopy image of fabricated bottom wafer. Center portion of the microstrip signal line bears 43 parallel nanotrenches.

Top wafer is started with a 4 inch in diameter, double-Side-Polished (DSP) p-type Si wafer with resistivity of 0.001-0.002 Ω·cm. Some open windows are needed for probe access of the GSG pads and inlet/outlet for fluidic sample injection. Deep reactive ion etch (DRIE) is used to etch through the 350 μm thick top Si wafer to form those windows.

The last procedure is to bond the bottom wafer and the top wafer together through Si-Si direct fusion bonding technique. Two wafers are thoroughly cleaned using standard RCA1 and RCA2 wafer cleaning procedures. Then they are carefully aligned and quickly transferred to wafer bonder for pre-bonding under temperature of 400 ℃ for 60 minutes. High temperature N_2 annealing under temperature of 1100 ℃ for 2 hours is followed to improve the bonding strength. After wafer bonding, parallel nanotrenches are sealed by the top wafer. Finally a microwave device with an inverted microstrip line which bears a parallel array of planar nanofluidic channels is therefore formed. Figure 4.11(b) shows a microscopy image of the bonded device. The CPW transition sections are visible through the open windows of the top wafer, but the nanochannels are invisible since they are covered by the top Si wafer.

Integrity of formed nanochannels is examined through Scanning Electron Microscope (SEM). Figure 4.12 shows a SEM image on the cross section of the fabricated Si planar nanochannels. The nanochannel is uniform across the whole channel width. No collapse is observed. Right-side edge of the nanochannel is zoomed in to show the details. The inset in Figure 4.12 clearly shows rounded channel edge which is due to anisotropic HF wet etch process during trench formation. In addition, seamless Si-Si bonding interface indicates good wafer bonding and strong bonding strength.

An Agilent N5230A PNA-L Network Analyzer is used to conduct on-chip two-port microwave measurements. Ground-signal-ground (GSG) probes are used to measure scattering parameters of the microwave device with or without sample fluids injected into the nanofluidic channels. Reliable electrical contacts between GSG probe tips and the silicon CPW electrodes are obtained and verified through DC resistance measurements. A full two-port short-open-load-through (SOLT) calibration procedure is performed before S-parameter measurements which are conducted from 2 GHz to 8 GHz at a power level of 10 dBm.

4.2.3 Results and Discussions

Deionized (DI) water is used as a sample fluid to experimentally demonstrate the functionality of the fabricated devices. Figure 4.13 shows measured S-parameters of the device when the nanochannels are injected with or without water. When there is no water injected into nanochannels, measured transmission coefficient S_{21} is around a level of - 40 dB, which indicates that a large loss exists. Small nanochannel depth and Si transmission line are two main factors which introduce such large loss. With 10 nm deep air nanochannels, the characteristic impedance Z_0 of microstrip line is very small, e.g., ~1-2 Ω, and it will get even smaller after the channels are filled with water. However, measurement system impedance is 50 Ω. This impedance mismatch will cause large reflection and therefore small S_{21}. In addition, heavily-doped silicon material, instead of commonly used metal materials, is used to build the transmission line in our device in order to have very smooth nanochannel walls/surfaces but with sacrifice on the S_{21} due to large conductor loss from used silicon material with conductivity of ~10^5 S m-1, which is at least 100 times smaller than conductivity of commonly used metal materials, such as Au, Al, Cu, etc.. The yield signal intensity of S_{21} is low as expected but still adequate for transmission line property characterization.

With the help of capillary force, DI water is injected into nanochannels [128]. After water injection, transmission coefficient S_{21} is dramatically decreased by up to 20 dB, which is expected due to high dielectric loss of water in the measured frequency region. Reflection coefficient S_{11} does not have visible change. Effect of water which resides along the water filling path is examined through a dummy test device which has exact the same structure except no nanochannels. Before and after water filling, the measured S-parameters do not have visible change, which indicates that the decease of S_{21} is mainly contributed from the water filled inside the nanochannels, not anywhere else. The water measurement validates functionality of fabricated devices.

In order to effectively conduct the confinement effect study, it is better to push the nanochannel depth to even smaller values, e.g., approaching to 1~2 nm. The proposed device fabrication flow can be directly applied or modified to achieve this goal but with some further design considerations: (i) Channel collapse/survival during the wafer bonding. Kim et al presented criteria for channel collapse when trying to bond two wafers together [129, 130]. Channel aspect ratio, surface energy and Young's modulus of wafers are main factors which will determine whether the channel is collapsed or not. When two wafers are in intimate contact from each other, strong Van der Waal force will intend to bring two surfaces together therefore block the channels. When desired channel depth approaches several nanometers, channel collapse is very intended to happen for such low aspect ratio (depth to width). Thus special consideration is needed for channel dimensions and surface treatments. In addition to the theoretical guidance, the nanochannel fabrication and its characterization will give you further verification on channel collapse/survival. (ii) Signal intensity of measured S-parameters. The smaller depth of channel, the smaller characteristic impedance of microstrip line, therefore the smaller S_{21} and the bigger S_{11} due to the bigger impedance mismatch. The signal level of S_{21} should be taken into design considerations and it has to be adequate for proper transmission line characterization even with the high sensitive measurement system, e.g., network analyzer with large dynamic range. (iii) Stringent control on roughness of the nanochannel surfaces/walls. It has more restricted requirements on surface roughness when the channel depth is scaled down to several nanometers. Although applied multiple-HF-dip technique have provided very smooth trench surface, e.g., with rms. roughness of 0.336 nm, the fabrication process needs to be further improved to meet the needs of 1~2 nm deep nanochannel fabrications.

4.2.4 Conclusions

An on-chip, broadband microwave dielectric spectrometer with integrated transmission line and nanofluidic channels is designed, fabricated and characterized through microwave S-parameter measurements. Heavily-doped Si material is used to build the microstrip line to provide broadband characterization capability. 10 nm deep planar Si nanofluidic channels are fabricated through native oxide etch and wafer bonding process. It is the first effort to build the microstrip line with periodically loaded individual sub-10 nm nanofluidic channels to conduct the broadband high frequency characterization of materials within confined space. The functionality of the device is demonstrated by the measurement of DI water. It behaves well and has great potentials on the study of confinement effects of fluids and molecules. Further work includes development of parasitic signal de-embedding procedures for accurate measurements.

ACKNOWLEDGMENT

The work is supported by NSF under Award #0925424. The fabrication is conducted at the Cornell NanoScale Science and Technology Facility (CNF) in Cornell University.

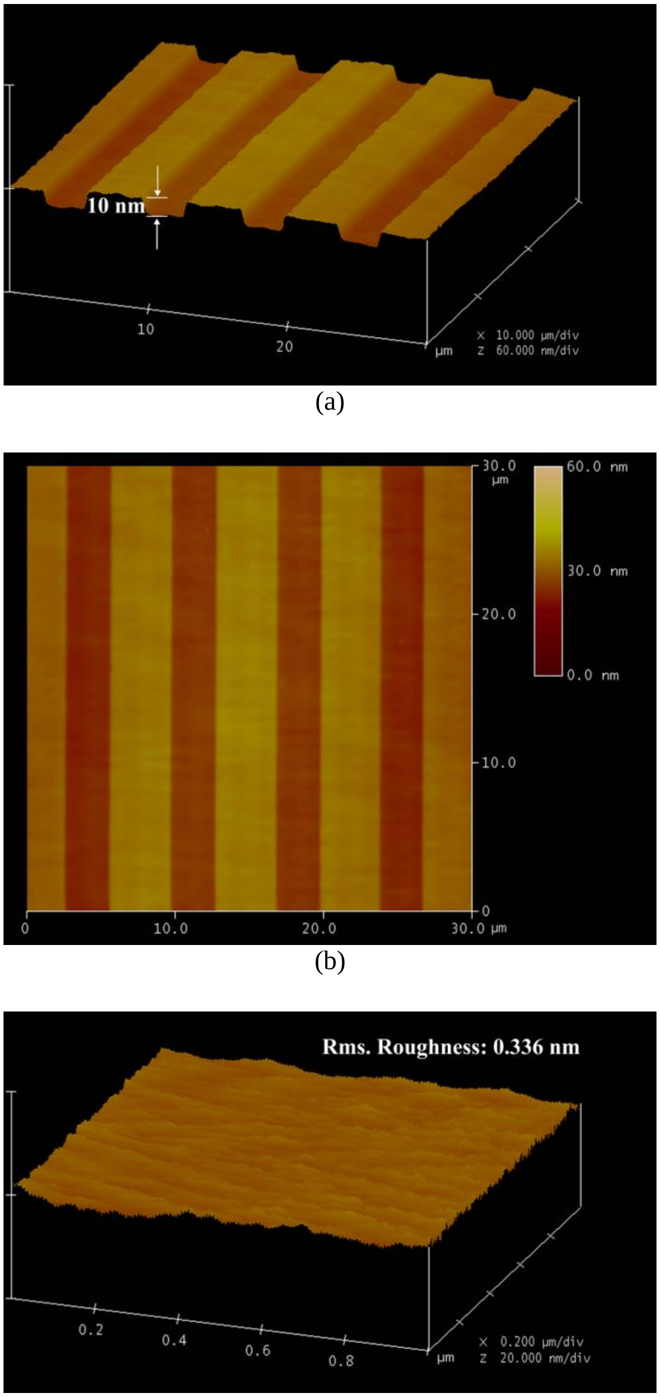

(a)

(b)

(c)

Figure 4.10: AFM images of fabricated 10 nm deep Si nanotrenches. (a) 3-D view. (b) Top view. (c) Rms. roughness of trench surface.

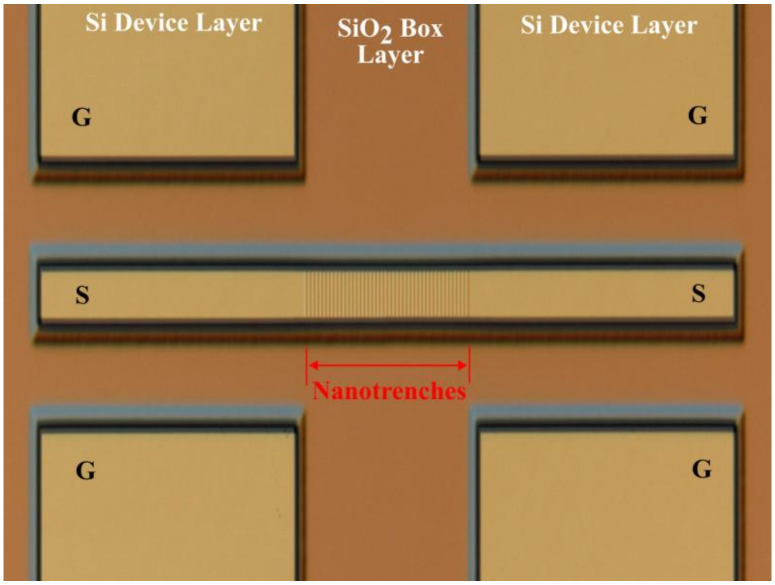

(a)

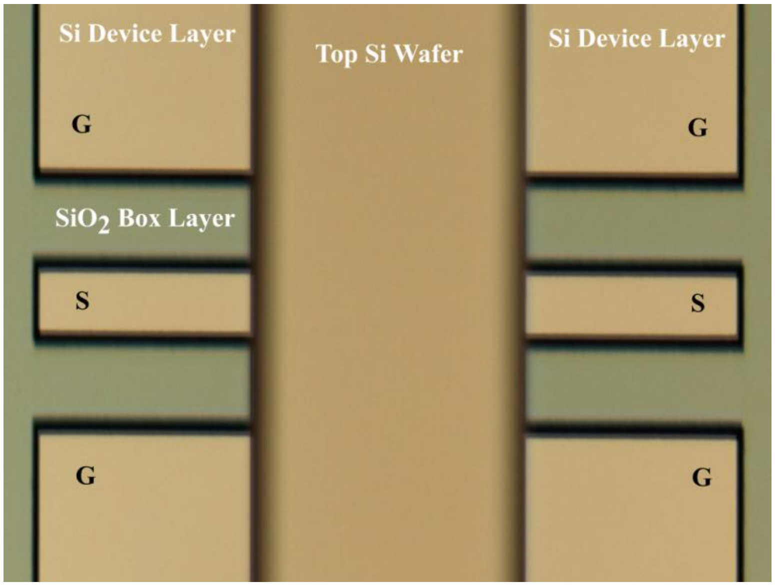

(b)

Figure 4.11: Microscopy images of (a) fabricated patterns (two CPW transition sections and a microstrip line which bears nanofluidic channels) in the bottom wafer and (b) final device after bonding the top wafer to the bottom wafer.

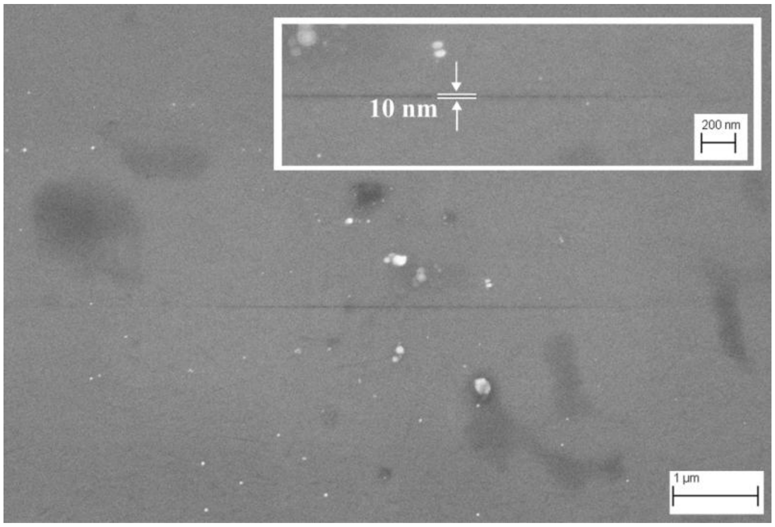

Figure 4.12: A SEM cross-section view of a fabricated 10 nm deep planar Si nanochannel. Included inset is a close-up image at the right-side edge of the nanochannel.

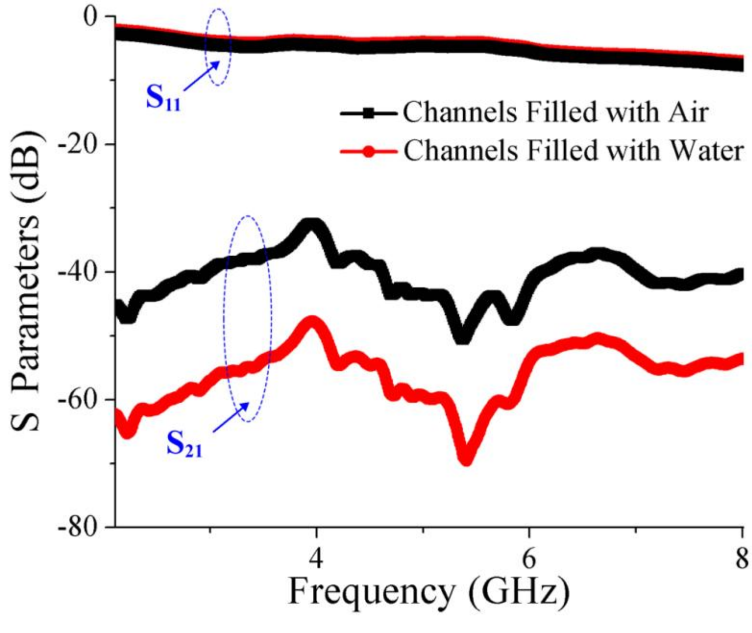

Figure 4.13: Measured S-Parameters (a) before water injection and (b) after water injection.

REFERENCES

[1] P. J. Burke, "Luttinger liquid theory as a model of the gigahertz electrical properties of carbon nanotubes," *IEEE Transactions on Nanotechnology,* vol. 1, pp. 129-144, September 2002 2002.

[2] P. L. McEuen, M. S. Fuhrer, and H. K. Park, "Single-walled carbon nanotube electronics," *IEEE Transactions on Nanotechnology,* vol. 1, pp. 78-85, Mar 2002.

[3] A. Naeemi and J. D. Meindl, "Monolayer metallic nanotube interconnects: Promising candidates for short local interconnects," *IEEE Electron Device Lett.,* vol. 26, pp. 544-546, Aug 2005.

[4] F. Rodriguez-Morales, R. Zannoni, J. Nicholson, M. Fischetti, K. S. Yngvesson, and J. Appenzeller, "Direct and heterodyne detection of microwaves in a metallic single wall carbon nanotube," *Applied Physics Letters,* vol. **89**, pp. 083502-1-3, 2006.

[5] J. J. Plombon, K. P. O'Brien, F. Gstrein, and V. M. Dubin, "High-frequency electrical properties of individual and bundled carbon nanotubes," *Applied Physics Letters,* vol. 90, pp. 063106-1-3, 2007.

[6] M. Zhang, X. Huo, P. C. H. Chan, Q. Liang, and Z. K. Tang, "Radio-frequency characterization for the single-walled carbon nanotubes," *applied Physics Letters,* vol. 88, pp. 163109-1-3, 2006.

[7] P. J. Burke, "An rf circuit model for carbon nanotubes," *IEEE Trans. Nanotechnology*, vol. 2, pp. 55-58, 2003.

[8] M. A. Stuchly and S. S. Stuchly, "Coaxial line reflection methods for measuring dielectric properties of biological substances at radio and microwave frequencies-a review," *IEEE Transactions on Instrumentation and Measurement,* vol. 29, pp. 176-183, 1980.

[9] A. Ocera, M. Dionigi, E. Fratticcioli, and R. Sorrentino, "A novel technique for complex permittivity measurement based on a planar four-port device," *IEEE Transactions on Microwave Theory and Techniques,* vol. 54, pp. 2568-2575, 2006.

[10] M. A. E. Sabbagh, "Use of microstrip patch antennas in grain permittivity measurement," *Proc. Intrum. Meas. Tech. Conf,* pp. 640-644, 2003.

[11] M. D. Janezic, D. F. Williams, V. Blaschke, A. Karamcheti, and C. S. Chang, "Permittivity characterization of low-k thin films from transmission-line measurements," *IEEE Transactions on Microwave Theory and Techniques,* vol. 51, pp. 132-136, 2003.

[12] K. Folgero, "Broad-band dielectric spectroscopy of low-permittivity fluids using one measurement cell," *IEEE Transactions on Instrumentation and Measurement,* vol. 47, pp. 881-885, 1998.

[13] A. Raj, W. S. Holmes, and S. R. Judah, "Wide bandwidth measurement of complex permittivity of liquids using coplanar lines," *IEEE Transactions on Instrumentation and Measurement,* vol. 50, pp. 905-909, 2001.

[14] J. Mateu, N. Orloff, M. Rinehart, and J. C. Booth, "Broadband permittivity of liquids extracted from transmission line measurements of microfluidic channels," *IEEE MTT,* pp. 523-526, 2007.

[15] J. Hefti, A. Pan, and A. Kumar, "Sensitive detection method of dielectric dispersion in aqueous-based, surface-bound macromolecular structures using microwave spectroscopy," *Applied Physics Letters,* vol. 75, pp. 1802-1804, 20 September 1999 1999.

[16] G. R. Facer, D. A. Notterman, and L. L. Sohn, "Dielectric spectroscopy for bioanalysis: From 40 hz to 26.5 ghz in a microfabricated wave guide," *Appl. Phys. Lett.,* vol. 78, pp. 996-998, Feb 2001.

[17] J. Knight, "Microfluidics: Honey, i shrunk the lab," *Nature,* vol. 418, pp. 474-475, 1 August 2002 2002.

[18] D. F. Williams and R. B. Marks, "Accurate transmission line characterization," *IEEE Microwave and Guided Wave Letters,* vol. 3, pp. 247-249, 1993.

[19] D. F. Williams, J. C. M. Wang, and U. Arz, "An optimal vector-network-analyzer calibration algorithm," *IEEE Transactions on Microwave Theory and Techniques,* vol. 51, pp. 2391-2401, 2003.

[20] H. Chien-Hsun, F. Lu, and C. Kai, "Broad-band uniplanar hybrid-ring and branch-line couplers," *IEEE Trans. Micro. Theo. Tech,* vol. 41, pp. 2116-2125, 1993.

[21] C.-C. Chen and C.-K. C. Tzuang, "Synthetic quasi-tem meandered transmission lines for compacted microwave integrated circuits," *IEEE Transactions on Microwave Theory and Techniques,* vol. 52, pp. 1637-1647, 2004.

[22] K. M. Taylor and D. W. van der Weide, "Ultra-sensitive detection of protein thermal unfolding and refolding using near-zone microwaves," *IEEE Transactions on Microwave Theory and Techniques,* vol. 53, pp. 1576-1586, May 2005.

[23] M. Olapinski, S. Manus, M. George, A. Bruggemann, N. Fertig, and F. C. Simmel, "Detection of lipid bilayer and peptide pore formation at gigahertz frequencies," *Appl. Phys. Lett.,* vol. 88, pp. 013902-1-3, Jan 2006.

[24] J. Hefti, A. Pan, and A. Kumar, "Sensitive detection method of dielectric dispersions in aqueous-based, surface-bound macromolecular structures using microwave spectroscopy," *Appl. Phys. Lett.,* vol. 75, pp. 1802-1804, Sep 1999.

[25] H. Morgan, T. Sun, D. Holmes, S. Gawad, and N. G. Green, "Single cell dielectric spectroscopy," *Journal of Physics D: Applied Physics,* vol. 40, pp. 61-70, 2007.

[26] Q. Chen, D. Roitman, and A. Knoesen, "Transit time coplanar probe for biomolecular interactions at an aqueous-solid interface," *Sensors and Actuators A: Physical*, vol. 133, pp. 480-485, 2007.

[27] S. Okamura, Y. J. Zhang, and N. Tsukamoto, "A new microstripline-type moisture sensor for heavily wet tea leaves," *Measurement Science & Technology,* vol. 18, pp. 1022-1028, 2007.

[28] M. Werner, "Novel microwave sensors for detection of subsurface moisture and acid," *Subsurface Sensing Technologies and Applications,* vol. 1, pp. 441-451, Oct. 2000.

[29] J. Mateu, N. Orloff, M. Rinehart, and J. C. Booth, "Broadband permittivity of liquids extracted from transmission line measurements of microfluidic channels," in *IEEE/MTT-S International Microwave Symposium 2007,* 2007, pp. 523-526.

[30] J. J. Shah, S. G. Sundaresan, J. Geist, D. R. Reyes, J. C. Booth, M. V. Rao, et al., "Microwave dielectric heating of fluids in an integrated microfluidic device," *J. Micromech. Microeng.,* vol. 17, pp. 2224-2230, Nov 2007.

[31] T. Akalin, S. Arscott, B. Bocquet, N. E. Bourzgui, V. Mille, V. Senez, et al., "Microfluidic devices for ultra wide band electromagnetic spectroscopy of single cell," in *2006 International Conference on Microtechnologies in Medicine and Biology,* 2006, pp. 252-255.

[32] D. Debuisson, A. Treizebre, T. Houssin, E. Leclerc, D. Bartes-Biesel, D. Legrand, et al., "Nanoscale devices for online dielectric spectroscopy of biological cells," *Physiological Measurement,* vol. 29, pp. S213-S225, 2008.

[33] C. Song and P. Wang, "On-chip cancellation of parasitic effects for dielectric permittivity measurement," in *2008 IEEE MTT-S International Microwave Symposium Digest,*, 2008, pp. 131-134.

[34] S. Mashimo, T. Umehara, and H. Redlin, "Structures of water and primary alcohol studied by microwave dielectric analyses," *J. Chem. Phys.*, vol. 95, pp. 6257-6260, Nov 1991.

[35] C. Ionescu-Zanetti, J. T. Nevill, D. Di Carlo, K. H. Jeong, and L. P. Lee, "Nanogap capacitors: Sensitivity to sample permittivity changes," *J. Appl. Phys.*, vol. 99, pp. 024305-1-5, Jan 2006.

[36] Q. Chen, D. Roitman, and A. Knoesen, "Transit time coplanar probe for biomolecular interactions at an aqueous-solid interface," *Sens. Actuator A-Phys.*, vol. 133, pp. 480-485, 2007.

[37] S. Okamura, Y. J. Zhang, and N. Tsukamoto, "A new microstripline-type moisture sensor for heavily wet tea leaves," *Measurement Science & Technology* vol. 18, pp. 1022-1028, 2007.

[38] T. Akalin, S. Arscott, B. Bocquet, N. E. Bourzgui, V. Mille, V. Senez, et al., "Microfluidic devices for ultra wide band electromagnetic spectroscopy of single cell," in *2006 International Conference on Microtechnologies in Medicine and Biology* Bankoku-Shinryokan, Okinawa, Japan, 2006, pp. 252-255.

[39] C. Song and P. Wang, "A radio frequency device for measurement of minute dielectric property changes in microfluidic channels," *Appl. Phys. Lett.*, vol. 94, pp. 023901-1-3, Jan 2009.

[40] D. M. Pozar, "Microwave engineering," 3 rd ed New Jersey: John Wiley & Sons, 2005.

[41] M. F. Iskander and T. S. Lind, "Electromagnetic coupling of coplanar waveguides and microstrip lines to highly lossy dielectric media," *IEEE Trans. Microw. Theory Tech.,* vol. 37, pp. 1910-1917, 1989.

[42] E. L. Chen and S. Y. Chou, "Characteristics of coplanar transmission lines on multilayer substrates: Modeling and experiments," *IEEE Trans. Microw. Theory Tech.,* vol. 45, pp. 939-945, Jun 1997.

[43] J. Svačina, "A simple quasi-static determination of basic parameters of multilayer microstrip and coplanar waveguide," *IEEE Microwave and Guided Wave Letters,* vol. 2, pp. 385-387, 1992.

[44] S. Mashimo, N. Miura, T. Umehara, S. Yagihara, and K. Higasi, "The structure of water and methanol in p-dioxane as determined by microwave dielectric-spectroscopy," *J. Chem. Phys.,* vol. 96, pp. 6358-6361, May 1992.

[45] Q. Chen, J. McMurdie, D. Roitman, and A. Knoesen, "Microwave transmission line dielectric probe to detect biomolecular surface interactions," in *26th Annual International Conference of the IEEE EMBS* San Franciso, CA, 2004.

[46] P. Wang, "Network analyzer on chip: The ultimate radio-frequency system-on-chip," The State University of New York Buffalo, 2005.

[47] N. Manaresi, G. Medoro, M. Tartagni, L. Altomare, and R. Guerrieri, "Microelectronics meets biology: Challenges and opportunities for functional integration in lab-on-a-chip," in *ESSCIRC*, 2002.

[48] Y. Eo and W. R. Eisenstadt, "High-speed vlsi interconnect modeling based on s-parameter measurements," *IEEE Trans. Components Hybrids and Manufacturing Technology,* vol. 16, pp. 555-562, Aug 1993.

[49] Y. J. Yoon and B. Kim, "A new formula for effective dielectric constant in multi-dielectric layer microstrip structure," in *Proceedings of the IEEE Electrical Performance of Electronic Packaging*, 2001, pp. 163-167.

[50] J. Svačina, "Analysis of multilayer microstrip lines by a conformal mapping method," *IEEE Transactions on Microwave Theory and Techniques,* vol. 40, pp. 769-772, Apr 1992.

[51] R. B. Marks, "A multiline method of network analyzer calibration," *IEEE Transactions on Microwave Theory and Techniques,* vol. 39, pp. 1205-1215, Jul 1991.

[52] A. I. Gerasimov, "Water as an insulator in pulsed facilities - (review)," *Instrum. Exp. Tech.,* vol. 48, pp. 141-167, Mar-Apr 2005.

[53] K. Schoenbach, J. Kolb, S. Xiao, S. Katsuki, Y. Minamitani, and R. Joshi, "Electrical breakdown of water in microgaps," *Plasma Sources Science & Technology* vol. 17, pp. 24010-1-10, May 2008.

[54] C. H. Tsau, S. M. Spearing, and M. A. Schmidt, "Characterization of wafer-level thermocompression bonds," *J. Microelectromech. Syst.,* vol. 13, pp. 963-971, Dec 2004.

[55] T. Liu, E. V. Moiseeva, and C. K. Harnett, "Chips & tips: Integrated reservoirs for pdms microfluidic chips," Available at: http://www.rsc.org/Publishing/Journals/lc/Chips_and_Tips/integrated_reservoirs.asp.

[56] R. Foest, M. Schmidt, and K. Becker, "Microplasmas, an emerging field of low-temperature plasma science and technology," *International Journal of Mass Spectrometry,* vol. 248, pp. 87-102, 2006.

[57] V. F. Klimkin, "Super high-speed anode pre-breakdown phenomena in liquid dielectrics under uniform fields," in *ICDL '93., IEEE 11th International Conference on Conduction and Breakdown in Dielectric Liquids 1993* Baden-Dattwil, Switzerland, 1993, pp. 299-303.

[58] X. Lu, J. F. Kolb, S. Xiao, M. Laroussi, K. H. Schoenbach, and E. Schamiloglu, "Dielectric strength of sub-millimeter water gaps subjected to microsecond and sub-microsecond voltage pulses," in *2005 IEEE Pulsed Power Conference* Monterey, CA, 2005, pp. 600-603.

[59] D. A. Wetz, J. J. Mankowski, J. C. Dickens, and M. Kristiansen, "The impact of field enhancements and charge injection on the pulsed breakdown strength of water," *IEEE Transactions on Plasma Science,* vol. 34, pp. 1670-1679, 2006.

[60] C. H. Tsau, S. M. Spearing, and M. A. Schmidt, "Fabrication of wafer-level thermocompression bonds," *J. Microelectromech. Syst.,* vol. 11, pp. 641-647, Dec 2002.

[61] R. P. Joshi, J. Qian, K. H. Schoenbach, and E. Schamiloglu, "Microscopic analysis for water stressed by high electric fields in the prebreakdown regime," *J. Appl. Phys.,* vol. 96, pp. 3617-3625, Oct 2004.

[62] R. P. Joshi, J. Qian, J. Kolb, and K. H. Schoenbach, "Model analysis of breakdown in high-voltage, water-based switches," in *14th IEEE International Pulsed Power Conference, 2003. Digest of Technical Papers. PPC-2003* Dallas, TX, 2003, pp. 293-296.

[63] R. P. Joshi, J. Qian, G. Zhao, J. Kolb, K. H. Schoenbach, E. Schamiloglu, et al., "Are microbubbles necessary for the breakdown of liquid water subjected to a submicrosecond pulse?," *J. Appl. Phys.,* vol. 96, pp. 5129-5139, 2004.

[64] J. F. Kolb, R. P. Joshi, S. Xiao, and K. H. Schoenbach, "Streamers in water and other dielectric liquids," *Journal of Physics D: Applied Physics,* vol. 41, pp. 234007-1-22, Dec 2008.

[65] N. F. Bunkin and A. V. Lobeev, "Bubbston-cluster structure under conditions of optical breakdown in a liquid," *Quantum Electron,* vol. 24, pp. 297-301, Apr 1994.

[66] J. M. Lehr, "Effect of de-aeration on the electrical breakdown characteristics of water," in *Conference on Electrical Insulation and Dielectric Phenomena 1998,* Atlanta, GA, 1998, pp. 460-463.

[67] M. Aguilella-Arzo, A. Andrio, V. M. Aguilella, and A. Alcaraz, "Dielectric saturation of water in a membrane protein channel," *Phys. Chem. Chem. Phys.,* vol. 11, pp. 358-365, 2009.

[68] S. Gavryushov, "Dielectric saturation of the ion hydration shell and interaction between two double helices of DNA in mono- and multivalent electrolyte solutions: Foundations of the epsilon-modified poisson-boltzmann theory," *J. Phys. Chem. B,* vol. 111, pp. 5264-5276, May 2007.

[69] K. Lebedev, S. Mafe, A. Alcaraz, and P. Ramirez, "Effects of water dielectric saturation on the space-charge junction of a fixed-charge bipolar membrane," *Chem. Phys. Lett.,* vol. 326, pp. 87-92, Aug 2000.

[70] D. A. Cherepanov, B. A. Feniouk, W. Junge, and A. Y. Mulkidjanian, "Low dielectric permittivity of water at the membrane interface: Effect on the energy coupling mechanism in biological membranes," *Biophys. J.,* vol. 85, pp. 1307-1316, Aug 2003.

[71] U. Pliquett, R. P. Joshi, V. Sridhara, and K. H. Schoenbach, "High electrical field effects on cell membranes," *Bioelectrochemistry*, vol. 70, pp. 275-282, May 2007.

[72] F. Booth, "The dielectric constant of water and the saturation effect," *J. Chem. Phys.,* vol. 19, pp. 391-394, 1951.

[73] Y. Minamitani, Y. Ohe, and Y. Higashiyama, "Nanosecond high voltage pulse generator using water gap switch for compact high power pulsed microwave generator," *IEEE Trans. Dielectr. Electr. Insul.,* vol. 14, pp. 894-899, Aug 2007.

[74] J. C. Martin, "Nanosecond pulse techniques," *Proceedings of the IEEE*, vol. 80, pp. 934-945, 1992.

[75] H. A. Kotodziej, G. P. Jones, and M. Davies, "High field dielectric measurements in water," *J. Chem. Soc., Faraday Trans. 2,* vol. 71, pp. 269-274, 1975.

[76] J. Kolb, Y. Minamitani, S. Xiao, X. Lu, M. Laroussi, R. P. Joshi, et al., "The permittivity of water under high dielectric stress," in *Pulsed Power Conference, 2005 IEEE*, 2005, pp. 1266-1269.

[77] I. C. Yeh and M. L. Berkowitz, "Dielectric constant of water at high electric fields: Molecular dynamics study," *J. Chem. Phys.*, vol. 110, pp. 7935-7942, Apr 1999.

[78] K. Schoenbach, J. Kolb, S. Xiao, S. Katsuki, Y. Minamitani, and R. Joshi, "Electrical breakdown of water in microgaps," *Plasma Sources Sci. Technol.*, vol. 17, pp. 024010-1-10, 2008.

[79] W. A. Stygar, T. C. Wagoner, H. C. Ives, Z. R. Wallace, V. Anaya, J. P. Corley, et al., "Water-dielectric-breakdown relation for the design of large-area multimegavolt pulsed-power systems," *Phys. Rev. Spec. Top.-Accel. Beams*, vol. 9, pp. 070401-1-9, Jul 2006.

[80] Agilent, "Agilent 8510c network analyzer data sheet," Available at: http://cp.literature.agilent.com/litweb/pdf/5091-8484E.pdf.

[81] A. A. Kornyshev and G. Sutmann, "Nonlocal dielectric saturation in liquid water," *Phys. Rev. Lett.*, vol. 79, pp. 3435-3438, Nov 1997.

[82] J. Haneveld, H. Jansen, E. Berenschot, N. Tas, and M. Elwenspoek, "Wet anisotropic etching for fluidic 1d nanochannels," *J. Micromech. Microeng.*, vol. 13, pp. S62-S66, 2003.

[83] M. D. Janezic, D. F. Williams, V. Blaschke, A. Karamcheti, and C. S. Chang, "Permittivity characterization of low-k thin films from transmission-line measurements," *IEEE Transactions on Microwave Theory and Techniques*, vol. 51, pp. 132-136, Jan 2003.

[84] Agilent Application Notes, "Ultra-low impedance measurements using 2-port measurements," Available at: http://cp.literature.agilent.com/litweb/pdf/5989-5935EN.pdf.

[85] I. T. Johansen, "Electrical conductivity in evaporated silicon oxide films," *J. Appl. Phys.*, vol. 37, pp. 499-&, 1966.

[86] S. H. Lo, D. A. Buchanan, Y. Taur, and W. Wang, "Quantum-mechanical modeling of electron tunneling current from the inversion layer of ultra-thin-oxide nmosfet's," *IEEE Electron Device Letters*, , vol. 18, pp. 209-211, May 1997.

[87] J. C. Fisher and I. Giaever, "Tunneling through thin insulating layers," *J. Appl. Phys.*, vol. 32, pp. 172-&, 1961.

[88] M. C. M. Lee and M. C. Wu, "Thermal annealing in hydrogen for 3-d profile transformation on silicon-on-insulator and sidewall roughness reduction," *J. Microelectromech. Syst.,* vol. 15, pp. 338-343, Apr 2006.

[89] Y. Eo and W. R. Eisenstadt, "High-speed vlsi interconnect modeling based on s-parameter measurements," *IEEE Trans. Compon. Hybrid. Manuf. Technol.,* vol. 16, pp. 555-562, August 1993.

[90] W. J. Ellison, "Permittivity of pure water, at standard atmospheric pressure, over the frequency range 0--25 thz and the temperature range 0-100 ℃," *J. Phys. Chem. Ref. Data,* vol. 36, pp. 1-18, 2007.

[91] T. S. Light, S. Licht, A. C. Bevilacqua, and K. R. Morash, "The fundamental conductivity and resistivity of water," *Electrochem. Solid-State Lett.,* vol. 8, pp. E16-E19, 2005.

[92] S. Pamidighantam, R. Puers, K. Baert, and H. A. C. Tilmans, "Pull-in voltage analysis of electrostatically actuated beam structures with fixed-fixed and fixed-free end conditions," *J. Micromech. Microeng.,* vol. 12, pp. 458-464, 2002.

[93] R. Richert and S. Weinstein, "Nonlinear dielectric response and thermodynamic heterogeneity in liquids," *Phys. Rev. Lett.,* vol. 97, pp. 095703-1-4, Sep 2006.

[94] J. Banys, M. Kinka, A. Meskauskas, J. Macutkevic, G. Volkel, W. Bohlman, et al., "Broadband dielectric spectroscopy of water confined in mcm-41 molecular sieve material," *Ferroelectrics,* vol. 318, pp. 201-207, 2005.

[95] M. C. Gordillo, G. Nagy, and J. Marti, "Structure of water nanoconfined between hydrophobic surfaces," *J. Chem. Phys.,* vol. 123, p. 054707, 2005.

[96] Q. F. Xia, K. J. Morton, R. H. Austin, and S. Y. Chou, "Sub-10 nm self-enclosed self-limited nanofluidic channel arrays," *Nano Lett.,* vol. 8, pp. 3830-3833, Nov 2008.

[97] J. S. Zhang and B. I. Shklovskii, "Effective charge and free energy of DNA inside an ion channel," *Phys. Rev. E,* vol. 75, p. 21906, Feb 2007.

[98] R. B. Schoch, J. Y. Han, and P. Renaud, "Transport phenomena in nanofluidics," *Rev. Mod. Phys.,* vol. 80, pp. 839-883, Jul-Sep 2008.

[99] M. A. M. Gijs, "Device physics - will fluidic electronics take off?," *Nat. Nanotechnol.,* vol. 2, pp. 268-270, May 2007.

[100] E. A. Strychalski, S. M. Stavis, and H. G. Craighead, "Non-planar nanofluidic devices for single molecule analysis fabricated using nanoglassblowing," *Nanotechnology,* vol. 19, p. 31530, Aug 2008.

[101] H. Cao, Z. N. Yu, J. Wang, J. O. Tegenfeldt, R. H. Austin, E. Chen, et al., "Fabrication of 10 nm enclosed nanofluidic channels," *Appl. Phys. Lett.,* vol. 81, pp. 174-176, Jul 2002.

[102] J. Gu, R. Gupta, C. Chou, Q. Wei, and F. Zenhausern, "A simple polysilsesquioxane sealing of nanofluidic channels below 10 nm at room temperature," *Lab on a Chip,* vol. 7, pp. 1198-1201, 2007.

[103] J. Haneveld, N. R. Tas, N. Brunets, H. V. Jansen, and M. Elwenspoek, "Capillary filling of sub-10 nm nanochannels," *J. Appl. Phys.,* vol. 104, p. 014309, 2008.

[104] K. M. van Delft, J. C. T. Eijkel, D. Mijatovic, T. S. Druzhinina, H. Rathgen, N. R. Tas, et al., "Micromachined fabry-perot interferometer with embedded nanochannels for nanoscale fluid dynamics," *Nano Lett.,* vol. 7, pp. 345-350, Feb 2007.

[105] P. Mao and J. Y. Han, "Fabrication and characterization of 20 nm planar nanofluidic channels by glass-glass and glass-silicon bonding," *Lab on a Chip,* vol. 5, pp. 837-844, 2005.

[106] M. Morita, T. Ohmi, E. Hasegawa, M. Kawakami, and M. Ohwada, "Growth of native oxide on a silicon surface," *J. Appl. Phys.,* vol. 68, pp. 1272-1281, Aug 1990.

[107] G. Willeke and K. Kellermann, "Crystalline silicon etching in quiescent concentrated aqueous hf solutions," *Semicond. Sci. Technol.,* vol. 11, pp. 415-421, Mar 1996.

[108] V. Dragoi, S. Farrens, P. Lindner, and J. Weixlberger, "Low temperature wafer bonding for microsystems applications," in *2004 International Semiconductor Conference, CAS 2004 Proceedings.,* 2004, pp. 199-202.

[109] S. Pamidighantam, R. Puers, K. Baert, and H. A. C. Tilmans, "Pull-in voltage analysis of electrostatically actuated beam structures with fixed-fixed and fixed-free end conditions," *Journal of Micromechanics and Microengineering,* vol. 12, pp. 458-464, Jul 2002.

[110] U. Gosele, Q. Y. Tong, A. Schumacher, G. Krauter, M. Reiche, A. Plossl, et al., "Wafer bonding for microsystems technologies," *Sensors and Actuators A,* vol. 74, pp. 161-168, 1999.

[111] L. H. Thamdrup, F. Persson, H. Bruus, A. Kristensen, and H. Flyvbjerg, "Experimental investigation of bubble formation during capillary filling of sio$_2$ nanoslits," *Appl. Phys. Lett.,* vol. 91, p. 163505, 2007.

[112] J. J. Gilijamse, A. J. Lock, and H. J. Bakker, "Dynamics of confined water molecules," *PNAS,* vol. 102, pp. 3202-3207, 2005.

[113] M.-C. Bellissent-Funel, "Status of experiments probing the dynamics of water in confinment," *Eur. Phys. J. E.,* vol. 12, pp. 83-92, 2003.

[114] Y. Lin, J. Shiomi, S. Maruyama, and G. Amberg, "Dielectric relaxation of water inside a single-walled carbon nanotube," *Phys. Rev. B*, vol. 80, p. 7, Jul 2009.

[115] J. Marti, G. Nagy, E. Guardia, and M. C. Gordillo, "Molecular dynamics simulation of liquid water confined inside graphite channels: Dielectric and dynamical properties," *J. Phys. Chem. B,* vol. 110, pp. 23987-23994, Nov 2006.

[116] S. H. Han, P. Kumar, and H. E. Stanley, "Hydrogen-bond dynamics of water in a quasi-two-dimensional hydrophobic nanopore slit," *Phys. Rev. E,* vol. 79, pp. 041202-1-5, Apr 2009.

[117] S. Senapati and A. Chandra, "Dielectric constant of water confined in a nanocavity," *J. Phys. Chem. B,* vol. 105, pp. 5106-5109, Jun 2001.

[118] P. Scheidler, W. Kob, and K. Binder, "The relaxation dynamics of a supercooled liquid confined by rough walls," *J. Phys. Chem. B*, vol. 108, pp. 6673-6686, May 2004.

[119] G. P. Sinha and F. M. Aliev, "Dielectric spectroscopy of liquid crystals in smectic, nematic, and isotropic phases confined in random porous media," *Phys. Rev. E*, vol. 58, pp. 2001-2010, Aug 1998.

[120] J. Banys, M. Kinka, G. Volkel, W. Bohlman, V. Umamaheswari, M. Hartmann, et al., "Dielectric spectroscopy of betaine phosphite confined in mcm-41 molecular sieve materials," *Ferroelectrics,* vol. 353, pp. 531-537, 2007.

[121] H. Jansson and J. Swenson, "Dynamics of water in molecular sieves by dielectric spectroscopy," *Eur. Phys. J. E.,* vol. 12, pp. S51-54, 2003.

[122] J. Banys, M. Kinka, J. Macutkevic, G. Volkel, W. Bohlmann, V. Umamaheswari, et al., "Broadband dielectric spectroscopy of water confined in mcm-41 molecular sieve materials - low-temperature freezing phenomena," *J. Phys.-Condes. Matter,* vol. 17, pp. 2843-2857, May 2005.

[123] M. Kinka, J. Banys, J. Macutkevic, A. Poppl, W. Bohlmann, V. Umamaheswari, et al., "Dielectric response of water confined in mcm-41 molecular sieve material," *Phys. Status Solidi B-Basic Solid State Phys.*, vol. 242, pp. R100-R102, Oct 2005.

[124] A. Spanoudaki, B. Albela, L. Bonneviot, and M. Peyrard, "The dynamics of water in nanoporous silica studied by dielectric spectroscopy," *Eur. Phys. J. E,* vol. 17, pp. 21-27, May 2005.

[125] G. Schiro, C. Antonio, S. E. Pagnotta, and F. Bruni, "Dynamic properties of solvent confined in silica gels studied by broadband dielectric spectroscopy," *J. Non-Cryst. Solids,* vol. 353, pp. 4546-4551, Dec 2007.

[126] M. Kondo, I. A. Heisler, and S. R. Meech, "Ultrafast reaction dynamics in nanoscale water droplets confined by ionic surfactants," *Faraday Discuss.,* vol. 145, pp. 185-203, 2010.

[127] J. J. Gilijamse, A. J. Lock, and H. J. Bakker, "Dynamics of confined water molecules," *Proceedings of the National Academy of Sciences of the United States of America,* vol. 102, pp. 3202-3207, March 1, 2005.

[128] C. Song and P. Wang, "Fabrication of sub-10 nm planar nanofluidic channels through native oxide etch and anodic wafer bonding," *IEEE Transactions on Nanotechnology,* vol. 9, pp. 138-141, Mar 2010.

[129] W. S. Kim, J. Lee, and R. Ruoff, "Nanofludic channel fabrication and characterization by micromachining," in *Proceedings of IMECE'03,* Washington D.C., 2003, pp. 1-6.

[130] J. L. Perry and S. G. Kandlikar, "Review of fabrication of nanochannels for single phase liquid flow," *Microfluidics and Nanofluidics,* vol. 2, pp. 185-193, May 2006.